

Electrochemical performance improvement using  
graphene nanosheets and hybrid carbon nanofiber-  
carbon black as cathode in hybrid Li-air battery

M a r c h 2 0 1 7

Chang-Ho, Ahn.

Electrochemical performance improvement using  
graphene nanosheets and hybrid carbon nanofiber-  
carbon black as cathode in hybrid Li-air battery

Graduate School of Systems and Information  
Engineering  
University of Tsukuba

M a r c h 2 0 1 7

Chang-Ho, Ahn.

## Abstract

The Li-air battery was considered one of power sources instead of Li-ion battery for EV. Because of its extremely high theoretical energy density. However, it still showed drawbacks such as low cycle performance and high overpotential gap during cycle performance. Therefore, precious metal catalysts have been used to solve those problems. However its high cost also was considered serious problem. Therefore, many kind of catalysts were investigated such as carbon material and transition material to use for alternative material to solve cost problem. Nevertheless, its low electro catalytic activity and low duration were considered that new catalyst should be researched to enhance electrochemical performance for Li-air battery.

The electrochemical performance of RGO-Co(mqph) electro catalyst for Li-air batteries with hybrid electrolyte was investigated in Chapter 2. The RGO-Co(mqph) showed high onset potential (-0.06 V vs. Ag/AgCl) under oxygen condition in the rotating disk electrode system for oxygen reduction reaction, which was higher than that of RGO (-0.13 V vs. Ag/AgCl). Furthermore, the ORR mechanism of RGO-Co(mqph) showed 3.52 electron pathway. On the other hand, the RGO only exhibited the electron transfer number of 2.2 for ORR. Moreover, the electrochemical performance of Li-air batteries with hybrid electrolyte showed that the RGO-Co(mqph) provided good discharge performance and cycle performance. It was thus considered that the Co(mqph) strongly affected ORR activity for cathode electrode. This was ascribed to synergic effect due to combination between RGO and Co(mqph).

The use of advanced carbon materials as an air electrode in hybrid Li-air batteries was

thought to improve electrochemical performances such as cycle stability and a low voltage gap between discharge and charge. In chapter 3, a carbon nanofiber grown on carbon black (CNF-CB) was prepared by chemical vapor deposition (CVD) method at different temperatures (640-840 °C), and the electrochemical performance of hybrid Li-air batteries based on the CNF-CB electrodes was investigated. The Li-air cell based on CNF-CB 740, with a cut-off voltage in the range 2.5-4.2 V at 0.5 mA cm<sup>-2</sup>, showed good cycle stability, and demonstrated about 75 cycles (about 300 h) without an obvious increase in charge voltage.

## TABLE OF CONTENTS

ABSTRACT.....	I
TABLE OF CONTENTS .....	III
LIST OF FIGURES .....	VI
LIST OF TABLES .....	XI
Chapter 1. General Introduction .....	1
1.1 Lithium-oxygen battery .....	1
1.1.1 Brief introduction of lithium-oxygen (Li-O <sub>2</sub> ) battery .....	1
1.1.2 Composites and Working principle of Li-O <sub>2</sub> battery .....	4
1.2 Various Li-O <sub>2</sub> batteries .....	4
1.2.1 Organic (aprotic) electrolyte Li-O <sub>2</sub> battery .....	4
1.2.2 Aqueous electrolyte Li-O <sub>2</sub> battery .....	5
1.2.3 Solid-state electrolyte Li-O <sub>2</sub> battery .....	6
1.2.4 Hybrid (mixed) electrolyte Li-O <sub>2</sub> battery .....	6
1.3 Issue of organic electrolyte Li-O <sub>2</sub> battery .....	7
1.3.1 Issue for anode and electrolyte part .....	7
1.3.2 Issue for cathode part .....	8
1.3.3 Catalyst material for cathode of organic electrolyte Li-O <sub>2</sub> battery .....	8
1.4 The hybrid electrolyte Li-air battery .....	10
1.4.1 Hybrid electrolyte Li-air battery .....	10
1.4.2 Issue of hybrid electrolyte Li-air battery .....	11
1.4.3 Catalyst material for hybrid electrolyte Li-air battery .....	11
1.5 Target and outline of this thesis .....	17

1.5.1 Motivation of this research .....	18
1.5.2 Target of this research.....	21
1.5.3 Outline of this thesis .....	21
1.6 Reference .....	22
Chapter 2. Investigation organic metal complexed catalyst with reduced graphene oxide (RGO) composite to reduce discharge overpotential gap .....	25
2.1 Introduction.....	25
2.2 Experimental .....	26
2.2.1 Preparation of reduced graphene oxide (RGO) .....	26
2.2.2 Preparation of organic metal complexed catalyst (Co(mqph)).....	27
2.2.3 Preparation of reduced graphene oxide with organic metal complexed (RGO-Co(mqph)).....	28
2.2.4 Fabrication of hybrid electrolyte Li-aur battery and electrochemical test .....	29
2.2.5 Characterization .....	32
2.3 Results and Discussion .....	32
2.3.1 The characteristic changing and heat treatment effect for RGO.....	32
2.3.2 The characteristics for RGO with RGO-Co(mqph) .....	37
2.3.3 Electrochemical performance for RGO-Co(mqph) .....	41
2.4 Conclusions.....	52
2.5 References.....	53
Chapter 3. Investigation of grown carbon nanofiber on carbon black (CNF-CB) to improve cycle performance.....	56
3.1 Introduction.....	56
3.2 Experimental .....	57
3.2.1 Preparation of CNF-CB .....	57

3.2.2 Assembly and testing of hybrid Li-air battery .....	59
3.2.3 Characterization .....	60
3.3 Results and Discussion .....	60
3.3.1 The characteristics for CNF-CB .....	60
3.3.2 Analysis of electrochemical characterization for CNF-CB series .....	67
3.3.3 The effect of remained Ni <sub>3</sub> Fe metallic particles for characterization and electrochemical performance of CNF-CB series .....	77
3.4 Conclusions.....	82
3.5 Reference .....	82
Chapter 4 Conclusions .....	84
List of Research Results.....	86
Acknowledgement .....	87

## List of Figures

Figure 1-1. The gravimetric energy densities for various types of rechargeable batteries compared to gasoline .....	3
Figure 1-2. Schematics of Li-O <sub>2</sub> battery .....	4
Figure 1-3. Schematics of organic (aprotic) electrolyte Li-O <sub>2</sub> battery .....	5
Figure 1-4. Schematics of aqueous electrolyte Li-O <sub>2</sub> battery .....	5
Figure 1-5. Schematics of solid-state electrolyte Li-O <sub>2</sub> battery.....	6
Figure 1-6. Schematics of hybrid elec.trolyte Li-O <sub>2</sub> battery.....	7
Figure 1-7. Schematics of Lithium dendrite formation .....	8
Figure 1-8. Schematics of hybrid electrolyte Li-air battery.....	10
Figure 2-1. Schematics of Co(mqph).....	26
Figure 2-2. The diagram for preparation of organic metal complexed catalyst (Co(mqph)). .....	28
Figure 2-3. The diagram for synthesise reduce graphene oxide with Co(mqph). .....	29
Figure 2-4. The schematics for hybrid electrolyte Li-air battery and the component ratio for cathode. ....	30
Figure 2-5. The image for rotating disk electrode (RDE) system (a) and schematics of cross section for working electrode (b), respectively.....	31
Figure 2-6. XRD pattern for Li <sub>2</sub> CO <sub>3</sub> and RGO after discharge for 20 h. ....	32
Figure 2-7. The comparison of XRD pattern for 1-step RGO and 2-step RGO.. .....	33
Figure 2-8. The TG-DTA for 1-step RGO (a) and 2-step RGO (b), respectively. The temperature increased from room temperature to 900 °C.....	34
Figure 2-9. The comparison of FTIR for 1-step RGO and 2-step RGO. ....	35

Figure 2-10. The cyclic performance at a current density of 0.5 mA/cm <sup>2</sup> for 2 hr to each discharge-charge under hybrid electrolyte conditions for 1-step RGO and 2-step RGO, respectively .....	37
Figure 2-11. The XRD pattern for Co(mqph), RGO-Co(mqph) and RGO.....	38
Figure 2-12. The SEM and TEM image of RGO (a),(c) and RGO-Co(mqph) (b),(d), respectively. ....	39
Figure 2-13. The XDX mapping of RGO-Co(mqph) from TEM image. ....	40
Figure 2-14. The XPS (X-ray Photoelectron Spectroscopy) analysis for RGO and RGO-Co(mqph) composite.....	40
Figure 2-15. The thermal gravimetric analysis for Co(mqph), RGO and RGO-Co(mqph) composite, respectively.....	41
Figure 2-16. The cycle voltammetry (CV) for 20wt% Pt-CB (a), RGO-Co(mqph) (b) and RGO (c), respectively at 20mV/s, 500 rpm, under 1M LiOH solution in pure N <sub>2</sub> and O <sub>2</sub> saturated condition. ....	42
Figure 2-17. The linear sweep voltammetry (LSV) for 20wt% Pt-CB, RGO-Co(mqph) and RGO, respectively at 20mV/s, 500-1500 rpm, under 1M LiOH solution in pure O <sub>2</sub> saturated condition. ....	43
Figure 2-18. The K-L plots determined from LSV data at -0.5 V for 20wt% Pt-CB, RGO-Co(mqph) and RGO, respectively .....	44
Figure 2-19. The diagram for ORR mechanism with 4-electron and 2-electron under alkaline electrolyte. ....	46
Figure 2-20. The discharge performance for RGO, RGO-Co(mqph) and 20wt% Pt-CB under 1M LiOH solution at 0.5 mA cm <sup>-1</sup> during 24 hours.....	47
Figure 2-21. The cycle performance under 1M LiOH solution at 0.5 mA cm <sup>-1</sup> , discharging and charging time each 2 h during 30 cycle for RGO (a), RGO-Co(mqph) (b) and 20wt% Pt-CB (c), respectively. ....	49
Figure 2-22. The discharge and charge potential of whole measured samples for each	

cycle for RGO, RGO-Co(mqph) and 20wt% Pt-CB, respectively. ....	50
Figure 2-23. XPS spectra of C <sub>1s</sub> (a) and O <sub>1s</sub> (b) for RGO and RGO-Co(mqph), respectively. ....	51
Figure 2-24. The sp <sup>3</sup> /sp <sup>2</sup> hybridization ratio of the RGO and RGO-Co(mqph) (a) was estimated by integrating the corresponding component against the binding energy for XPS peaks. And the Raman spectroscopy and I <sub>G</sub> /I <sub>D</sub> value for RGO and RGO-Co(mqph) (b). ....	52
Figure 3-1. Preparation of CNF-CB by chemical vapour deposition (CVD) on different temperature from 640 °C to 840 °C. ....	59
Figure 3-2. The XRD pattern of CNF-CB from 20° to 80° of 2 theta degrees. And the peak intensity, which corresponded with Ni <sub>3</sub> Fe of metallic composite. ....	61
Figure 3-3. The thermo gravimetric (TG) and differential thermal analysis (DTA) curve from room temperature to 900 °C of temperature range under air condition (100 ml min <sup>-1</sup> ) and the 10 °C min <sup>-1</sup> of temperature raising speed for CNF-CB 640, CNF-CB 740 and CNF-CB 840, respectively. ....	62
Figure 3-4. The hysteresis loop and BET specific surface area for CNF-CB 640, CNF-CB 740 and CNF-CB 840, respectively. ....	64
Figure 3-5. The Raman spectroscopy (a) and comparison of I <sub>D</sub> /I <sub>G</sub> ratio from intensity value of D-band and G-band as Raman result for CNF-CB 640, CNF-CB 740, CNF-CB 840 and CB, respectively. ....	65
Figure 3-6. The SEM images for CNF-CB 640, CNF-CB 740, CNF-CB 840 and CB, respectively. ....	66
Figure 3-7. The TEM images for CNF-CB 640, CNF-CB 740, CNF-CB 840 and CB, respectively. ....	67
Figure 3-8. The cycle voltammetry (CV) analysis at a scan rate of 20 mV s <sup>-1</sup> with a rotating rate of 500 rpm under 0.1M KOH in N <sub>2</sub> and O <sub>2</sub> condition for CNF-CB 640, CNF-CB 740, CNF-CB 840 and CB, respectively. ....	68

Figure 3-9. The linear sweep voltammetry (LSV) analysis at a scan rate of 20 mV s <sup>-1</sup> with a rotating rate of 500 rpm to 1500 rpm under 0.1M KOH in O <sub>2</sub> condition for CNF-CB 640, CNF-CB 740, CNF-CB 840 and 20wt% Pt-CB, respectively.....	69
Figure 3-10. The Koutechky-Levich (K-L) plots corresponded LSV result of 20 wt% Pt-CB, CNF-CB 640, CNF-CB 740 and CNF-CB 840, respectively. ....	70
Figure 3-11. The discharge performance at a current density of 0.5 mA cm <sup>-1</sup> for 24 h under hybrid electrolyte for CNF-CB 640, CNF-CB 740 and CNF-CB 840, respectively. ....	71
Figure 3-12. The discharge-charge performance at a current density of 0.5 mA cm <sup>-2</sup> each 2 h under hybrid electrolyte for CNF-CB 640, CNF-CB 740 and CNF-CB 840, respectively.. ....	73
Figure 3-13. The discharge and charge voltages obtained for all measured samples during cycling at a range of 2.5 to 4.2 V for CNF-CB 640, CNF-CB 740, CNF-CB 840 and CB, respectively.. ....	74
Figure 3-14. The discharge rate performance of hybrid Li-air batteries with CNF-CB 640, CNF-CB 740, CNF-CB 840 and CB electrodes at various current densities up to 1.5 mA cm <sup>-2</sup> .....	75
Figure 3-15. The internal resistance for CNF-CB 640, CNF-CB 740, CNF-CB 840 and CB electrodes by analysing the I-V curve at various current densities up to 1.5 mA cm <sup>-2</sup> . ....	76
Figure 3-16. The XRD pattern for CNF-CB 740 before acidic wash with corresponded intensity of Ni <sub>3</sub> Fe at range 20 to 80 ° of 2 theta.....	78
Figure 3-17. The thermo gravimetric (TG) and differential thermal analysis (DTA) curve from room temperature to 900 °C of temperature range under air condition (100 ml min <sup>-1</sup> ) and the 10 °C min <sup>-1</sup> of temperature raising speed for CNF-CB 740 before acidic wash.....	79
Figure 3-18. The discharge-charge performance for 1 <sup>st</sup> cycle at a current density of 0.5 mA cm <sup>-2</sup> each 2 h under hybrid electrolyte for CNF-CB 740 after acidic wash (a) and	

before acidic wash (b), respectively. .... 80

Figure 3-19. The discharge-charge performance at a current density of  $0.5 \text{ mA cm}^{-2}$  each 2 h under hybrid electrolyte for CNF-CB 740 before acidic wash. .... 81

## LIST OF TABLES

Table 1-1. Different catalyst material for hybrid electrolyte Li-air battery with their synthetic details and result .....	11
Figure 3-1. The ratio of remained amount for Ni <sub>3</sub> Fe in CNF-CB 640, CNF-CB 740 and CNF-CB 840 after acidic wash by HCl solution .....	62
Figure 3-2. The BET surface area for CNF-CB 640, CNF-CB 740, CNF-CB 840 and CB .....	63
Figure 3-3. The onset potential of CNF-CB 640, CNF-CB 740, CNF-CB 840 and CB for oxygen reduction reaction (ORR) .....	68
Figure 3-4. The electron transferred number of 20wt% Pt-CB, CNF-CB 640, CNF-CB 740, CNF-CB 840 and CB for ORR.....	71
Figure 3-5. The comparison of BET surface area for CNF-CB 740 before acidic wash with after acidic wash .....	81

# Chapter 1. General introduction

## 1.1 Lithium oxygen battery

### 1.1.1 Brief introduction of lithium-oxygen (Li-O<sub>2</sub>) battery

In 18<sup>th</sup> century, the revolution of transportation and industrial facilitated mass production and mass transportation, which improved humanity more convenient. Nevertheless, the industrialization was developed continuously due to the humanity want higher technology. However, the more industrialization was improved, nature was destroyed. Especially, air pollution was became primary reason for several negative effect such as smog and greenhouse effect. Therefore, many nations discussed on environment protection forum such as Kyoto protocol at 2005 and Paris agreement at 2015, respectively. Advanced countries were agreed to reduce greenhouse gases such as carbon dioxide gas (CO<sub>2</sub>), methane gas (CH<sub>4</sub>), nitrous oxide (N<sub>2</sub>O), perfluorinated carbon (PFC), hydrofluoro carbon (HFC) and sulfur hexafluoride (SF<sub>6</sub>) in Kyoto protocol. Nevertheless, greenhouse gases were increased gradually at every years. Therefore, new convention from Paris was announced instead of Kyoto protocol. This agreement regulated that whole countries have to reduce greenhouse gases including developing countries from 2021.

Therefore, the green energies such as solar generation and wind generation were investigated to reduce greenhouse gases during electric generations. Although these power sources were used instead of thermal power plant, it showed poor efficiency. Thus, the amount of produced electric power was not enough to cover that. Moreover, it has disadvantage for large space and first cost to install infrastructure. To solve these problems, many methods were studied for example improving efficiency and cooperation with architecture.

Furthermore, the improvement of transportation and increase of vehicles were largest obstacle to reduced CO<sub>2</sub> gas. Accordance with global research insight, the amount of vehicles increasing every year, it will be over 1 million at 2018. Thus, exhaust gas also will increase which will accelerate greenhouse effect as well as interruption to reduce CO<sub>2</sub>. Those problems became a main reason to investigate new transportation method

such as electric vehicles (EV) and hybrid electric vehicles (HEV) to use instead of gasoline engine.

At this time, Li-ion batteries (LIB) were usually used power sources of EV and HEV. Because, LIB showed high stability for long cycle performance. However, it also has serious problems for low power density and low energy density which make critical drawbacks. First, the limitation for application was occurred. The low power density of LIB was not enough to operate huge application such as bus and industrial vehicles. Second, the limitation for possible driving distance by one charge was occurred from low energy density. The EV, which used LIB for power sources, can drive only 250 km. It was not satisfied for needs of customers. In addition, many kind of international energy research institute such as NEDO established aim to increase possible driving distance of EV to 500 km until 2020 as one time charge.

Therefore, many kind of power sources such as fuel-cell, super capacitor and metal-air batteries were investigated to use power sources of EV and HEV. Among these power sources, the fuel-cell has largest energy density than that of other power sources which was benefit for power source of EV and house. However, its high cost interrupted to be commercial products. In contrast, capacitor showed highest power density among other power sources which was suitable to use for huge application such as bus and industrial vehicles. However, it also showed drawbacks for low energy density. These serious problems were considered highest barrier to use power source of EV.

On the other hands, the metal-oxygen batteries were regarded suitable power sources of EV. Because, metal-oxygen battery has more theoretical energy density as well as higher power density than that of LIB. The metal-oxygen batteries were used active metal such as Al, Zn, Mn and Li for anode and various porous carbon materials were used for cathode. Especially, Lithium-oxygen (Li-O<sub>2</sub>) battery showed highest theoretical energy density among all of metal-oxygen batteries. For the past few decades, interest in Li-O<sub>2</sub> batteries increased due to its extremely high energy density and gravimetric energy, which is three to four times that of Li-ion batteries [1-5]. In contrast, it was considered structural problems that Li-O<sub>2</sub> battery have to use pure oxygen gas bombe. Therefore, Li-air battery was investigated to solve structural problems, due to it was supplied oxygen gas the air instead of gas bombe. Especially, non-aqueous electrolyte Li-air battery was widely investigated because of it has an

advantage for the energy density ( $3504 \text{ Wh kg}^{-1}$ ). However, the practical energy density of non-aqueous electrolyte Li-air batteries is limited by the deposition of the insoluble discharge product such as  $\text{Li}_2\text{O}_2$  and  $\text{LiO}_2$ , which caused the cycle performance fading due to clog air path way on cathode. To overcome this problem, a hybrid Li-air batteries system has been developed, composed of a non-aqueous electrolyte in the anode side and an aqueous electrolyte in the cathode side, separated by Li conducted solid state separate [6-10]. Our group also has reported that the hybrid Li-air batteries since 2009 [11-14]. In the basic electrolyte, the overall reaction of Li-air batteries is  $2\text{Li} + \text{H}_2\text{O} + 1/2\text{O}_2 \leftrightarrow 2\text{LiOH}$ , and theoretical cell potential is 3.43 V [10-14]. However, the hybrid Li-air batteries were still in a developing to overcome the large discharge-charge overpotential gap and cycle stability. Therefore, the development of an electrocatalyst with highly active and stable for the ORR and oxygen evolution reaction (OER) was one of the most attractive challenges in hybrid Li-air batteries.

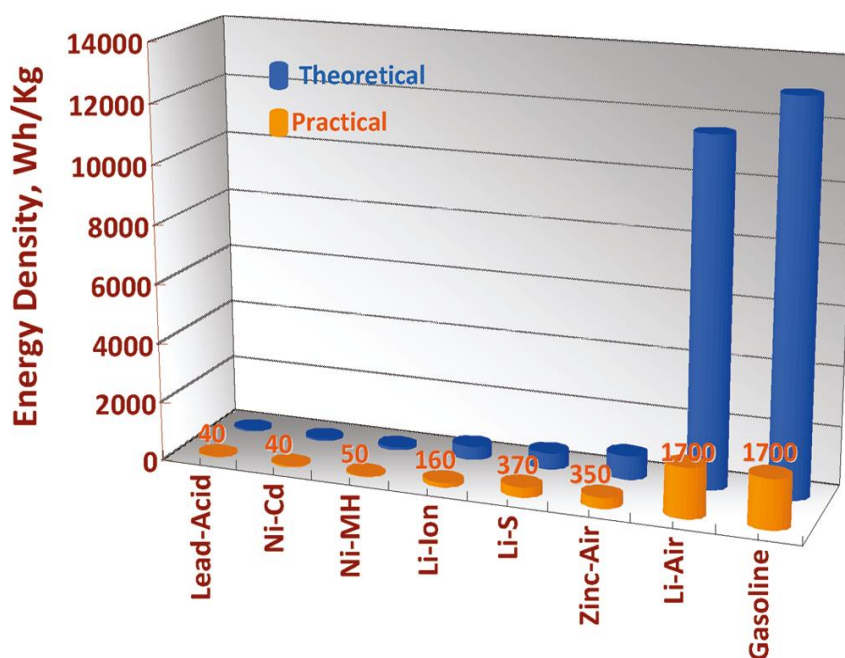


Figure 1-1. The gravimetric energy densities for various types of rechargeable batteries compared to gasoline [15].

### 1.1.2 Composites and working principle of Li-O<sub>2</sub> battery

Figure 1-2 showed schematics Li-O<sub>2</sub> battery. The Li-O<sub>2</sub> battery consists of anode, electrolyte and cathode. The lithium metal was used for anode. The cathode used porous material such as activation carbon materials.

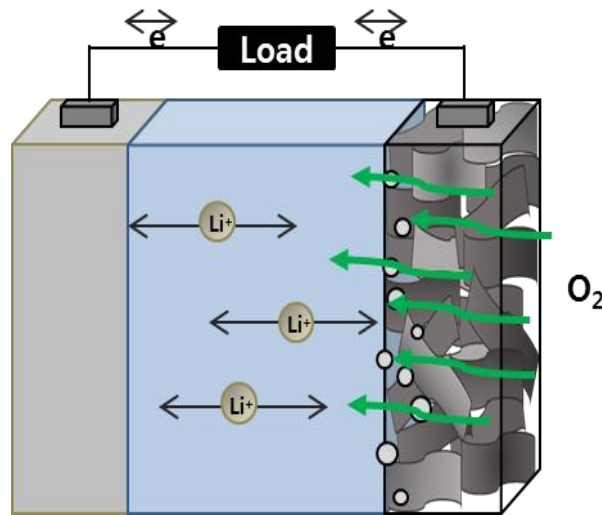


Figure 1-2. Schematics of Li-O<sub>2</sub> battery

The discharge reaction; Li ion was reacted with oxygen on the cathode surface, which reaction was called ORR. And then, it make discharge product, which created discharge product was difference depend on kind of electrolyte. On the other hands, the discharge product was decomposed during charge procedure. The Li ion returned to anode, which reduced Li metal. This phenomenon was called OER procedure.

## 1.2 Various Li-O<sub>2</sub> batteries

Li-O<sub>2</sub> batteries were distinguished depend on using electrolyte, which were organic electrolyte, aqueous electrolyte, solid-state electrolyte and hybrid electrolyte. In this section, we introduced the four kind of Li-O<sub>2</sub> battery with their advantage and challenge points.

### 1.2.1 Organic (aprotic) electrolyte Li-O<sub>2</sub> battery

Figure 1-3 showed schematics of organic electrolyte Li-O<sub>2</sub> battery. This model was investigated first time by Abraham and Zhang et. al. which used porous carbon material and organic solution for cathode and electrolyte, respectively. It was showed larger theoretical energy density over 10 times than that of Li-ion battery.

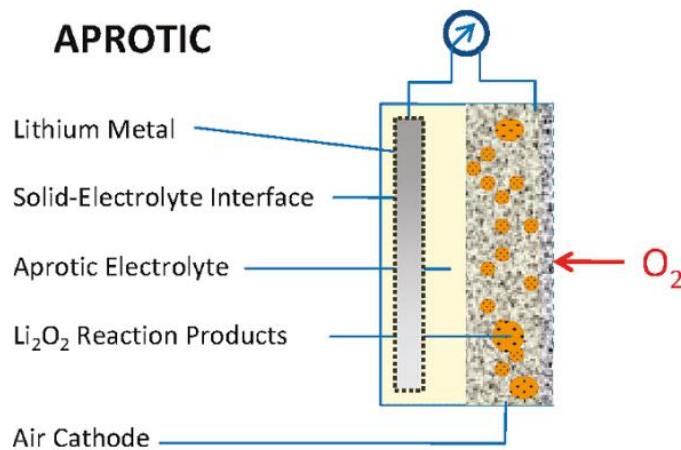


Figure 1-3. Schematics of organic (aprotic) electrolyte Li-O<sub>2</sub> battery [16]

### 1.2.2 Aqueous electrolyte Li-O<sub>2</sub> battery

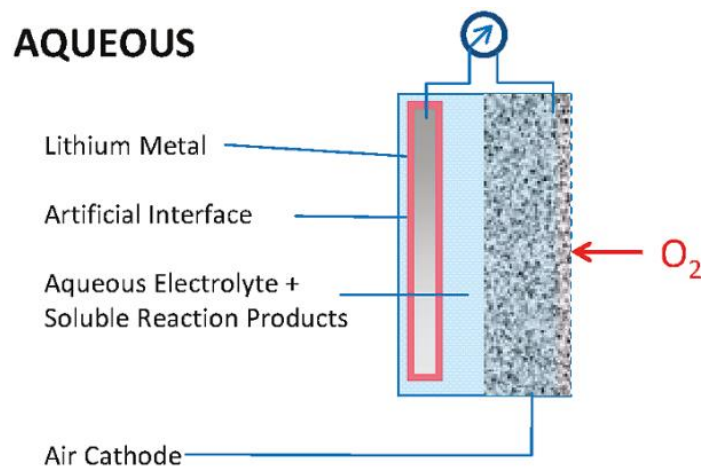


Figure 1-4. Schematics of aqueous electrolyte Li-O<sub>2</sub> battery [16]

Figure 4 was schematics of aqueous electrolyte Li-O<sub>2</sub> battery. The aqueous electrolyte Li-O<sub>2</sub> battery used alkaline and acidic solution such as KOH, LiOH and HCl for electrolyte. This model can be showed advantage for highest power density than that other Li-O<sub>2</sub> battery models. In contrast, it has stability problems between Li metal with electrolyte.

### 1.2.3 Solid-state electrolyte Li-O<sub>2</sub> battery

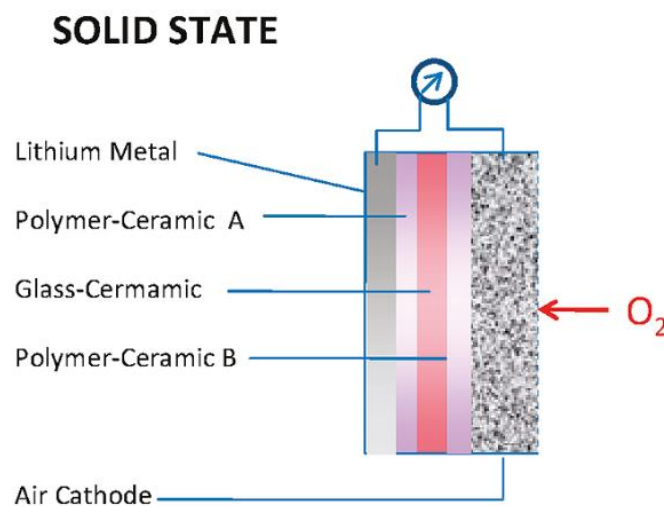


Figure 1-5. Schematics of solid-state electrolyte Li-O<sub>2</sub> battery [16]

Figure 1-5 showed schematics of solid-state electrolyte Li-O<sub>2</sub> battery. The solid state Li-O<sub>2</sub> battery was investigated to improve stability of anode, which used Li ion conduct ceramic membrane such as LiSICON. Even though solid-state electrolyte Li-O<sub>2</sub> battery showed highest stability, its ionic mobility was slow. Moreover, its high resistance also was considered serious problems.

### 1.2.4 Hybrid (mixed) electrolyte Li-O<sub>2</sub> battery

The hybrid (mixed) electrolyte Li-O<sub>2</sub> battery used organic electrolyte and aqueous electrolyte for anode and cathode, respectively (Figure 1-6). Both electrolyte was isolated by Li conducted solid-state membrane such as LiSICON to prevent inter mixed.

It was investigated to overcome drawbacks from discharge product in organic electrolyte Li-O<sub>2</sub> battery. The hybrid electrolyte Li-O<sub>2</sub> battery make soluble discharge product, which can resolve performance fading problems by discharge product.

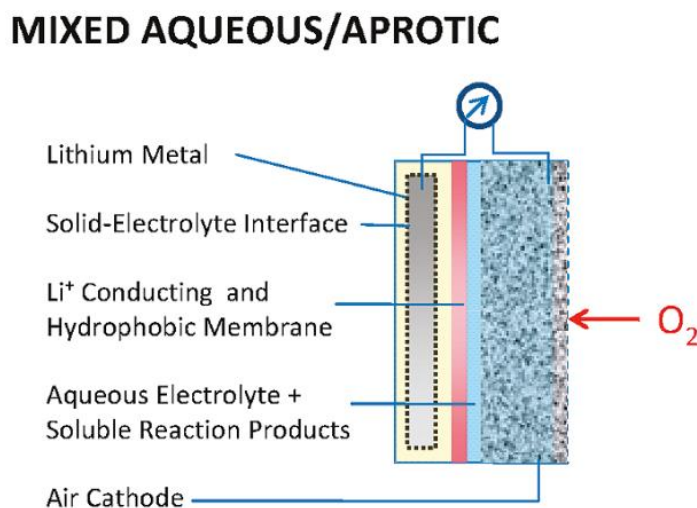


Figure 1-6. Schematics of hybrid electrolyte Li-O<sub>2</sub> battery [16]

### 1.3 Issue of organic electrolyte Li-O<sub>2</sub> battery

The organic Li-O<sub>2</sub> battery was most concentrated among Li-O<sub>2</sub> batteries, because of its highest theoretical energy density. However, it also had challenge points for each part.

#### 1.3.1 Issue for anode and electrolyte parts

Figure 1-7 showed formation of Lithium dendrite during cycling performance in the organic (aprotic) Li-O<sub>2</sub> battery. The growth of lithium dendrite grown on the lithium metal surface as anode gradually, which was damaged separator finally. As a result, the short problems was occurred inside of Li-O<sub>2</sub> battery under organic electrolyte.

Furthermore, the electrolyte parts also have problems such as decomposed. During cycle performance, the electrolyte was decomposed at high charge potential. According

to Kraytsberg et. al. report, the electrolyte, which using propylene carbonate, had decomposed reaction above 4.2 V vs. Li/Li<sup>+</sup> [6]. Furthermore, the evaporation of electrolyte by attendant air also was considered problem.

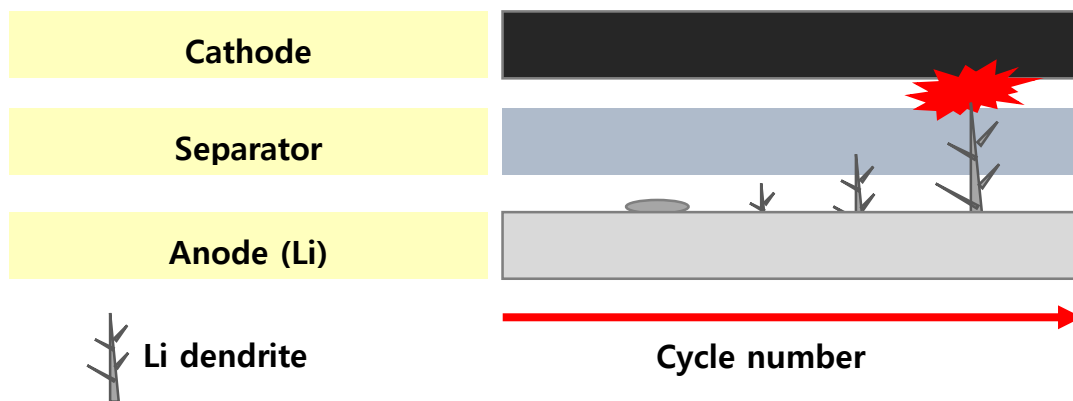


Figure 1-7. Schematics of Lithium dendrite formation

### 1.3.2 Issue for cathode part

The organic electrolyte Li-O<sub>2</sub> battery have each reaction for ORR, it is,



these discharge product such as Li<sub>2</sub>O<sub>2</sub> and LiO<sub>2</sub> was insoluble and solid, which became a main reason of battery performance fading. The most serious problem as cathode part of organic electrolyte Li-O<sub>2</sub> battery was high overpotential gap during cycle performance. In general, the charging overpotential was higher than that of discharging in organic electrolyte Li-air battery, if it used carbon supported material as cathode. The charging overpotential increased above 4 V. Accordance with previous report of Thotiyl et. al., the carbon decomposition began above 3.5 V. Moreover, it occurred side reaction which was Li<sub>2</sub>CO<sub>3</sub> formation [17]. Therefore, many research groups were studied for catalyst material to decrease overpotential gap during cycling performance.

### 1.3.3 Catalyst materials for cathode of organic electrolyte Li-O<sub>2</sub> battery

Many research groups investigated various cathode materials to reduce overpotential gap during cycle performance in organic electrolyte Li-O<sub>2</sub> battery.

Yang et. al. reported for electro catalytic activation of platinum nano particle composite with graphene (PtNP-GNS). In the report, the discharge-charge curves for PtNP-GNS and comparison with bare graphene (GNS). As a result, PtNP-GNS reduced overpotential gap. Nevertheless, it still high overpotential at charging [18].

Ma et. al. reported catalytic activation of MnCo<sub>2</sub>O<sub>4</sub> to improve stability for discharge-charge curve in organic electrolyte Li-O<sub>2</sub> battery. In the reports, the total overpotential gap of MnCo<sub>2</sub>O<sub>4</sub> with Super-P composite was reduced to compare with bare Super-P. Especially, the charge overpotential of MnCo<sub>2</sub>O<sub>4</sub> with Super-P composite was 3.90 V, which was smaller than 4.2 V of bare Super-P [19].

Xin et. al. investigated metal-free carbon composite material, which consist of graphene with activated carbon (G/AC). Their catalytic activation was compared with pristine graphene and pristine ketjen-black. The G/AC showed similar discharge performance with graphene and ketjen-black. In contrast, the charge potential showed different depends on the type of carbon material. The potential of graphene was highest which plateau value was near 4.25 V. The charge potential of ketjen-black on plateau region was about 4 V. On the other hands, the G/AC showed 2 step plateau region for charge curve, which were near 3.5 V and 4 V. As a result, G/AC have an effect to reduce overpotential gap, however that material still showed high overpotential for charging [20]. Ma et. al. group investigated Sr<sub>0.95</sub>Ce<sub>0.05</sub>CoO<sub>3-δ</sub> to improve stability for discharge and charge process. As a result, the Sr<sub>0.95</sub>Ce<sub>0.05</sub>CoO<sub>3-δ</sub> improved ORR, thus it increased discharge capacity from 1400 mAh g<sup>-1</sup> to 2300 mAh g<sup>-1</sup> but also discharge potential under 2.5 V to 2.65 V. In addition, Sr<sub>0.95</sub>Ce<sub>0.05</sub>CoO<sub>3-δ</sub> also effect to reduce charge overpotential from 4.5 V to 4.25 V. Although the Sr<sub>0.95</sub>Ce<sub>0.05</sub>CoO<sub>3-δ</sub> improved stability during discharge-charge, its charging potential was still high over 4 V [21].

Furthermore, metal oxide materials such as α-MnO<sub>2</sub>/Pd composite was also investigated to improve electrochemical properties by Thapa et. al. That materials showed improvement not only stable capacity but also round trip efficiency [22]. Yang et. al. also researched electrochemical catalytic of perovskite structure material (Sr<sub>0.95</sub>Ce<sub>0.05</sub>CoO<sub>3-δ</sub>) for organic electrolyte Li-air battery [23]. Moreover, metal nano

particles catalyst (TiN) and metal composite (Fe/N/C and Cu/Fe) were investigated by Li et. al., Shui et. al. and Ren et. al., respectively. The TiN nano particles have significant role of bi-functional activity for OER and ORR. On the other hands, Fe/N/C composite catalyst had an effect to prevent decomposition of organic electrolyte. Although the Cu/Fe composite catalyst improved ORR activity, it showed decrease of discharge capacity [24,25]. Even though almost catalyst showed effect to be improved electrocatalytic activation, organic electrolyte Li-O<sub>2</sub> battery showed still high overpotential gap for cyclic performance. In addition, the Li-O<sub>2</sub> battery has a structural disadvantage, which was necessary of additional oxygen tank. Because of the Li-O<sub>2</sub> batteries needed pure oxygen gas. Therefore, Zhou et. al. investigated hybrid electrolyte Li-air battery.

## 1.4 The hybrid electrolyte Li-air battery

### 1.4.1 Hybrid electrolyte Li-air battery

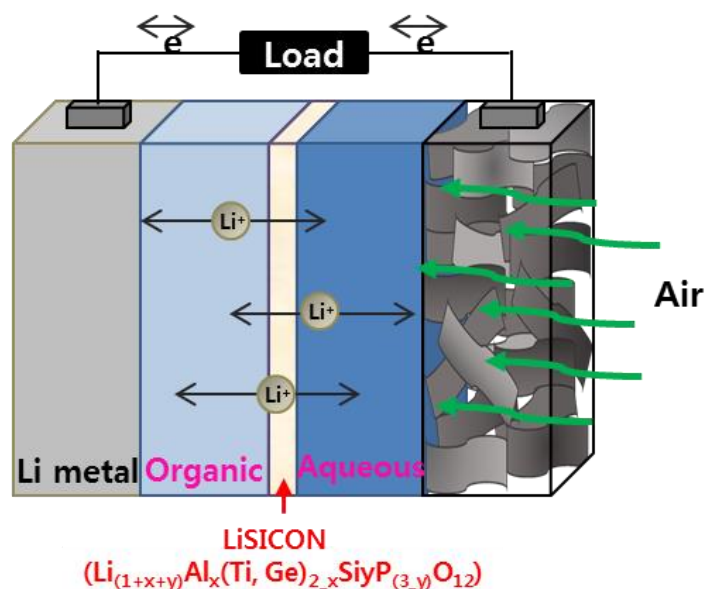


Figure 1-8. Schematics of hybrid electrolyte Li-air battery

The figure 1-8 showed schematics of hybrid electrolyte Li-air battery. The hybrid electrolyte Li-air battery used oxygen in the air, therefore the module was more

convenience than that of before. Moreover, the aqueous electrolyte of anode site supplied few advantages. First, the discharge potential was higher than organic Li- O<sub>2</sub> battery. The theoretical ORR mechanism of hybrid electrolyte Li-air battery under basic electrolyte was,



it has higher discharge potential than that of organic Li-O<sub>2</sub> battery. Thus, the power density of hybrid electrolyte Li-air battery was improved, which is more than organic electrolyte Li-O<sub>2</sub> battery suitable for huge applications.

Second, it can be improved battery performance. The discharge product of organic electrolyte occurred negative side effect for cycle performance.

### 1.4.2 Issue of hybrid electrolyte Li-air battery

Due to the hybrid electrolyte Li-air battery produce soluble discharge product, it can be prevented drawbacks about performance fading by discharge product. Thus, the hybrid electrolyte Li-air battery has not only improvement of battery performance but also reduced overpotential gap in comparison with organic electrolyte Li-O<sub>2</sub> battery. Nevertheless, the overpotential gap of hybrid electrolyte Li-air battery was still high due to low catalytic activity for carbon material. Therefore, many research group investigated various catalyst materials as cathode of hybrid electrolyte Li-air battery to improve stability of discharge-charge performance.

### 1.4.3 Catalyst materials for hybrid electrolyte Li-air battery

Table 1-1. Different catalyst material for hybrid electrolyte Li-air battery with their synthetic details and result

The catalyst material	Synthesis procedure	Optimized amount	Improvement	Analysis	Reference

CNT array grown on carbon fiber paper	The metal alloy catalyst was coated on commercial carbon paper. Then, CNT was grown on the coated carbon paper by PECVD		The discharge capacity was increased. And it showed good cycle performance	The high surface area and low internal resistance.	9
TiN(nano size)	Commercial	85 wt%	Improvement electron transferred number to 4 electron pathway	The high electrical conductivity of titanium nitride (TiN) and small particle size improve ORR	14
Pt-Au nano particles with carbon	To reduce H <sub>2</sub> AuCl <sub>4</sub> and H <sub>2</sub> PtCl in oleylamine and then loaded on carbon (XC-72)	40 wt%	Discharge overpotential and charge overpotential were decreased	The surface Pt and Au atoms on PtAu/C were responsible for ORR and OER kinetics, respectively	26
Pt/IrO <sub>2</sub> -CNT	K <sub>3</sub> IrCl <sub>6</sub> loaded on CNT (by reflux	10wt% IrO <sub>2</sub> and 5wt% Pt	OER activity was improved	The bi-functional catalytic	27

	condition) then annealing (for IrO <sub>2</sub> ). And then Pt loaded on IrO <sub>2</sub> /CNT (by polyol)		(vs. Pt-C) and increased round trip efficiency from 72% to 81%.	activation of Pt-IrO <sub>2</sub> improved OER performance	
Graphene nano sheet (after heat treatment)	Graphene was prepared by Hummer's method, which was reduced by hydrazine. And then, that had a heat treatment at 950 °C for 30 min in Ar/H <sub>2</sub> gas.	90 wt%	It showed low overpotential and stable cycle performance.	The carbon crystallization was improved and the functional group of carbon surface was removed after heat treatment.	28
N doped graphene nano sheets	The graphene oxide has heat treatment at 850 °C in NH <sub>3</sub> for 2h	90 wt%	This material showed improvement for ORR, moreover its internal resistance also very small	The pyridine-type N with a large proportion of edge site in the N-doped GNS may play a positive role for improvement	29

				t of ORR	
O- and N-doped carbon nanoweb	The N-CNW was prepared by oxidative template assembly method. Then, N-CNW was heat treatment with KOH powder at 600 °C	1 mg cm <sup>-1</sup>	ON-CNW showed ORR improvement and similar cell efficiency with commercial Pt/C	The CNW structure has better to improve electron and mass transport. And the synergistic effect of O and N groups made high ORR	30
NiCo <sub>2</sub> O <sub>4</sub> (without carbon)	Ni(NO <sub>3</sub> ) <sub>2</sub> 6H <sub>2</sub> O, Co(NO <sub>3</sub> ) <sub>2</sub> 6H <sub>2</sub> O and hexamethylene-tetramine had hydro thermal method at 90 °C.	1.0 mg cm <sup>-1</sup>	High OER activity and good electrochemical stability for OER process.	This material was free for binder and carbon material. Therefore, it avoids performance fading by carbon support degradation. And high electrochemical and mechanical	31

				stability of NiCo <sub>2</sub> O <sub>4</sub> .	
Co <sub>3</sub> O <sub>4</sub> (micro sphere) with Cu (nano particle)	The hydrothermal method for Co <sub>3</sub> O <sub>4</sub> and the polyol method for Cu nano particle loading on Co <sub>3</sub> O <sub>4</sub>		Co <sub>3</sub> O <sub>4</sub> -Cu showed stable bi-functional catalytic activity, which similar with precious catalyst material.	The synergistic effect Co <sub>3</sub> O <sub>4</sub> with Cu.	32
Co <sub>3</sub> O <sub>4</sub> nano cristal with ON-CNW	The N-CNW was prepared by oxidative template assembly method. Then, N-CNW was heat treatment with KOH powder at 600 °C for ON-CNW. Co <sub>3</sub> O <sub>4</sub> /ON-CNW was prepared by refluxed method.	80 wt%	The long cycle performance and high durability for long cycle.	The synergistic effect for good structure of carbon nanoweb and strong catalytic activation of Co <sub>3</sub> O <sub>4</sub> with O-,N-functional group.	33
CoMn <sub>2</sub> O <sub>4</sub>	The hummer's	30 wt%	The ORR	The	34

grown on Graphene	method for graphene and the hydrothermal method for CoMn <sub>2</sub> O <sub>4</sub> /graphene		electron transferred number was improved and OER on set potential also improved.	graphene showed little electrochemical activation but it made synergetic effect with CMO.	
Co/N/rGO(NH <sub>3</sub> )	The graphene (rGO) was prepared by Marcano method. The rGO and Co(NO <sub>3</sub> ) <sub>2</sub> ·6H <sub>2</sub> O with PEI was dissolved in DI water and heat treatment at 850 °C in NH <sub>3</sub> for 30 min.		The electron transferred number for ORR was improved (n=3.9) and the durability also showed higher than that of Pt.	The morphology of rGo was facilitated the create active Co-N <sub>x</sub> site and to improve the catalytic activity for ORR.	35
La <sub>1.7</sub> Sr <sub>0.3</sub> NiO <sub>4</sub> (perovskite)	La(NO <sub>3</sub> ) <sub>3</sub> ·6H <sub>2</sub> O, Sr(NO <sub>3</sub> ) <sub>2</sub> ·4H <sub>2</sub> O and Ni(NO <sub>3</sub> ) <sub>2</sub> ·6H <sub>2</sub> O dissolved in DI water and ethylene glycol. And citric acid	20 wt%	La <sub>1.7</sub> Sr <sub>0.3</sub> NiO <sub>4</sub> showed bi-functional catalytic activation and the stability of cycle performance	The strong catalytic activation for La <sub>1.7</sub> Sr <sub>0.3</sub> NiO <sub>4</sub> .	36

	<p>solution was added to the solution and heat and drying. And another heat treatment at 900 °C for 5h.</p>		also improved.		
FePc-CNT	<p>The CNT and FePc were dissolved in ethanol, which ratio was 2:1. Then, it has evaporation process and dried.</p>	90 wt%	<p>The discharge performance and cyclic performance stability were improved.</p>	<p>The electro catalytic activation of FePc had synergetic effect with CNT.</p>	37
GO/CNT	<p>The hummer's method for GO. The evaporation to composite GO with CNT.</p>	90 wt%	<p>The catalytic activation improved for oxygen reduction.</p>	<p>The oxygen contained functional group of GO with electrical conductivity of CNT made synergetic effect for ORR</p>	38

## 1.5 Target and outline of this thesis

### 1.5.1 Motivation of this research

The research and improvement of Li-air battery for longer cycle performance, higher stability and stronger durability was positively necessary to reduce for rate of increase environment pollution and to save human society and earth through to achieve commercial of electric vehicles (EV). The one of most important factor was improvement of cathode material, due to it could determine not only the cost but also ability of Li-air battery performance. Present, many kinds of catalyst were investigated to improve electrochemical activity such as ORR and OER for hybrid electrolyte Li-air battery. Precious and rare metal such as Pt, Au, La and Ir with their composite were used to improve battery performance during discharge-charge performance. Furthermore, transition metal such as Fe, Mn and Ni with their composite and their oxide material also have been investigated. Course, those materials showed excellent electro catalytic activation as well as to be developed electrochemical performance. Nevertheless, those materials also showed several serious drawbacks,

- The precious metal catalyst such as Pt, Au, Ag and their composite;  
Even though precious metal catalyst species showed best catalytic activation to improve electro catalytic activation for oxygen reduction and oxygen evolution in aqueous electrolyte, its poor stability and extremely high cost were considered serious drawback to make commercial product.
- The non-precious metal catalyst and their various composite;  
Instead of precious metal catalyst, the transition metal material such as Fe, Mn, Ce, Ni, Cu, their oxide and their composite were used for alternative catalyst material. Although that showed advantage for cost than that of precious catalyst, its catalytic activation was weaker than that of precious material. Therefore, it was necessary for more research to using commercial product.

Moreover, the metallic catalyst species has a common drawback. The metallic catalyst materials were supported by porous material, which was carbon material for almost cases. From the previous reports, many research groups demonstrated that carbon oxidation occurred on high potential for charging, especially. Furthermore, the high catalytic activity of metallic material was acceleration of carbon oxidation during

discharge-charge procedure [26, 38, 39]. Therefore, it was concentrated that metal-free catalyst was investigation to overcome limitation of metallic catalyst for last several years.

- The nano structure carbon such as graphene (RGO), carbon nano tube (CNT); The nano structure carbons were concentrated for cathode material because their structure advantage such as large surface area and high electric conductivity than that of activated carbon material such as Super-P, ketjen-black and acethylene-black. Therefore, the nano structure carbon material showed moderate electro catalytic activation for hybrid electrolyte Li-air battery system. Furthermore, those have cheapest cost than that other catalyst material for example precious metal, metal oxide, transition metal and their composite.

However, the nano structure carbon had critical problems for low duration for cyclic performance. Because of the potential was changed for drop and rising to low potential level to high potential level to low potential level during discharge-charge procedure. This repetition was not only damage for carbon material but also to become a main reason for performance degradation.

Course, the various catalyst materials were investigated and those material showed advanced electrochemical performance in hybrid electrolyte Li-air battery. However, those materials also showed several serious problems.

Therefore, hybrid electrolyte Li-air battery still needed to investigate new catalyst material for improvement of cycle performance and their stability. In general, the catalytic performance associated with carbon properties. Because of the various carbon was used to support material of catalyst material in almost catalyst synthesise case. Furthermore, many previous reports also showed different catalytic activity dependence with kind of carbon materials. In previous report of Xin et. al. group, the graphene, activated carbon with their composite carbon was investigated for electro catalytic activation in organic Li-O<sub>2</sub> battery model. All of carbon material showed difference for battery performance such as discharge capacity and the overpotential gap during discharge-charge process [20]. Wang et. al. researched about electro catalytic activation of graphene comparison with ketjen-black in hybrid electrolyte Li-air battery model.

Each carbon showed difference battery performance such as overpotential gap and discharge capacity [40]. From these previous reports, thus, the each carbon showed difference battery performance without kind of electrolyte. Because of each carbon had different mechanical properties such as surface area, pore size, carbon crystalline and functional groups. These previous reports showed catalytic role, when various carbon materials use for catalyst in Li-air battery. On the other hands, Yoo et. al. reported electrochemical performance for FePc with various carbon material composite in hybrid electrolyte Li-air battery. When graphene, CNT and AB were used support material of FePc, their each composite showed different electrochemical performance for ORR and battery cycle performance [34]. Thus, these previous reports indicated that properties of carbon material had an effect for battery performance when it uses catalyst as well as catalyst support material.

Therefore, the excellent catalyst material should be satisfied some condition, Firstly, the good properties carbon should be prepared; the carbon surface area accommodated for discharge products, therefore it can improve discharge capacity. The high graphitization lead to improve electrical conductivity which can reduce internal resistance, moreover it also can improve durability during cycling.

Second, the catalyst should be dispersed uniformly on the carbon surface; if carbon was used support material for other catalyst, it should be dispersed uniformly. In other word, the particle size of catalyst should be small and that is not aggregated. Because of the aggregated catalyst has difficulty to show equal performance. Moreover, it has possibility to be main reason of carbon decomposition more easily. Because of the reaction will concentrate around bulk of catalyst, which can make damage for carbon surface.

Third, catalyst should be has good marketability; the precious metal catalyst such as Pt, Au already showed excellent performance for ORR and OER in almost energy storage system. Nevertheless, its extremely high cost interrupted to investigate commercial product. Thus, the catalyst should be low cost and easy for preparation.

Therefore, we choose to improve electrochemical performance such as decrease overpotential gap and better cyclic performance for hybrid Li-air battery by investigation new cathode catalyst material as my doctoral thesis. And I also tried to

give the detailed analysis for the mechanism of improved electrochemical performance.

### **1.5.2 Target of this research**

The targets of this research on investigation catalyst materials for hybrid electrolyte Li-air battery were as follows;

- To improve the electrochemical performance for oxygen reduction by non-precious metal catalyst material.
- To enhance stability for long cycle performance by metal-free catalyst material.
- Detail study the catalytic activation mechanism of catalyst materials and, get the final conclusions.

### **1.5.3 Outline of this thesis**

There are four chapters in this dissertation.

Chapter 1 is a comprehensive review of lithium-air battery. It mainly include a brief introduction about various lithium-air batteries with their drawbacks and cathode materials for Li-air battery under hybrid electrolyte. The research motivation and targets have also been introduced.

In chapter 2, the organic metal complex (Co(mqph)) with reduced graphene oxide (RGO) was synthesized to improve ORR activity in hybrid Li-air battery. The RDE test was used to confirm electro catalytic activity of RGO-Co(mqph), which result was used to calculate electron transfer number for ORR. Furthermore, the battery test was carried out to examine effect of RGO-Co(mqph).

In chapter 3, the CVD method was used to modify metal-free cathode material (CNF-CB) to prevent carbon oxidation by metallic catalyst during discharge-charge performance. Similar techniques with Chapter 2 were applied to study the electrochemical performance.

Chapter 4 is the general conclusion and avenues for future work of this research.

## 1.6 Reference

- [1] J L. Shui, N K. Karan, M Balasubramanian, S Y. Li, D J. Liu, *J. Am. Chem. Soc.*, 134 (2012) 16654-16661.
- [2] V.Viswanathan, K. S. Thygesen, J. S. Hummelshoj, J. K. Norskov, G. Girishkumar, B. D. McCloskey, A. C. Luntz, *The Journal of Chemical Physics*, 135 (2011) 214704.
- [3] M. Wu, J Y. JO, S J Kim, Y K. Kang, H T. Jung, H K. Jung, *RSC Adv.*, 6 (2016) 23467-23470.
- [4] Y L. Cao, F C. Lv, S C. Yu, J. Xu, X. Yang, Z G. Lu, *Nanotechnology*, 27 (2016) 135703.
- [5] Y. Zhang, X. Zhang, J. Wang, W C. McKee, Y. Xu, Z. Peng, *J. Phys. Chem. C*, 120 (2016) 3690-3698.
- [6] A. Kraytsberg, E. Ein-Eli, *Journal of Power Sources*, 196 (2011) 886-893.
- [7] H. He, W. Niu, N. M. Asl, J. Salim, R. Chen, Y. Kim, *Electrochimica Acta*, 67 (2012) 87-94.
- [8] L. Li, X. Zhao. Y. Fu, A. Manthiram, *Phys. Chem. Chem. Phys.*, 14 (2012) 12737-12740.
- [9] Y. Li, Z. Huang, K. Huang, D. Carnahan, Y. Xing, *Energy Environ. Sci.*, 6 (2013) 3339-3345.
- [10] Y. Li, K. Huang, Y. Xing, *Electrochimica Acta*, 81 (2012) 20-24.
- [11] H. Zhou, Y. Wang, H. Li, P. He, *ChemSusChem*, 3 (2010) 1009-1019.
- [12] P. He, Y. Wang, H. Zhou, *Electrochemistry Communications*, 12 (2010) 1686-1689.
- [13] P. He, Y. Wang, H. Zhou, *Chem. Commun*, 47 (2011) 10701-10703.
- [14] Y. Wang, R. Ohnishi, E. Yoo, P. He, J. Kubota, K. Domen, H. Zhou, *J. Mater.*

Chem., 22 (2012) 15549-1555.

[15] G. Girishkumar, B. McCloskey, A. Luntz, S. Swanson and W. Wilcke, *J. Phys. Chem. Lett.* 1 (2010) 2193-2203

[16] Israel National Research Center for Electrochemical Propulsion

[17] Muhammed M. Ottakam Thotily, Stefan A. Freunberger, Zhnaquan Peng, and Peter G. Bruce, *J. Am. Chem. Soc.* 135 (2013) 494-500

[18] Y. Yang, M. Shi, Q-F Zhou, Y-S Li, Z-W Fu, *Electrochemistry Communications* 20 (2010)11-14

[19] S. Ma, L. Sun, L. Cong, X. Gao, C. Yao, X. Guo, L. Tai, P. Mei., Y. Zeng, H.Xie and R. Wang, *J. Phys. Chem. C* 117 (2013) 25890-25897

[20] X. Xin, K. Ito, Y. Kubo, *Carbon* (2016) 99 167-173

[21] Z. Ma, X. Yuan, L. Li and Z-F Ma, *Chem. Commun.*, 50 (2014) 14855-14858

[22] A. K. Thapa, T. Ishihara, *Journal of Power Sources* 196 (2011) 7016-7020

[23] W. Yang, J. Salim, S. Li, C. Sun, L. Chen, J. B. Goodenough and Y. Kim, *J. Mater.Chem.*, 22 (2012) 18902-18907

[24] F. Li, R. Ohnishi, Y. Yamada, J. Kubata, K. Domen, A. Yamada and H. Zhou, *Chem. Commun.*, 49 (2013) 1175-1177

[25] X. Ren, S S. Zhang, D T. Tran and J. Read, *J. Mater. Chem.* 21 (2011) 10118-10125

[26] Y-C. Lu, Z. Xu, H A. Gasteiger, S. Chen, K. Hamad-Schifferli and Y. Shao-Horn, *J. Am. Chem. Soc* 132 (2010) 12170-12171

[27] K. huang, Y. Li, Y. Xing, *Electrochimica Acta*, 103 (2013) 44-49

[28] E. Yoo, H. Zhou, *ACS NANO*, 5 (2011) 3020-3026

[29] E. Yoo, J. Nakamura and H. Zhou, *Energy Environ. Sci.*, 5 (2012) 6928-6932

[30] L. Li and A. Manthiram, *Adv. Energy Mater.*, 4 (2014) 1301795-1301801

[31] L. Li and A. Manthiram, *Nano Energy*, 9 (2014) 94-100

- [32] W. Yang, J. Salim, C. Ma, Z. Ma, C. Sun, J. Li, L. Chen and Y. Kim, *Electrochemistry Communications* 28 (2013) 13-16
- [33] L. Li, S. Liu and A. Manthiram, *Nano Energy*, 12 (2015) 852-860
- [34] L. Wang, X. Zhao, Y. Lu, M. Xu, D. Zhang, R S. Ruoff, K J. Stevenson and J B. Goodenough, *Journal of The Electrochemical Society*, 158(12) (2011) A1379-A1382
- [35] K. Niu, b, Yang, J. Cui, J. Jin, X. Fu, Q. Zhao, J. Zhang, *Journal of Power Source* 243 (2013) 65-71
- [36] K-N. Jung, J-H. Jung, W. Im, S. Yoon, K-H. Shin and J-W. Lee, *ACS Appl. Mater. Interfaces*, 5 (2013) 9902-9907
- [37] E. Yoo, H. Zhou, *Journal of Power Sources* 24 (2013) 429-434
- [38] S. Wang, S. Dong, J. Wang, L. Zhang, P. Han, C. Zhang, X. Wang, K. Zhang, Z. Lan and G. Cui, *J. Mater. Chem.*, 22 (2012) 21051-21056
- [39] S. Jiang, C. Zhu and S. Dong, *J. Mater, Chem. A* 1 (2013) 3593-3599
- [40] L. Wang, M. Ara, K. Wadumestrige, S. Salley, K.Y. Simon Ng, *Journal of Power Sources* 234 (2013) 8-15

# **Chapter 2. Investigation organic metal complexed catalyst with reduced graphene oxide (RGO) composite to reduce discharge overpotential gap**

## **2.1 Introduction**

Above mentioned, the hybrid type Li-air battery formed LiOH for discharge product, which was soluble in aqueous electrolyte [1,2]. However, the Li-air batteries with hybrid electrolyte had still some critical problems such as poor cycle performance, high overpotential and poor durability of cathode catalyst. These problems were occurred from low durability and low catalyst reaction kinetics. Although many catalyst materials were investigated to solve those problems such as perovskite structure materials, spinel structure materials and transition materials, these catalysts also have not enough performance for solution of that [3,4]. Thus, optimization of the air electrode was still needed to improve the cell performance.

Graphene nano sheets (GNSs) have been reported as a good candidate for cathode catalyst in the Li-air batteries, because of high surface area, high conductivity and low cost [5-9]. Our group had already proposed that the GNSs had high discharge potential and good cycle performance (50<sup>th</sup> cycles) in Li-air batteries with alkaline condition [2]. However, GNSs only electrode in Li-air batteries with hybrid electrolyte still showed high overpotential in discharge and charge process. Thus, it was necessary to find the efficient and stable cathode catalyst alternatives to Pt and metal oxide supported carbon which used commonly cathode catalyst in Li-air batteries with aqueous electrolyte [3,10-13].

Okada et al. reported that the electrocatalyst using organic metal complexes (mqph: N,N'-mono-8quinolyl-o-phenylenediamine) showed good electrochemical performance in polymer electrolyte fuel cell (PEFCs) and methanol oxidation reaction (MOR) [14-17]. Especially, they reported that Co(mqph) supported valcan XC-72R

showed good oxygen reduction reaction (ORR). However, the electrochemical performance of Co(mqph) combined carbon in Li-air batteries with aqueous electrolyte have not been reported so far. Here,  $M(\text{mqph})$  is featured as central metal-N coordination structure and peripheral aromatic rings [14-17]. The chemical structure of Co(mqph) was shown in Figure 2-1.

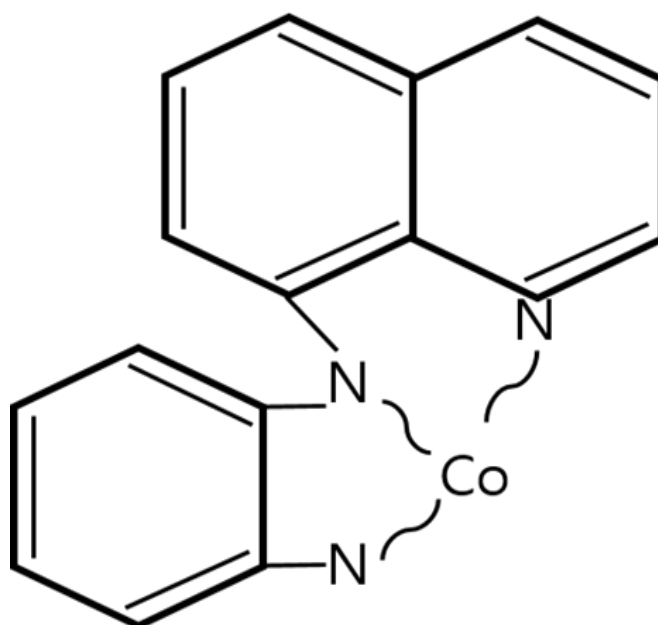


Figure 2-1. Schematics of Co(mqph).

In this study, we reported the heat treatment effect for carbon properties improvement to remove oxygen contained functional groups on RGO surface. Furthermore, electrochemical performance of the reduced graphene oxide (RGO) combined with Co(mqph) was also reported, which was proposed as a new-type catalyst for Li-air batteries with hybrid electrolyte under alkaline condition.

## 2.2 Experimental

### 2.2.1 Preparation of reduced graphene oxide (RGO).

Graphene Oxide (GO) was prepared by Hummers and Offeman's method, which was as follows: Graphite of 10 g was dispersed in 95 %  $\text{H}_2\text{SO}_4$  of 230 mL, and then  $\text{KMnO}_4$

of 30 g and  $\text{NaNO}_3$  of 5 g were slowly put in that solution [18]. The mixture was stirred for overnight at 50 °C. Then, 30 %  $\text{H}_2\text{O}_2$  of 30 mL was gradually added into the suspension. Obtained suspension were filtered and rinsed by the 35 % HCl to remove metal ions, the powder was washed with deionized water until its pH value reached to neuter. GO was reduced by 2 step reduction procedure to obtain the reduced graphene oxide (RGO). Firstly, GO was reduced by stirring with hydrazine hydrate for 12 hr at room temperature, washed with distilled water and then dried at room temperature. Secondly, dried powder was heated in 4 %  $\text{H}_2/\text{Ar}$  gas atmosphere for overnight at 300 °C.

### **2.2.2 Preparation of organic metal complexed catalyst (Co(mqph)).**

The metal organic complexed (Co(mqph)) was prepared by previous report of T. Okada et.al. The aqueous mixture of 8-hydroxyquinoline (0.02 mol) of 2.90 g, sodium disulfate (0.02 mol) of 3.08g and O-phenylenediamine (0.01 mol) of 1.08 g was refluxed for a week at 110 °C, which solution has recrystallization step in methanol. From the recrystallization, mono-8-quinolyl-o-phenylenediamine (mqph) has formation, which has amber colored cubic. The organic ligand (mqph) and acetate tetrahydrate were added at room temperature in ethanol under nitrogen atmosphere condition. The solution was concentrated and refrigerated to get cobalt mono-8-quinolyl-o-phenylenediamine (Co(mqph)). The Co(mqph) powder has a claret or reddish pupple color. The synthesized steps were showed as Figure 2-2.

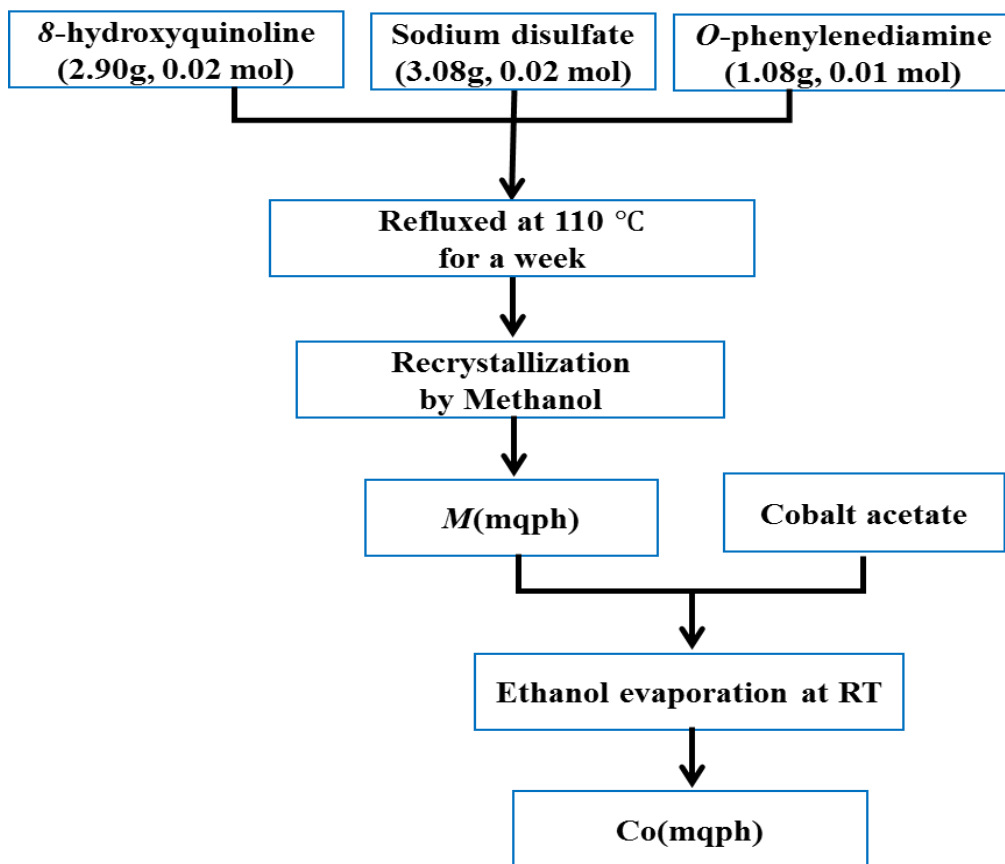


Figure 2-2. The diagram for preparation of organic metal complexed catalyst ( $\text{Co(mqph)}$ ).

### 2.2.3 Preparation of reduced graphene oxide with organic metal complexed (RGO- $\text{Co(mqph)}$ ).

The figure 2-3 showed diagram for synthesized reduced graphene oxide with  $\text{Co(mqph)}$ . To obtain the RGO- $\text{Co(mqph)}$ , RGO and  $\text{Co(mqph)}$  with mass ratios of 2:1 were mixed by hand in ethanol solution for 30 min, it was heated in a furnace under Ar stream for 2 hr at 450 °C.

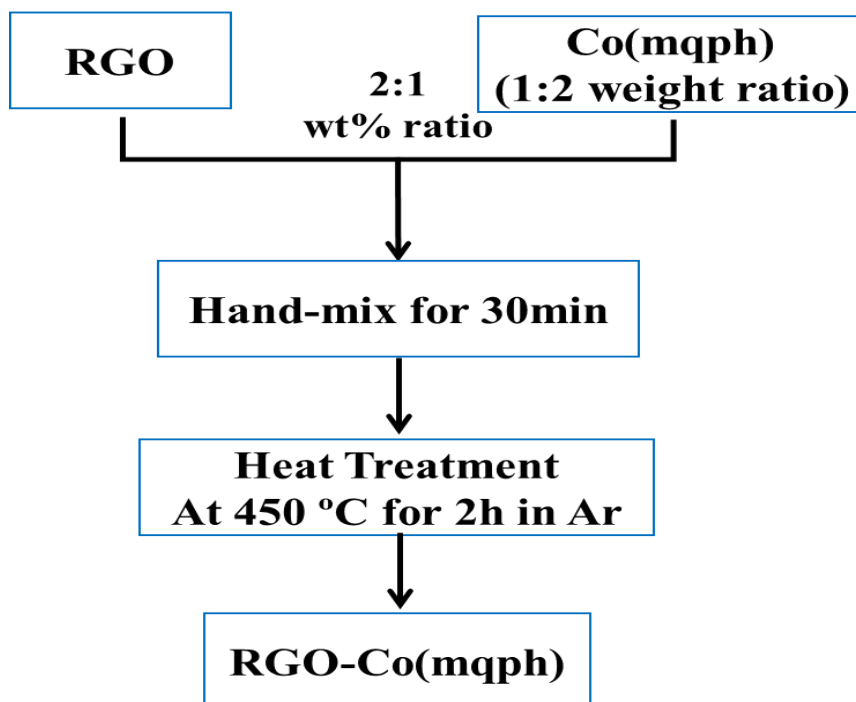


Figure 2-3. The diagram for synthesize reduce graphene oxide with Co(mqph).

#### 2.2.4 Fabrication of hybrid electrolyte Li-air battery and electrochemical test.

The electrochemical test set up for Li-air batteries with hybrid electrolyte was described in previous work of our group [2,19-21]. The schematics for hybrid electrolyte Li-air battery and the component ratio for cathode were shown as Figure 2-4. 1M LiOH was used aqueous electrolyte and 1M LiClO<sub>4</sub>/ EC/DEC was used organic electrolyte for anodic electrolyte and cathodic electrolyte, respectively. Then, the solid state electrolyte Li<sub>(1+x+y)</sub>Al<sub>x</sub>(Ti, Ge)<sub>2-x</sub>SiyP<sub>(3-y)</sub>O<sub>12</sub> (LiSICON) film was used as a separating membrane between the organic and aqueous electrolyte to prevent intermixing of both solutions.

The cathode was composed catalyst film and gas diffusion layer (GDL). The catalyst film consisted RGO-Co(mqph) (85 wt%), acetylene black (AB) (5 wt%) and 10 wt% polytetrafluoretrelyene (PTFE) (10 wt%). The AB gave to improve electric conductivity for electrode, however it was used minimum quantity to prevent alteration

of electrochemical property for catalyst material. The PTFE had a role for binder which also used minimum amount, because of its volume also has an effect to change electrochemical property. And GDL consisted acetylene black and PTFE, which component ratio was 1:1 weight ratio. Furthermore, the Ni mesh and Cu mesh was used collector for anode and cathode, respectively.

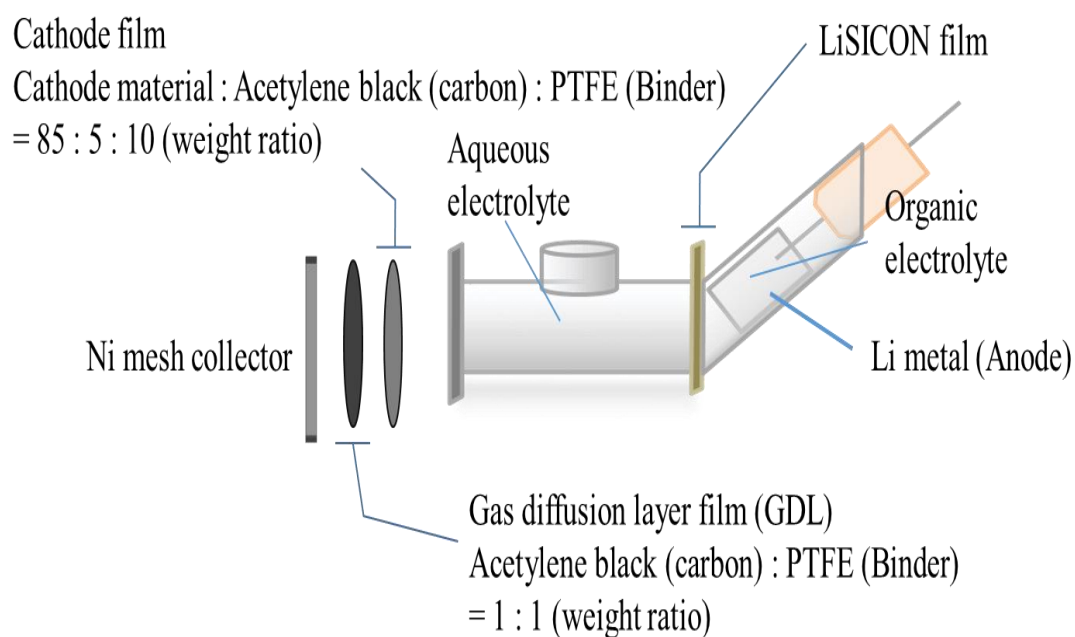


Figure 2-4. The schematics for hybrid electrolyte Li-air battery and the component ratio for cathode.

The oxygen reduction reaction (ORR) activity was tested by using rotating disk electrode (RDE) with room temperature under nitrogen and oxygen gas under alkaline electrolyte (1M LiOH). The figure 2-5 (a) showed RDE system, which consisted 3-electrode system. The counter electrode used a platinum and a silver/silver chloride electrode (Ag/AgCl) was used as the reference electrode. The figure 2-5 (b) showed schematics of cross section for working electrode on RDE system. The catalyst was loaded on glassy carbon electrode ( $0.285 \text{ cm}^2$ ) with diluted (1:50 in methanol) 5 wt% Nafion solution (Aldrich).

The ORR activity of catalyst was measured under pure  $\text{N}_2$  and  $\text{O}_2$  saturated condition. The pure  $\text{N}_2$  or  $\text{O}_2$  gases was fellow into alkaline solution through pipe of white color

over 30 min to exchange saturated gas condition. The gas was applying continuously during measurement of ORR activation for catalyst material.

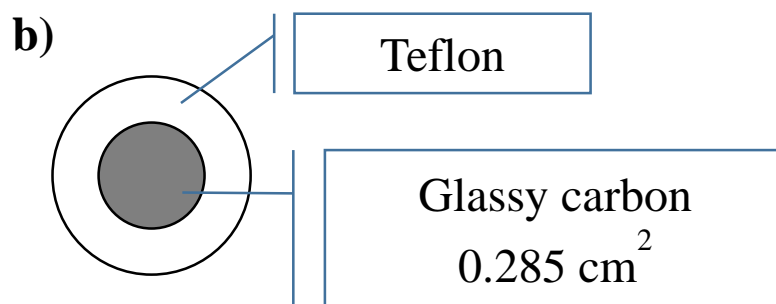
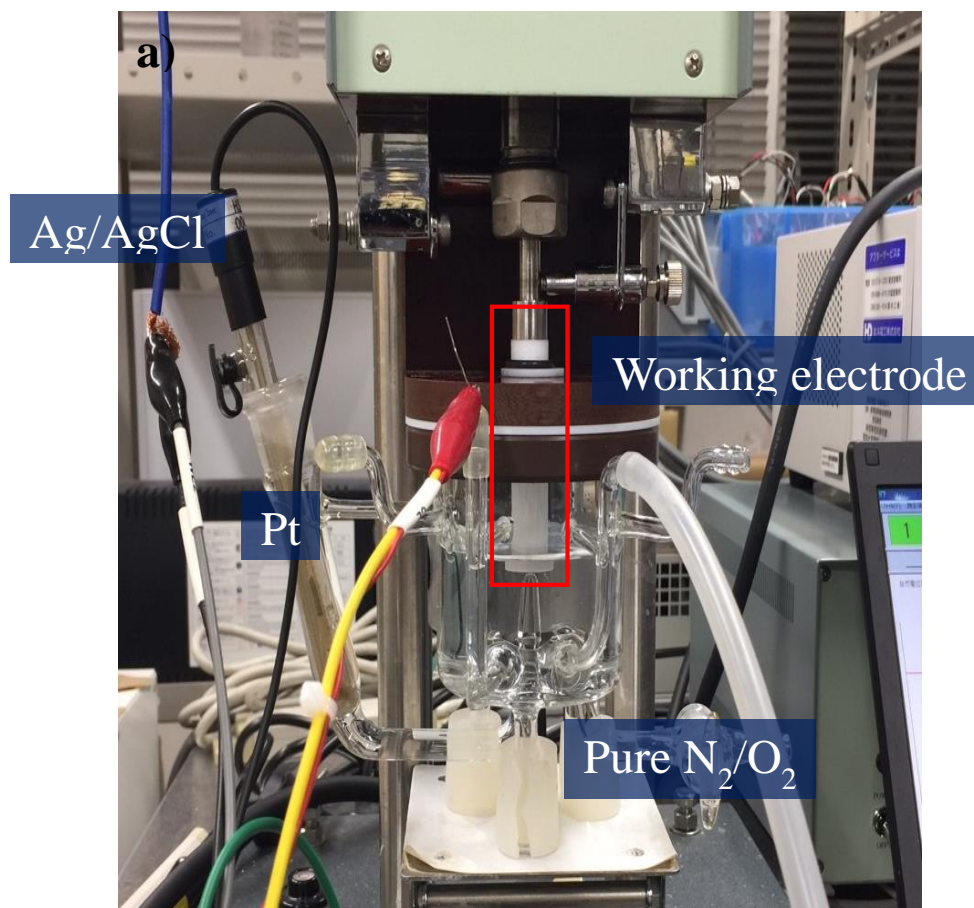


Figure 2-5. The image for rotating disk electrode (RDE) system (a) and schematics of cross section for working electrode (b), respectively.

## 2.2.5 Characterization

The RGO and RGO-Co(mqph) were characterized by X-ray diffraction (XRD), Thermogravimetry (TG), X-ray photoelectron spectroscopy (XPS), Raman spectroscopy, Scanning electron microscope (SEM), Transmission electron microscope (TEM), Energy dispersive X-ray spectroscopy (EDX) and Fourier Transform Infrared Spectroscopy (FTIR). A commercial 20 wt% Pt-CB was also used as a reference at the same condition.

## 2.3 Result and discussion

### 2.3.1 The characteristic changing and heat treatment effect for RGO

Figure 2-6 showed the XRD diffraction of RGO after discharge for 20 h, which material also prepared by Hummer's method and to be reduced by hydrazine solution.

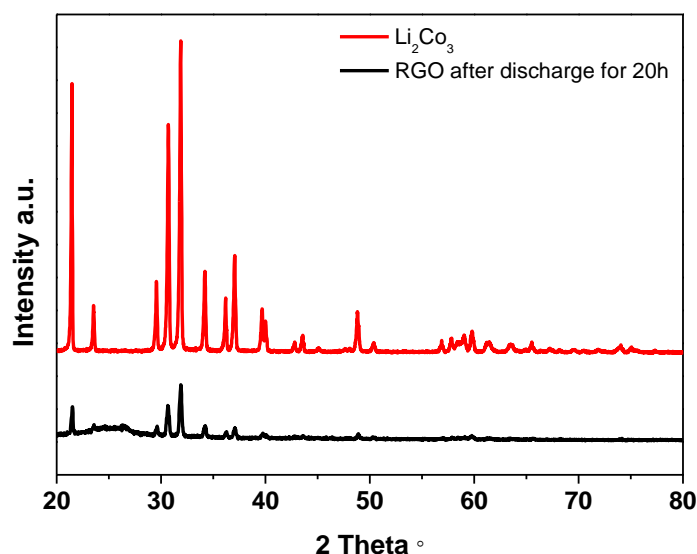


Figure 2-6. XRD pattern for  $\text{Li}_2\text{CO}_3$  and RGO after discharge for 20 h.

The XRD result showed that the RGO contained other XRD peaks after discharge for 20 h, which was corresponded with  $\text{LiCO}_3$ . This result indicated that the  $\text{Li}_2\text{CO}_3$  was formed during discharge performance. Thus, it was considered that the oxygen

contained functional groups of RGO surface involved to form  $\text{Li}_2\text{CO}_3$ . Therefore, we suggested the removal of oxygen contained functional group to improve discharge-charge performance in Li-air battery under hybrid electrolyte. Because of  $\text{Li}_2\text{CO}_3$  needed high potential for decomposition during charging, which also damaged carbon material. Thus, formation of  $\text{Li}_2\text{CO}_3$  was related with carbon corrosion during discharge-charge performance.

In general, RGO was reduced by reduction chemical such as mono-hydrazine hydrate solution. Nevertheless, the RGO still showed remaining oxygen contained functional groups. Thus, oxygen contained functional group was not removed by chemical reduction. Therefore, RGO was prepared through 2-step reduction procedure to remove oxygen contained functional groups. This chapter showed to change of carbon properties after heat treatment by XRD, TG-DTA and FTIR. The hydrazine reduction RGO was denoted 1-step RGO. Furthermore, the heat treatment reduction RGO was denoted 2-step RGO. The figure 2-7 showed XRD of 1-step RGO and 2-step RGO.

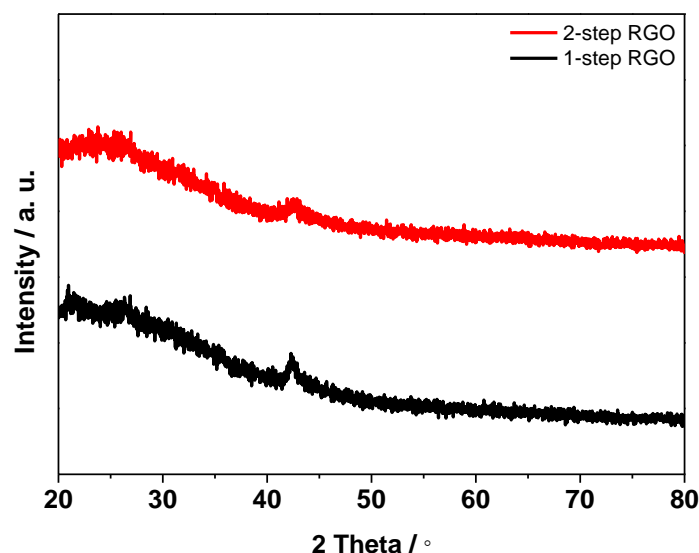


Figure 2-7. The comparison of XRD pattern for 1-step RGO and 2-step RGO.

Both RGO showed X-ray diffraction pattern at 23.4 and 42.5 °, and no more diffraction pattern was detected by XRD (Figure 2-7). Furthermore, the XRD pattern of both

materials showed broaden and similar intensity. This result indicated that both materials were consisted only carbon material. In addition, the graphitization of them also was similar.

The TG-DTA curve of 1-step RGO and 2-step RGO were shown in Figure 2-8 (a) and (b), respectively. The TG-DTA curve of 1-step RGO exhibited that the mass loss occurred couple times at 210 and 581 °C, respectively. In the first section, from room temperature to 210 °C, near 45 wt% of mass loss was obtained. On the other hands, 55 wt% of remaining carbon material have decomposed in second section. In my opinions, in the initial part, few remaining water was decompose under 100 °C. Furthermore, the hydroxyl functional group (-OH) species was decompose from 100 °C to 210 °C, section. On the other hands, the DTA curve of 2-step RGO showed that the mass loss occurred only one time at 645 °C. Moreover, the functional group of 2-step RGO was decreased after heat treatment.

This result indicated that the heat treatment has an effect for two things. First, it removed oxygen contained functional groups. Second, it was improved graphitization for RGO.

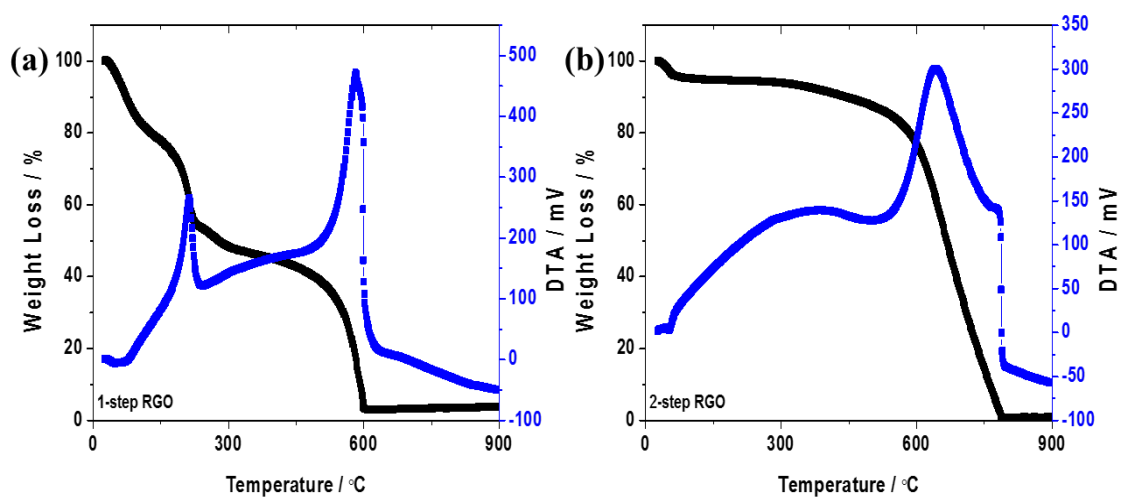


Figure 2-8. The TG-DTA for 1-step RGO (a) and 2-step RGO (b), respectively. The temperature increased from room temperature to 900 °C.

Furthermore, the FTIR analysis also showed that alteration of functional group after heat treatment. Many kind of functional group were located on 1-step RGO surface such as C-O, O-H, C=C and C-H stretching, which applied defect site on carbon surface. After heat treatment some kind of functional groups still remained on carbon surface. However, few kind of functional group reduced on the surface of 2-step RGO after heat treatment. Those were alkoxy (C-O), epoxy (C-O), carboxyle (C=C) and O-H of water at 1026, 1202, 1634 and 1385  $\text{cm}^{-1}$ , respectively. Reduced functional groups were contained oxygen and water molecules, thus oxygen contained functional groups was combined with hydrogen gas. Finally, the combined oxygen contained functional groups was removed by heat. These result indicated that almost oxygen contained functional groups were removed during heat treatment, nevertheless it was not removed perfectly. These consequences agreed with TG-DTA result, which were shown as Figure 2-9.

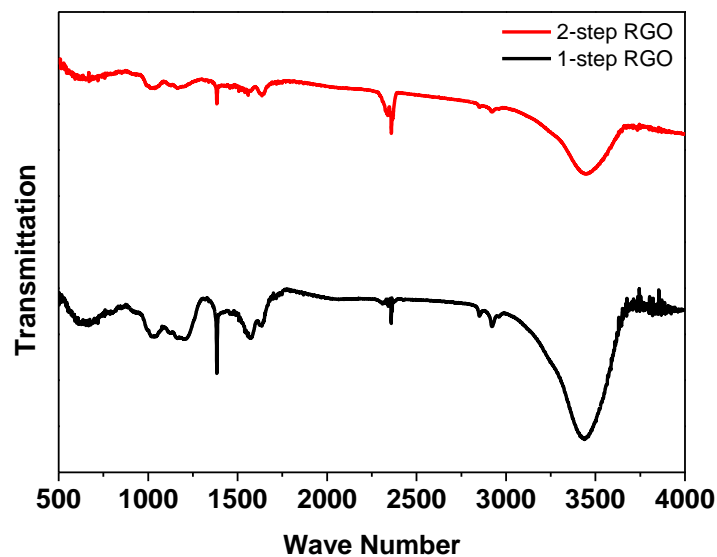


Figure 2-9. The comparison of FTIR for 1-step RGO and 2-step RGO.

The figure 2-10 showed cyclic performance at a current density of  $0.5 \text{ mA/cm}^2$  for 2 hr to each discharge-charge under hybrid electrolyte conditions for 1-step RGO and 2-step RGO, respectively. The 1-step RGO showed potential at 2.7 V for first discharging, which decreased to 2.5 V for 10<sup>th</sup> cycle gradually. Furthermore, the discharge potential reached under 2.5 V from 25<sup>th</sup> cycle. The charge potential of 1-step RGO was obtained

3.7 V at first cycle, which was suddenly increased to 4.1 V at 10<sup>th</sup> cycle. And then it showed stable charging potential until 25<sup>th</sup> cycle. The 1-step RGO worked during 25<sup>th</sup> cycles.

In contrast, 2-step RGO showed 2.8 V and 3.8 V for discharge potential and charge potential, respectively. The 2-step RGO also showed performance fading during discharge-charge procedure. The discharge potential of 2-step RGO was decreased gradually to 2.51 V during 37 cycles, furthermore the charge potential also increased gradually to 4.0 V for 37 cycles. Thus, 2-step RGO showed longer cycle performance, lower potential fading and lower overpotential gap than that of 1-step RGO. Thus, 2-step RGO showed high stability for cycle performance under hybrid electrolyte Li-air battery condition.

This result related with removal functional group on the carbon surface. Yoo et. al. demonstrated that oxygen contained functional group of carbon surface had an negative effect for cycle performance under alkaline electrolyte Li-air battery. They compared electrochemical performance of commercial GNs (graphene nano sheets) with heat treated GNs under alkaline electrolyte condition. The heat treated GNs showed better electro catalytic activity for ORR than commercial GNs. Furthermore, heat treated GNs showed higher stability for cycle performance than that of pristine GNs. The overpotential gap of bare GNs showed to be increasing during cycle performance test. Even though overpotential gap of heat treated GNs showed also increasing, it was very stable comparison with pristine GNs. Furthermore, they reported that the reason of improvement electrochemical performance related with heat treatment effect. The oxygen contained functional group was removed during heat treatment, which lead to prevent increasing overpotential for charging [21]. In addition, the graphitization of GNs was improve for heat treatment, which related with the improvement of carbon durability. Thus, the improvement cycling performance of 2-step RGO has an effect for heat treatment, which improve carbon duration and electro catalytic activity. Therefore, the 2-step RGO was used for this research, which was denoted RGO.

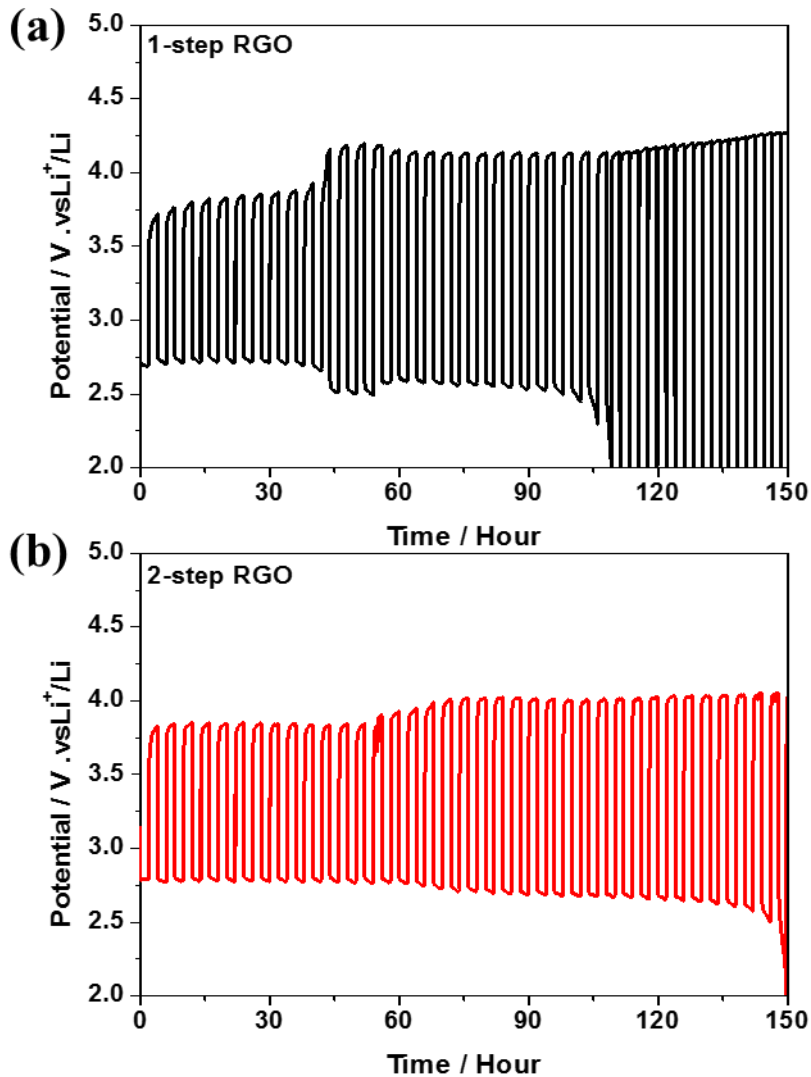


Figure 2-10. The cyclic performance at a current density of  $0.5 \text{ mA/cm}^2$  for 2 hr to each discharge-charge under hybrid electrolyte conditions for 1-step RGO (a) and 2-step RGO (b), respectively.

### 2.3.2 The characteristics for RGO with RGO-Co(mqph)

Figure 2-11 showed the XRD patterns of Co(mqph), RGO-Co(mqph) and RGO. The diffraction peak for Co(mqph), RGO-Co(mqph) and RGO was observed at  $22.8$ ,  $24.3$  and  $23.4^\circ$  of peak top, respectively. Furthermore, there were not observed the diffraction peaks of Co for Co(mqph) and RGO-Co(mqph). Thus, this result indicated

that the Co(mqph) did not decompose after heat treatment at 400 °C.

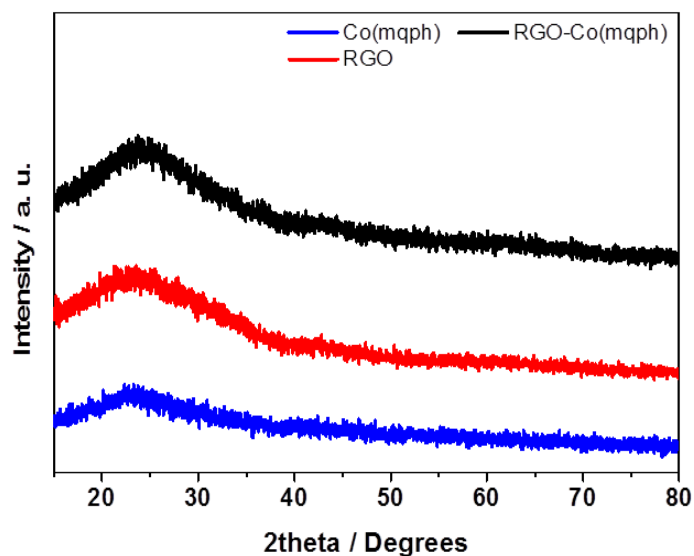


Figure 2-11. The XRD pattern for Co(mqph), RGO-Co(mqph) and RGO.

The SEM measurement were also carried out to observe the morphology of the RGO-Co(mqph) and RGO. The SEM images showed no significantly different morphology for both samples as shown in Figure 2-12 (a), (b). Furthermore, TEM images of RGO and RGO-Co(mqph) also showed same carbon morphologies as shown Figure 2-12 (c), (d). Especially, the Co metal particles were not detected on surface of RGO-Co(mqph). That also indicated that Co(mqph) was not decomposed during heat treatment procedure, which agreed with XRD result.

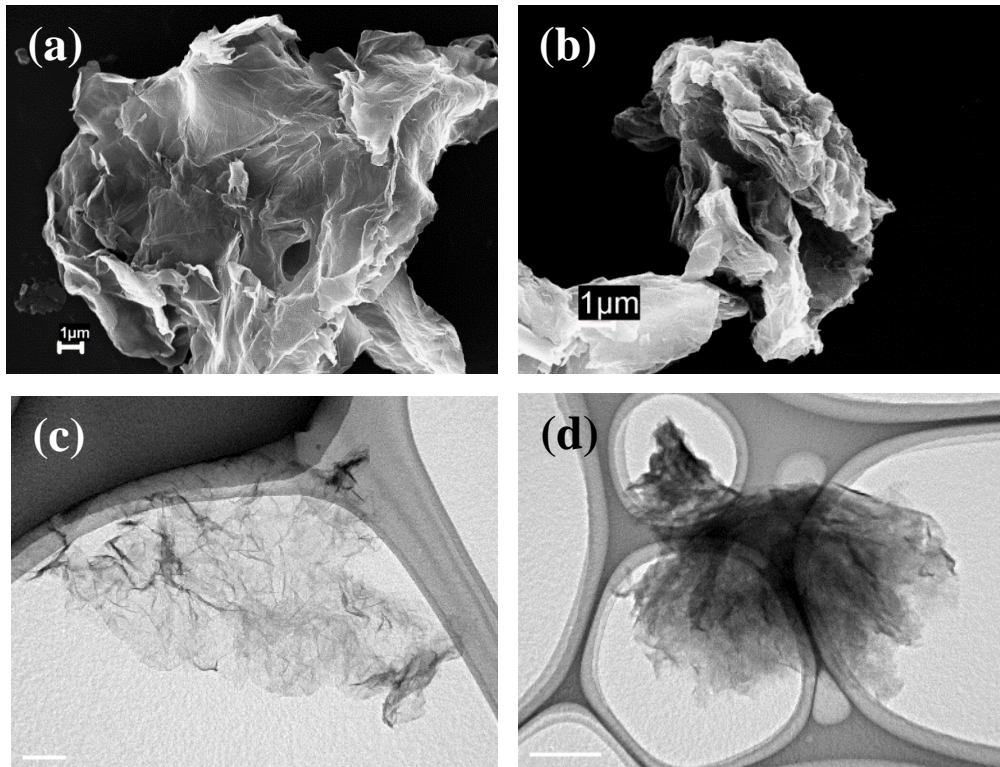


Figure 2-12. The SEM and TEM image of RGO (a),(c) and RGO-Co(mqph) (b),(d), respectively.

From the TEM image of RGO-Co(mqph) in Figure 2-12 (d), the EDX mapping was analyzed to confirm Co elements as shown in Figure 2-13. The EDX detected carbon, oxygen and Co, which was mapping by red, green and yellow color for carbon, oxygen and Co, respectively. The EDX mapping showed that the Co was not aggregated, thus it was dispersed on RGO surface very uniformly.

Furthermore, the X-ray Photoelectron Spectroscopy (XPS) analysis result also showed the Co element was contained on RGO-Co(mqph) composite. The XPS detected peak for C1s, N1s and O1s for RGO at 285.1, 399 and 533 eV, respectively. In contrast, RGO-Co(mqph) showed C1s, N1s and O1s, moreover Co2p<sub>3</sub> and Co2LM<sub>2</sub> also was detected at 716 and 782 eV, respectively. This result also indicated that the Co was contained in RGO-Co(mqph) composite as shown in Figure 2-14.

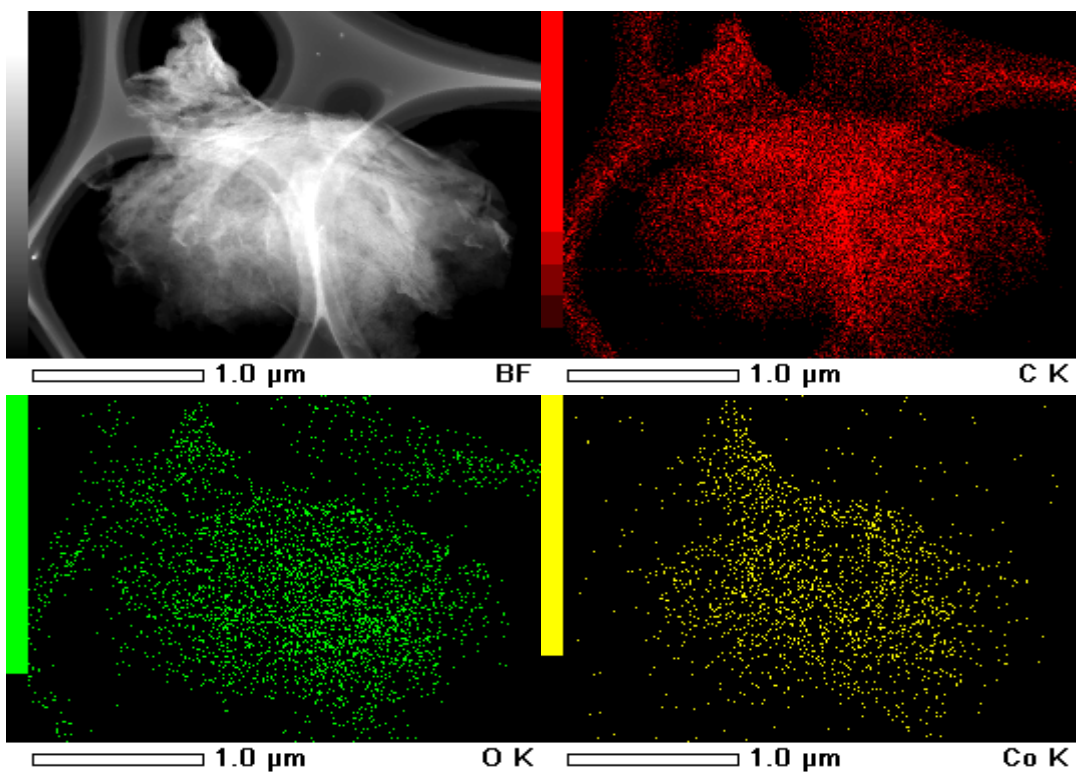


Figure 2-13. The XDX mapping of RGO-Co(mqph) from TEM image.

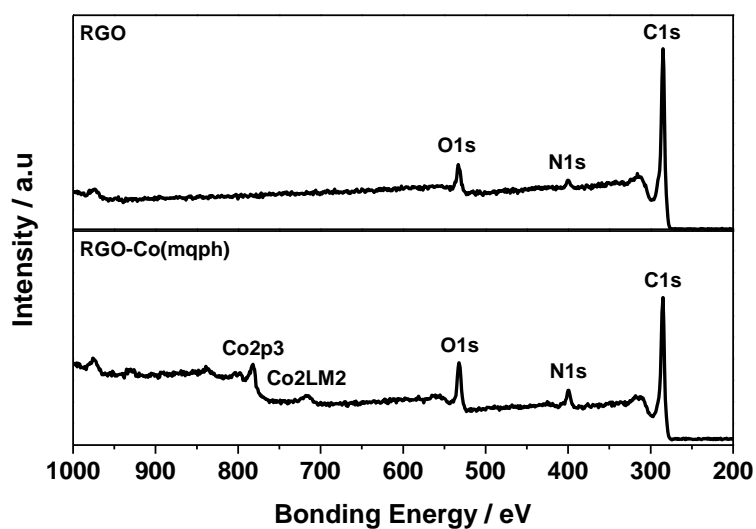


Figure 2-14. The XPS (X-ray Photoelectron Spectroscopy) analysis for RGO and RGO-Co(mqph) composite.

However, TG data obtained that RGO exhibited the mass loss of 15 % in the temperature range of room temperature to 600 °C, which resulted the removal of functional groups on RGO. Moreover, the TG curve of Co(mqph) showed the mass loss of 70 % at about 370 °C. It indicated that Co(mqph) contained 30wt% Cobalt metals. While the RGO-Co(mqph) started combusting at about 300 °C, the mass of RGO-Co(mqph) was lost about 90 % in the temperature range from 300 to 750 °C. Thus, this results clearly indicated that the Co(mqph) was mixed with RGO, which shown in Figure 2-15.

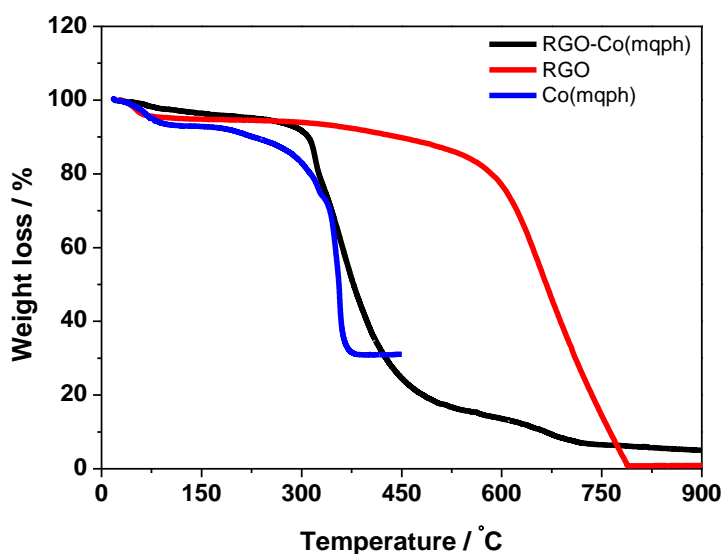


Figure 2-15. The thermal gravimetric analysis for Co(mqph), RGO and RGO-Co(mqph) composite, respectively.

### 2.3.3 Electrochemical performance for RGO-Co(mqph)

The cycle voltammetry (CV) of RGO, RGO-Co(mqph) and 20 wt% Pt-CB to examine the onset potential of ORR were shown in Figure 2-16. The onset potential of ORR for the RGO, RGO-Co(mqph) and 20 wt% Pt-CB at scan rate of 20 mV/s with rotating rate of 500 rpm in nitrogen and pure oxygen condition were at -0.13, -0.089 and -0.033 V vs. Ag/AgCl. Furthermore, the current density at -0.3 V vs. Ag/AgCl was -0.25, -0.8 and -1.97 mA/cm<sup>2</sup> for RGO, RGO-Co(mqph) and 20 wt% Pt-CB, respectively. The RGO-Co(mqph) showed the high onset potential of ORR and high value of current density at -0.3 V vs. Ag/AgCl comparison with RGO, indicating that the Co(mqph)

combined with RGO led to improve the catalytic activity toward oxygen reduction, even though the catalytic activity of ORR was lower than that of 20 wt% Pt-CB.

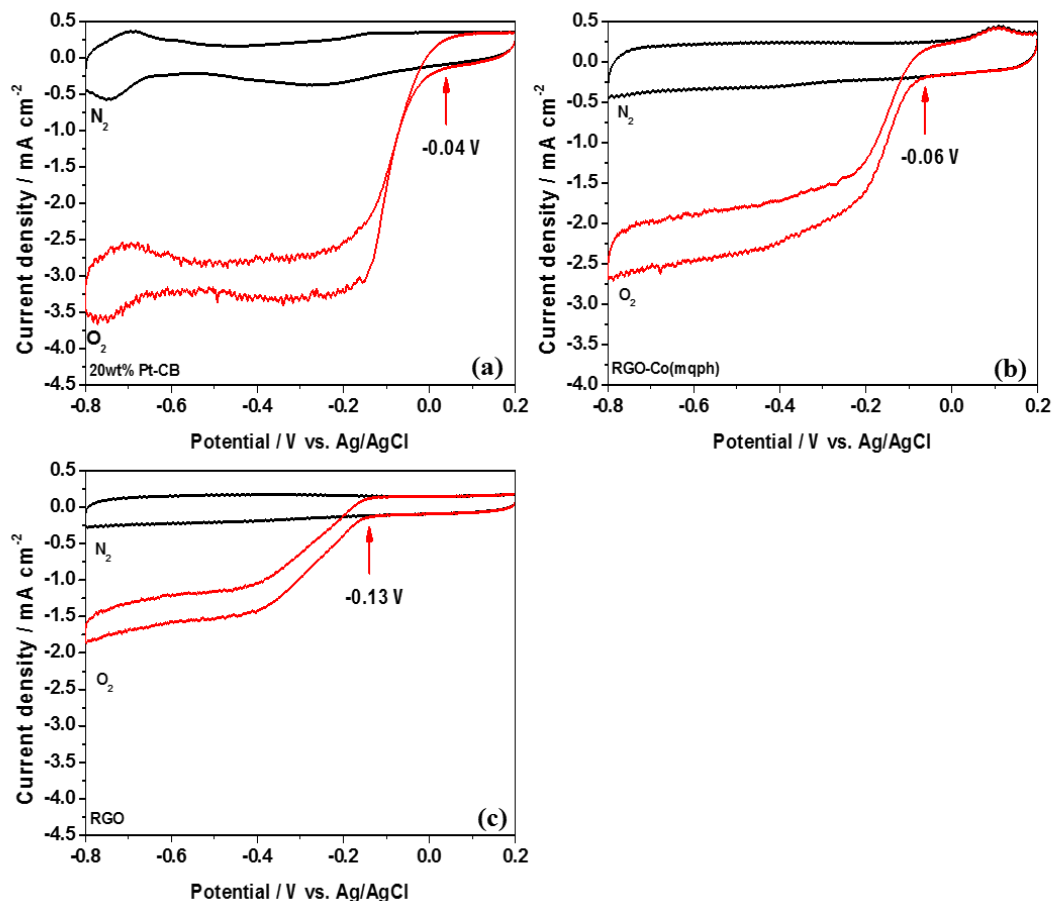


Figure 2-16. The cycle voltammetry (CV) for 20wt% Pt-CB (a), RGO-Co(mqph) (b) and RGO (c), respectively at 20mV/s, 500 rpm, under 1M LiOH solution in pure N<sub>2</sub> and O<sub>2</sub> saturated condition.

Figure 2-17 showed linear sweep voltammetry (LSV) curves for RGO, RGO-Co(mqph) and 20 wt% Pt-CB at scan rate of 20 mV/s with different rotating rates from 500 to 1500 rpm in oxygen condition to investigate the number of electrons ( $n$ ) involved in the ORR. As expected, the polarization curves of 20 wt% Pt-CB displayed current plateaus in the high polarization range. Furthermore, the mass transport limiting ORR voltage was reached at about -0.4 V and -0.5 V, for 20 wt% Pt-CB and RGO-Co(mqph), respectively.

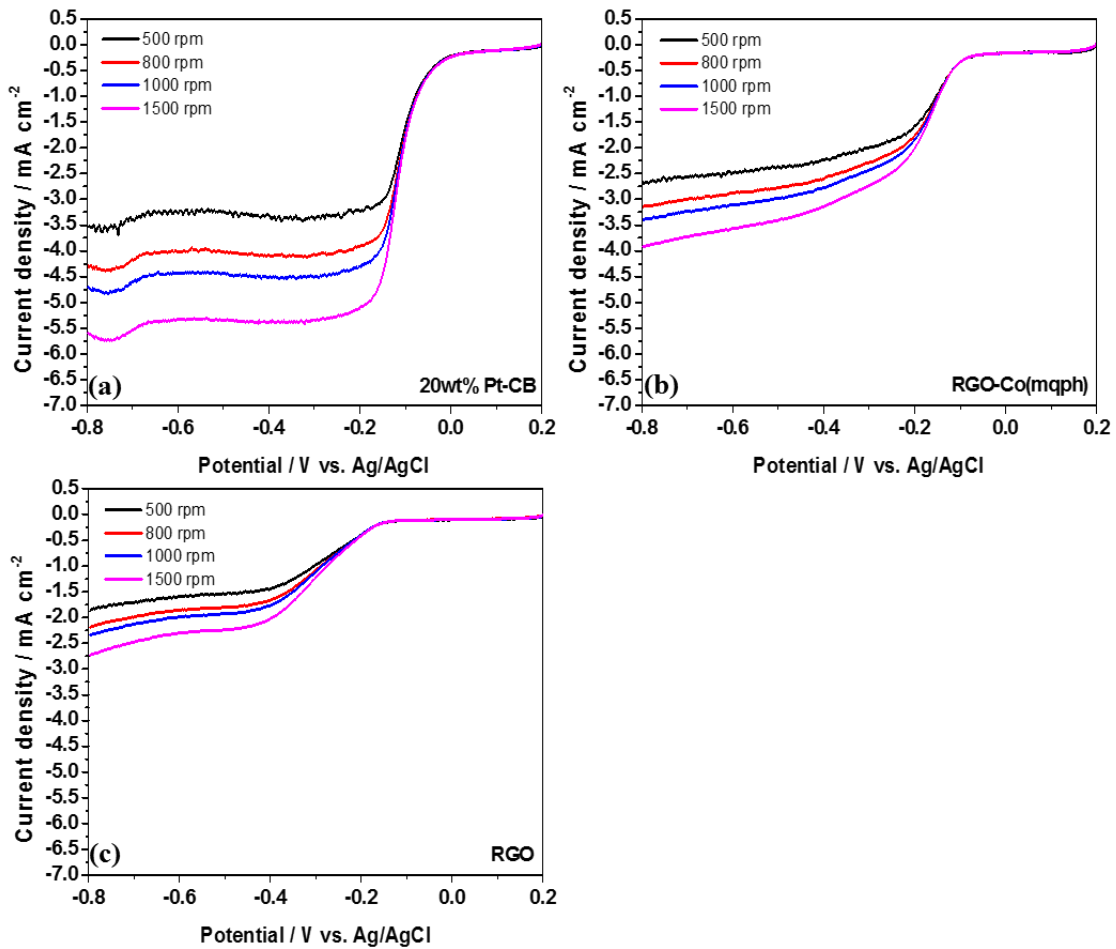


Figure 2-17. The linear sweep voltammetry (LSV) for 20wt% Pt-CB (a), RGO-Co(mqph) (b) and RGO (c), respectively at 20mV/s, 500-1500 rpm, under 1M LiOH solution in pure O<sub>2</sub> saturated condition.

While, the RGO did not reach the mass transport limiting ORR voltage, indicating a 2-electron transferred for the H<sub>2</sub>O<sub>2</sub> production [22]. The number of electrons involved in the ORR was estimated by using Koutechky-Levich (K-L) plots. The K-L equation was

$$\frac{1}{i} = \frac{1}{i_k} + \frac{1}{i_{l,c}}$$

$$i_{l,c} = 0.62nFAD_0^{2/3}w^{1/2}v^{-1/6}C_0^*$$

where,  $i_{l,c}$  is the limiting current,  $n$  the number of electrons transferred in the half reaction,  $F$  the Faraday constant,  $A$  the electrode area,  $D_0$  the diffusion coefficient,  $\omega$  the angular rotation rate of the electrode,  $\nu$  the kinematic viscosity, and  $C_0^*$  analyze concentration. The K-L plots determined from LSV data in Figure 2-18. In this study, the number of electron transfer for 20 wt% Pt-CB were assumed to be 4-electron, because it was well known that the ORR by Pt-CB proceeds via 4-electron pathway in an acidic or alkaline media [23-29].

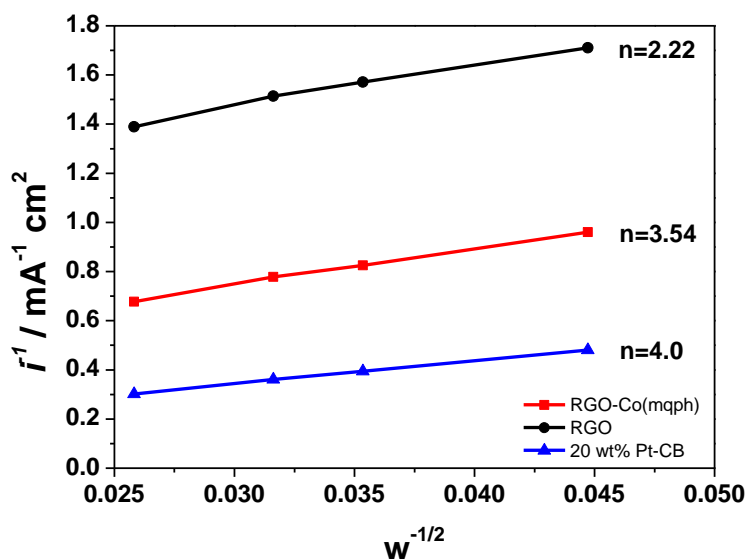


Figure 2-18. The K-L plots determined from LSV data at -0.5 V for 20wt% Pt-CB, RGO-Co(mqph) and RGO, respectively.

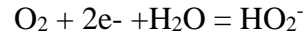
Based on the slopes of the K-L plots, the electron transfer number was calculated to be 2.22, 3.52 and 4 for RGO, RGO-Co(mqph) and 20 wt% Pt-CB, respectively. These results suggested that ORR catalyzed on RGO-Co(mqph) was a close 4-electron reduction process leading to the formation of  $H_2O$ . It was thus indicated that the Co(mqph) played an important role in the ORR catalyst, because only RGO electrode was more less than 4-electron reaction.

Figure 2-19 was diagram for ORR mechanism under alkaline electrolyte. Many research groups studied for reaction mechanism of oxygen reduction under aqueous solutions. As a result, it was demonstrated that the oxygen reacted with 4-electron and 2-electron under aqueous solution. Furthermore, Li-air battery under aqueous

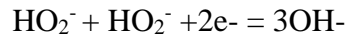
electrolyte has same mechanism. The 4-electron path way reaction was,



On the other hands, the 2-electron path way reaction was,



The  $\text{HO}_2^-$  was reacted consecutively,



Or  $\text{HO}_2^-$  had chemical reaction with  $\text{HO}_2^-$ ,



The LiOH was formation to combined  $\text{OH}^-$  with  $\text{Li}^+$  by 4-electron path way reaction in Li-air battery under hybrid electrolyte.

Thus, the RGO-Co(mqph) had 4-electron path way and it make soluble discharge product of LiOH during discharging. On the other hands, the RGO produced hydro peroxide ( $\text{H}_2\text{O}_2$ ) for discharge product. Both reaction shown in the Figure 2-19.

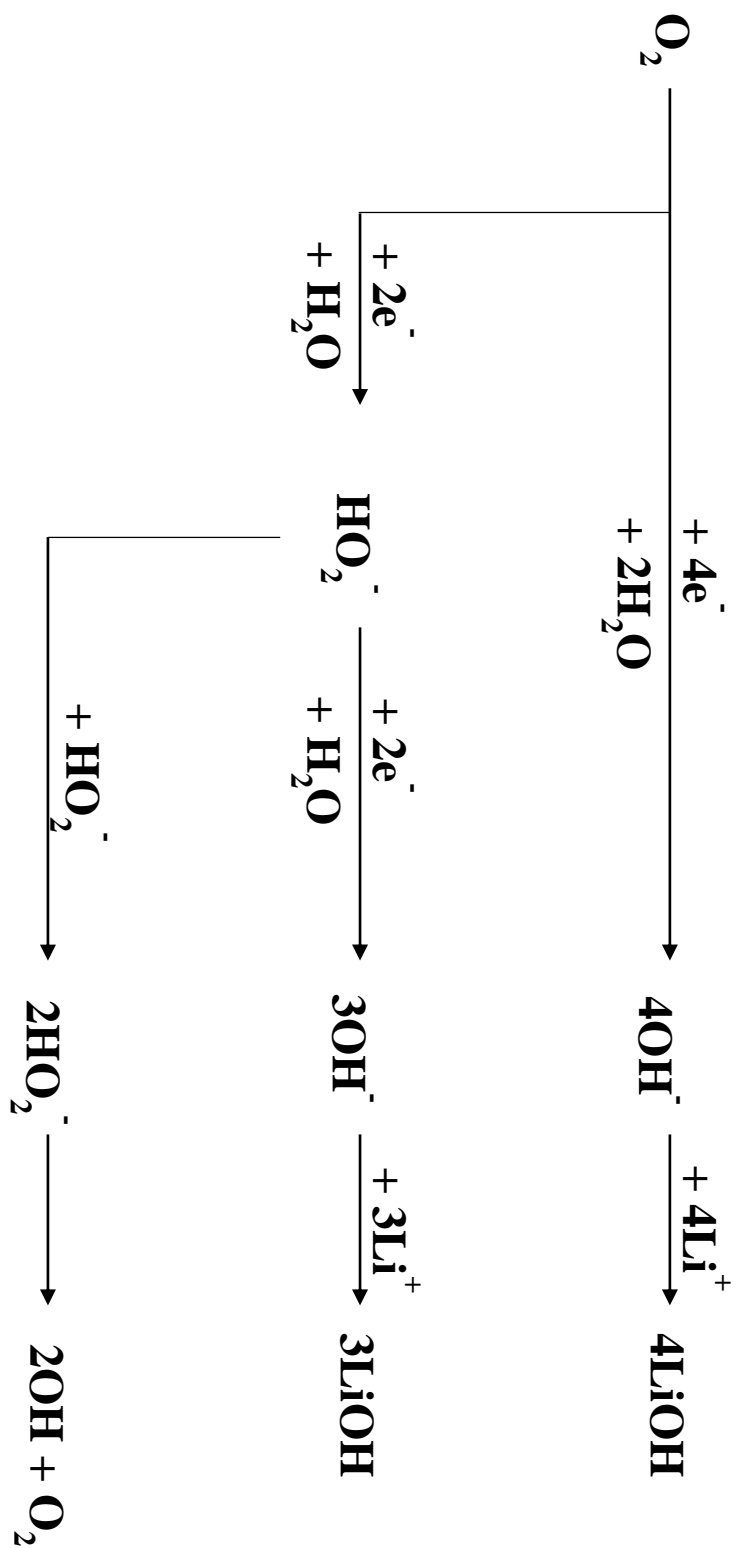


Figure 2-19. The diagram for ORR mechanism with 4-electron and 2-electron under alkaline electrolyte.

Figure 2-20 gave the discharge curves of RGO, RGO-Co(mqph) and 20 wt% Pt-CB at a current density of 0.5 mA/cm<sup>2</sup> for 24 hr. The discharge voltage was 2.81, 2.87 and 2.97 V vs. Li/Li<sup>+</sup> for RGO, RGO-Co(mqph) and 20 t% Pt-CB, respectively. The discharge voltage of RGO-Co(mqph) exhibited higher than that of RGO. In other word, discharge overpotential was 0.61, 0.55 and 0.45 V for RGO, RGO-Co(mqph) and 20 t% Pt-CB, respectively. Thus, RGO-Co(mqph) showed smaller discharge overpotential than that of RGO. These difference of discharge properties between RGO-Co(mqph) and RGO were attributed to add the Co(mqph) on RGO, which indicated that the reason of higher electro catalytic activity of RGO-Co(mqph) for ORR under alkaline electrolyte was high electro catalytic ability of Co(mqph). Therefore, it can be considered that the RGO-Co(mqph) was the promising catalyst for Li-air batteries in aqueous media.

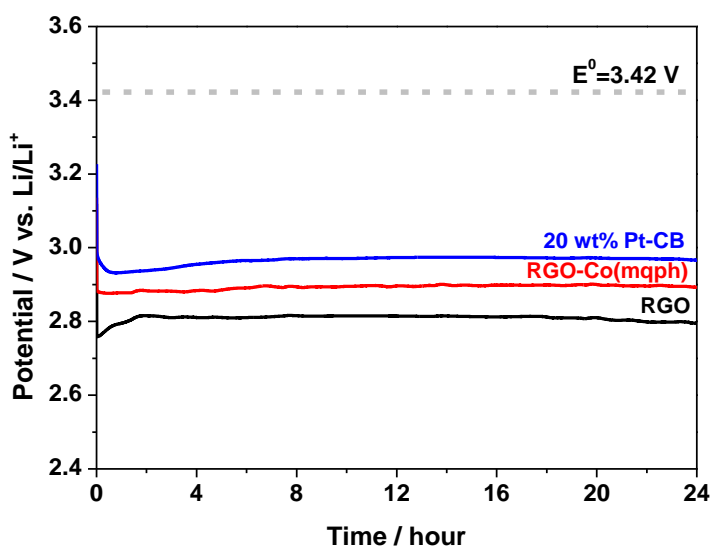


Figure 2-20. The discharge performance for RGO, RGO-Co(mqph) and 20wt% Pt-CB under 1M LiOH solution at 0.5 mA cm<sup>-1</sup> during 24 hours.

In order to investigate the stability of RGO-Co(mqph) for Li-air batteries with hybrid electrolyte, the Li-air cells with RGO, RGO-Co(mqph) and 20 wt% Pt-CB cathode were cycled at a current density of 0.5 mA/cm<sup>2</sup> for 2 hr to each discharge-charge at 30<sup>th</sup> cycles (Figure 2-21). At 1<sup>st</sup> cycles, the discharge voltage for RGO, RGO-Co(mqph) and 20 wt% Pt-CB were 2.88, 2.97 and 3.04 V vs. Li/Li<sup>+</sup>, respectively. Moreover, the charge voltage

at 1<sup>st</sup> cycles was 3.69, 3.74 and 3.80 V for RGO, RGO-Co(mqph) and 20 wt% Pt-CB. However, with discharge-charge cycling, the charge voltage of 20 wt% Pt-CB increased from about 3.80 to 4.3 V vs. Li/Li<sup>+</sup> after 30<sup>th</sup> cycles. The discharge voltage of 20 wt% Pt-CB also decreased from 3.04 to 2.0 V after 30<sup>th</sup> cycles. In contrast, for the RGO-Co(mqph), the charge voltage gradually increased, reaching the charge voltage of 3.87 V after 30<sup>th</sup> cycles. The discharge voltage also gradually decreased with each cycle, reaching at 2.74 V after the 30<sup>th</sup> cycles. Furthermore, for the RGO, the increased voltage value after 30<sup>th</sup> cycles was about 0.08 and 0.08 V for charge and discharge process, respectively. It indicated that the RGO and RGO-Co(mqph) revealed good cycle stability comparison with 20 wt% Pt-CB. Our group already reported that the surface state of GNSs influenced the cycle performance in Li-air batteries with alkaline media [5]. Therefore, the difference of cycle stability between RGO, RGO-Co(mqph) and 20 wt% Pt-CB may be attributed to different surface structure of RGO consisting of graphene sheets. Figure 2-22 showed the discharge and charge potential of whole measured samples for each cycle obtained from Figure 2-21 (a-c). Interestingly, we found that the charge potential of RGO was below 3.8 V vs. Li/Li<sup>+</sup> after 30<sup>th</sup> cycles. This value of RGO was lower by far than that of reported based on only carbon used as cathode in Li-air batteries under alkaline media (4.0 and 4.2 V vs. Li/Li<sup>+</sup>) [30,31]. In comparison, the RGO-Co(mqph) showed the charge potential of 3.87 V after 30<sup>th</sup> cycles. However, the difference discharge potential between the 1<sup>st</sup> cycles and 30<sup>th</sup> cycles was 0.08 and 0.23 V for RGO and RGO-Co(mqph), respectively. Although the reason of decreasing discharge potential of RGO-Co(mqph) than RGO with cycling was unclear, it considered that adding Co(mqph) on RGO might activate the oxidation of RGO with cycling. To investigate the surface state of RGO and RGO-Co(mqph), the XPS measurement was examined.

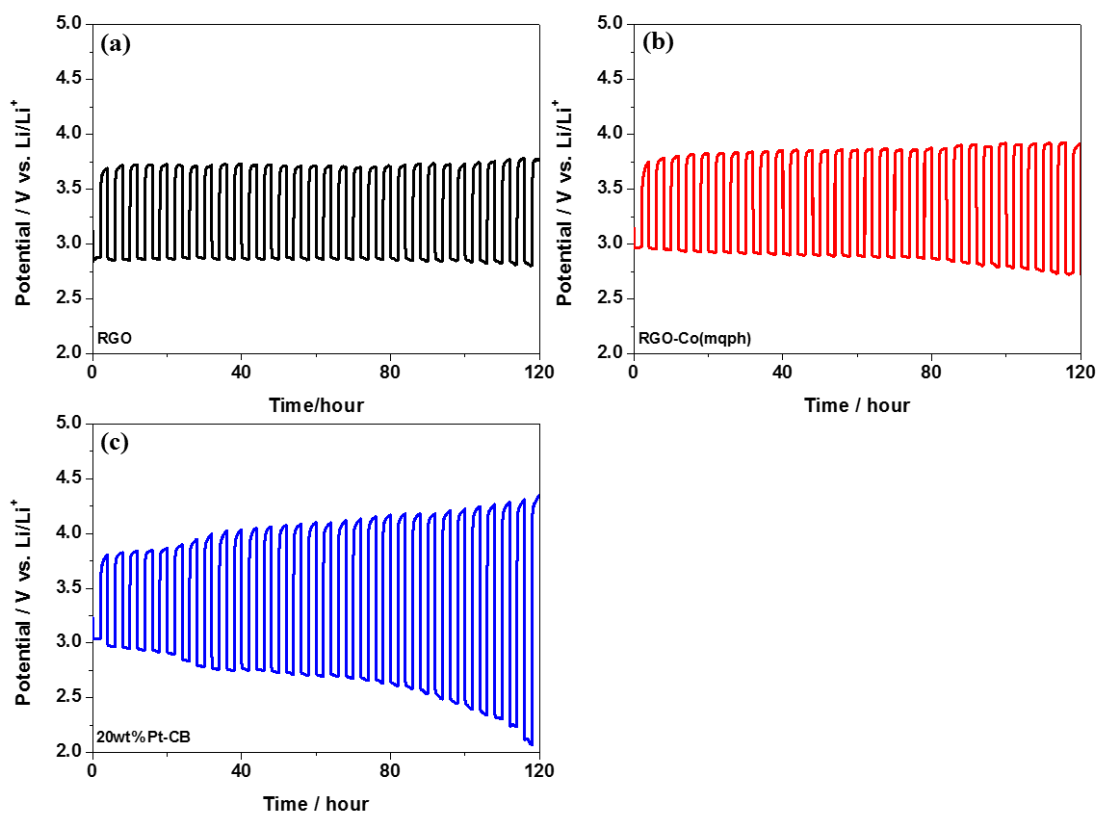


Figure 2-21. The cycle performance under 1M LiOH solution at  $0.5 \text{ mA cm}^{-1}$ , discharging and charging time each 2 h during 30 cycle for RGO (a), RGO-Co(mqph) (b) and 20wt% Pt-CB (c), respectively.

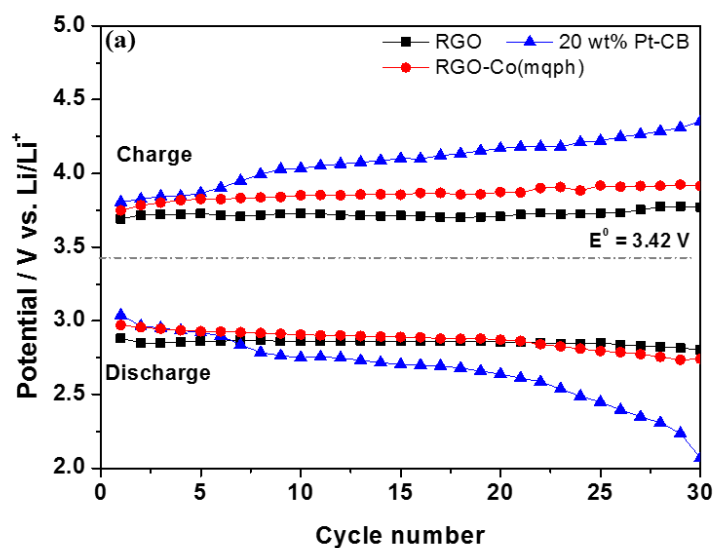


Figure 2-22. The discharge and charge potential of whole measured samples for each cycle for RGO, RGO-Co(mqph) and 20wt% Pt-CB, respectively.

Figure 2-23 showed XPS spectra of  $C_{1s}$  (a) and  $O_{1s}$  (b) for RGO and RGO-Co(mqph), respectively. The  $C_{1s}$  XPS spectra showed the presence several components correspond to carbon atoms in various functional groups. We could find that the  $C_{1s}$  XPS spectra of RGO-Co(mqph) and RGO exhibited same functionalities.

To understand the dependence of defects and edges state on RGO and RGO-Co(mqph), the  $sp^3/sp^2$  hybridization ratio of the RGO and RGO-Co(mqph) was estimated by integrating the corresponding component against the binding energy for XPS peaks as shown Figure 2-24 (a). The  $sp^3/sp^2$  hybridization ratio for RGO and RGO-Co(mqph) were 12.8 and 6.16, respectively. The decrease of  $sp^3/sp^2$  ratio for RGO-Co(mqph) was mainly caused by an increase of  $sp^2$ -bonded carbon sites due to the formation of graphitized C–C bonds on heating. Thus, we considered that the RGO-Co(mqph) was graphitized by heating. The Raman measurement also was carried out confirm the crystallization of RGO and RGO-Co(mqph) as shown in Figure 2-24 (b). The Raman spectra of RGO and RGO-Co(mqph) showed the two distinct peaks corresponding to the D and G bands of carbon, respectively. It was also revealed that the intensity ratio of  $I_G/I_D$  was 0.46 and 0.50 for RGO and RGO-Co(mqph), indicating that the RGO-Co(mqph) was graphitized by heating. From XPS and Raman results, it was considered

that the high charge potential of RGO-Co(mqph) was ascribed to the flat surface structure of RGO by heat-treatment during RGO-Co(mqph) preparing process.

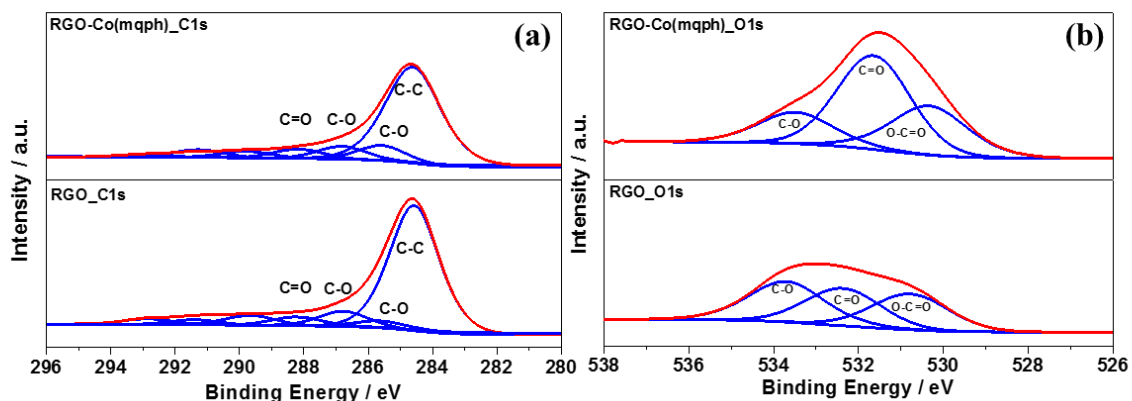


Figure 2-23. XPS spectra of C<sub>1s</sub> (a) and O<sub>1s</sub> (b) for RGO and RGO-Co(mqph), respectively.

X. Lu. et al. have reported that oxidized multiwall-carbon nanotubes (MWCNTs) showed good oxygen evolution reaction (OER) activity, due to the presence of oxygen-containing functional groups on the outer wall of MWCNTs. Oxygen-Containing functional groups such as ketonic C=O generated on the outer wall of MWCNTs were found to play crucial role in catalyzing OER by altering the electronic structures of the adjacent carbon atoms and facilitates the adsorption of OER intermediates [32].

That was, the presence of functional groups on carbon may be the crucial factor to improve the OER activity in Li-air batteries. Although the detail mechanism of low charge overpotential for RGO was unclear, it was considered that the low charge overpotential of RGO after 30<sup>th</sup> cycles was attributed to the presence of functional group on carbon surface. Thus, we expected that controlling oxygen-containing functional group and surface state of carbon materials enabled to reduce the charge overpotential and enhance the cycle stability for Li-air batteries.

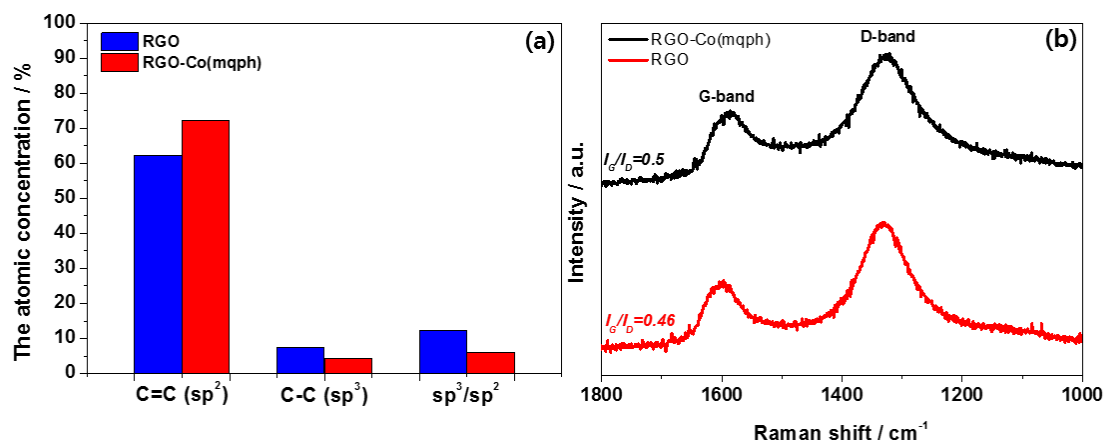


Figure 2-24. The  $sp^3/sp^2$  hybridization ratio of the RGO and RGO-Co(mqph) (a) was estimated by integrating the corresponding component against the binding energy for XPS peaks. And the Raman spectroscopy and  $I_G/I_D$  value for RGO and RGO-Co(mqph) (b).

## 2.4 Conclusion

We demonstrated that the ORR activity and cycle performance of Li-air batteries with hybrid electrolyte based on RGO and RGO-Co(mqph) used as a cathode electrode. The heat treated RGO has less oxygen contained functional group on carbon surface and higher graphitization than that of non-heat treated RGO. Therefore, heat treated RGO showed smaller overpotential gap for cycle performance, furthermore it also showed longer cycle performance in Li-air battery under hybrid electrolyte conditions. Because of various oxygen contained functional groups were removed as well as moreover carbon crystalline also improved during heat treatment. Therefore, heat treated RGO was used to combine with organic metal complexed catalyst (Co(mqph)). The RGO-Co(mqph) exhibited good ORR activity, which was obtained enhanced electron transfer number than RGO. It showed about 3.52 electron path was for oxygen reduction reaction. Furthermore, the RGO-Co(mqph) showed the good stability of cycle performance comparison with commercial 20 wt% Pt-CB. This result indicated that introducing Co(mqph) on RGO promoted the ORR activity and electrochemical performance of Li-air batteries in alkaline condition.

## 2.5 Reference

- [1] Z. Cui, L. Li, A. Manthiram and JB. Goodenough *J. Am. Chem. Soc* 137(23) (2015) 7278-7281
- [2] E. Yoo, H. Zhou *ACS Nano* 5 (2011) 3020-3026
- [3] T. Poux, F.S. Napolskiy, T. Dlutzer, G. Kerangueven, S. Ya. Istomin, G. A. Tsirlina, E. V. Antipov. E. R. Savinova *Catalysis Today* 189 (2012) 83-92
- [4] L. Wang, X. Zhao, Y. Lu, M. Xu, D. Zhang, R S. Ruoff, K J. Stevenson, J B. Goodenough *Journal of The Electrochemical Society* 158 (12) (2012) A1379-A1382
- [5] K. Niu, B. Yang, J. Cui, J. Jin, X. Fu, Q. Zhao *Journal of Power Source* 243 (2013) 65-71
- [6] S. Pei, H. M. Cheng *Carbon* 50 (2012) 3210-3228
- [7] N. Pan, D. Guan, Y. Yang, Z.Huang, B. Wang, Y. Jin *Chemical Engineering Journal* 236 (2014) 471-479
- [8] H. Huang, H. Chen, D. Sun, X. Wang *Journal of Power Source* 204 (2012) 46-52
- [9] V. Tjoa, J. Chua, S. S. Pramana, J. Wei, S. G. Mhaisakar, N. Mathews *ASC Appl. Mater. Interfaces* 4 (2012) 3447-3452
- [10] L. Wang, M. Ara, K. Wadumesthrige, S. Salley, K. Y. Simon Ng *Journal of Power Sources* 234 (2013) 8-15
- [11] H M. A. Amain, H. Baltruschat, D. Wittmaier, K.A Friedrich *Electrochimica Acta* 151 (2015) 332-339
- [12] D J. Davis, A-R O. Raji, T N. Lambert, J A. Vigil, L. Li, K. Nan, J M. Tour *Electroanalysis* 26 (2014) 164-170
- [13] Y. Wu, Q. Shi, Y. Li, Z. Lai, H. Yu, H. Wang, F. Peng *J. mater. Chem. A* 3 (2015) 1142
- [14] T. Okada, Y. Suzuki, T. Hirose, T. Ozawa *Electrochimica Acta* 49 (2004) 385-395

- [15] J. P. Oh, E. Yoo, C. Ono, T. Kizuka, T. Okada, J. Nakamura *Journal of Power Source* 185 (2008) 886-891
- [16] M. Saito, H. Shhiroishi, C. Ono, S. Tsuzuki, T. Okada, Y. Uchimoto *Journal of Molecular catalyst catalysis A : Chemical* 248 (2006) 99-108
- [17] T. Okada, N. Arimura, C. Ono, M. Yuasa *Electrochimica Acta* 51 (2005) 1130-1139
- [18] W. S. Hummers, Jr., R. E. Offeman *National Lead Company* (1958) 1339
- [19] P. He, Y. Wang, H. Zhou *Journal of Power Source* 196 (2011) 5611-5616
- [20] H. Zhou, Y. Wang, H. Li, P. He *ChemSusChem* 3 (2010) 1009-1019
- [21] E. Yoo, J. Nakamura, H. Zhou *Energy Environ. Sci.* 5 (2012) 6928
- [22] K. Lee, M. S. Ahmed, S. Jeon *Journal of The Electrochemical Society* 162 (2015) F1-F8
- [23] Y. Wang, R. Ohnishi, E. Yoo, P. He, J. Kubota, K. Domen, H. Zhou *J. Mater. Chem* 22 (2012) 15549-15555
- [24] E. Yeager *Journal of molecular catalysis*, 38 (1986) 5-25
- [25] B. Geboes, I. mintsouli, B. Wouters, J. Georgieva, A. Kakaroglou, S. Sotiropoulos, E. Valova, S. Armyanov, A. Hubin, T. Bregelmans *Applies Catalysis B : Environmental* 150-151 (2014) 249-256
- [26] J. Sunarso, A. A. J. Torriero, W. Zhou, P. C. Howlett, M. Fosyth *J. Phys. Chem. C* 116 (2012) 5827-5834
- [27] S. Lj. Gojkovic, S. Gupa, R. F. Savinell *Journal of Electroanalytical Chemistry* 462 (1999) 63-72
- [28] P. S. Ruvinskiy, A. Bonnefont, E. R. Savinova *Electrocatal* 2 (2011) 123-133
- [29] Y. Liu, Y. Y. Wu, G. J. LV, T. Pu, X. Q. He, L. L. Cui *Electrochimica Acta* 112 (2013) 269-278
- [30] J L. Shui, N K. Karan, M. balasubramanian, S Y. Li, D J. Lui *J. Am. Chem. Soc.*

134 (2012) 16654-16661

[31] Y. Li, Z. Huang, K. Huang, D. Carnahan and Y. Xing *Energy Environ. Sci.* 6 (2013) 3339-3345

[32] X. Lu, W. Leung, B. H. R. Suryanto, C. Zhao *J. Am. Chem. Soc.* 137 (2015) 2901-2907

# **Chapter 3. Investigation of grown carbon nanofiber on carbon black (CNF-CB) to improve cycle performance.**

## **3.1 Introduction**

The reduced graphene oxide with Co(mqph) composite (RGO-Co(mqph)) was attempted to use cathode material to improve electrochemical performance during battery cycle performance in previous chapter. Furthermore, our group also reported that the hybrid Li-air batteries based on graphene nanosheet, Mn<sub>2</sub>O<sub>3</sub> supported carbon for cathode. These displayed improved oxygen reduction reaction (ORR) activity during the discharge process and enhanced cycle stability [1,2]. Moreover, many research groups also attempted investigation of cathode material to use low-cost catalysts for example carbon materials or metal oxides M<sub>x</sub>O<sub>y</sub> (M=Ni, Cu, Mn, Co) [3-10]. However, the hybrid Li-air batteries were still in a developing to overcome the large discharge-charge overpotential gap and cycle stability. The carbon oxidation for discharge-charge performance was serious problems. To prevent carbon oxidation, reduced graphene oxide with Co(mqph) composite was tried for cathode. Nevertheless, that catalyst also showed carbon oxidation during cycle performance. Therefore, the investigation of metal-free catalyst was very important. Moreover, the cycle stability problem of hybrid Li-air batteries was related to the sluggish kinetics of ORR and poor durability of the cathode catalyst. Therefore, the development of an electrocatalyst with highly active and stable for the ORR and oxygen evolution reaction (OER) was one of the most attractive challenges in hybrid Li-air batteries.

Therefore, the nano structure carbon such as graphene and carbon nano tube was considered for good candidate for metal-free catalyst as cathode of Li-air battery under hybrid electrolyte because of its good properties such as low cost, good electrical conductivity, excellent mechanical strength and flexibility.

Huang et al. reported the CNF composite with Co and Ni by electrospun method as cathode material in Li-O<sub>2</sub> batteries led to high cyclic stability and low initial

overpotential. They suggested that the graphitization of CNF was contributed to electrical conductivity and carbon stability [11].

Bhuvaneshwari et al. has reported that the comparison of electrochemical performance for carbon nanofiber (CNF) composite with  $\text{LiFePO}_4$  and pristine  $\text{LiFePO}_4$  as a cathode in Li-ion batteries. The carbon nanofiber (CNF) composite with  $\text{LiFePO}_4$  showed decreased overpotential, furthermore the performance fading also reduced during 4 cycles. Thus, carbon nanofiber (CNF) composite with  $\text{LiFePO}_4$  had better electrochemical with stability were improved during discharge-charge performance than that of pristine  $\text{LiFePO}_4$ . They considered that the improvement of electro performance for carbon nanofiber (CNF) composite with  $\text{LiFePO}_4$  attributed to good conductivity of CNF [12].

Jang et al. investigated the electrochemical performance of CNF composed with graphite in Li-ion batteries [13]. The CNF composite with graphite showed improved discharge capacity as well as cycleability. They suggested that the specific morphology of CNF-graphite led to improve cyclability and high rate capability in Li-ion batteries. Also, they showed that CNF grown on graphite had the large surface area.

Therefore, it considered that the CNF composited with carbon materials may provide sufficiently large active site as well as improving the kinetics of ORR due to the large surface area and high conductivity. In addition, the high electro conductivity of CNF could be advanced durability of cycle performance. However, the CNF composite with carbon materials had not yet been reported in the Li-air batteries. Herein, CNF-CB composites were prepared and their electrochemical properties as an air-electrode for hybrid Li-air battery were studied in the discharge-charge performance.

## **3.2 Experimental**

### **3.2.1 Preparation of CNF-CB**

CNF-CB composites were fabricated by CVD, as illustrated in Figure 3-1. The FeNi supported CB were prepared from Iron(III) nitrate nonahydrate ( $\text{Fe}(\text{NO}_3)_3 \cdot 9\text{H}_2\text{O}$ ) and Nickel(II) nitrate hexahydrate ( $\text{Ni}(\text{NO}_3)_2 \cdot 6\text{H}_2\text{O}$ ) to provide nuclei for CNF on CB. Firstly, 397.09 mg of  $\text{Fe}(\text{NO}_3)_3 \cdot 9\text{H}_2\text{O}$  and 144 mg of  $\text{Ni}(\text{NO}_3)_2 \cdot 6\text{H}_2\text{O}$  were dissolved in

250 ml of ethanol while stirring for 30 min at room temperature. Then, CB of 1 g was added to the Fe/Ni mixture solution and stirred for 2 h at room temperature. Ethanol was evaporated at 80 °C. Finally, the obtained FeNi@CB was dried in an oven at 100 °C overnight in the air condition.

The powdered FeNi@CB catalyst was placed in a quartz boat at the center of a reactor tube in the furnace to grow CNF on the CB surface. After reduction in 20 % H<sub>2</sub>/He for 140 min, He gas was reflushed for 1 h before introduction of C<sub>2</sub>H<sub>4</sub> gas and He mixture for 30 min at each reaction temperature (640-840 °C). Then, He gas was flowed during cool down to ambient temperature. The prepared CNF-FeNi@CB was washed with 2M HCl and distilled water to remove Fe and Ni metals. Finally, the obtained CNF-CB was dried at the temperature of 80 °C. The CNF-CB was denoted to CNF-CB 640, CNF-CB 740 and CNF-CB 840 by the CNF grown temperature.

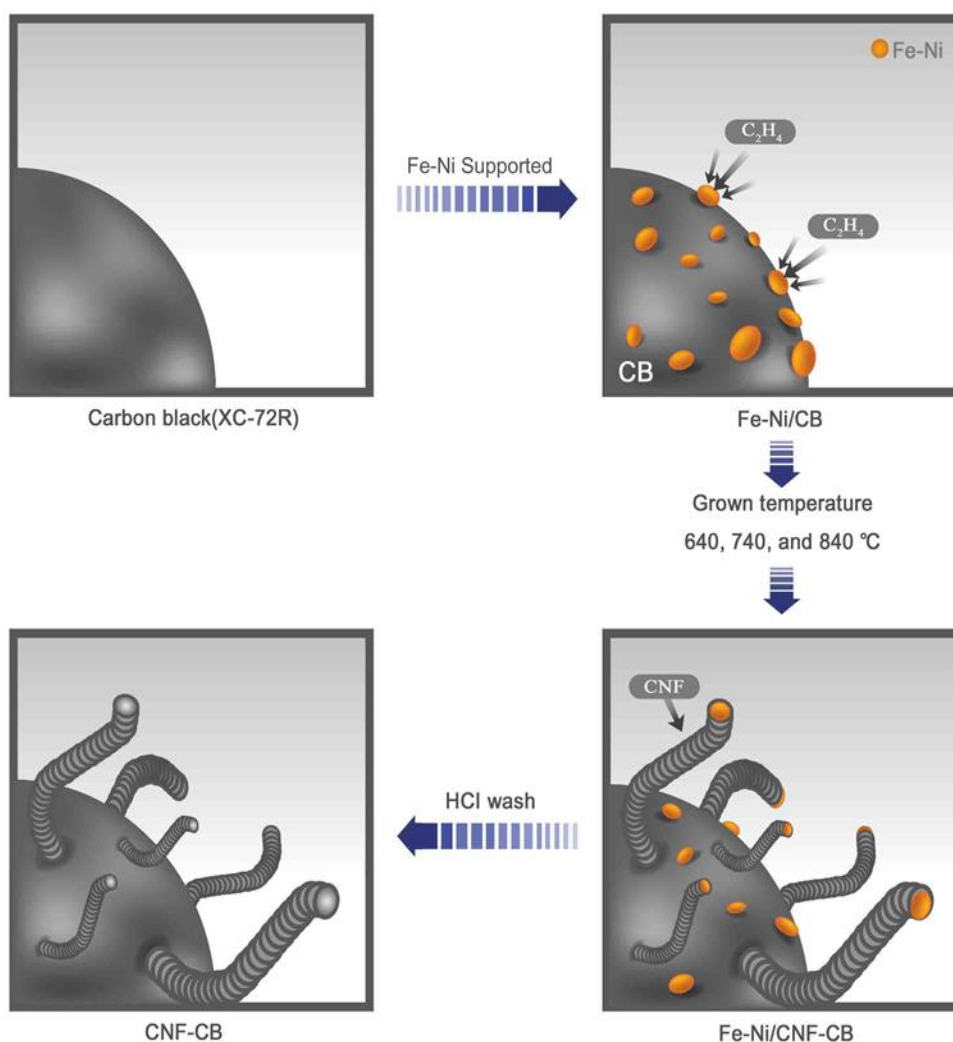


Figure 3-1. Preparation of CNF-CB by chemical vapour deposition (CVD) on different temperature from 640 °C to 840 °C.

### 3.2.2 Assembly and testing of hybrid Li-air battery

The electrochemical test for hybrid Li-air batteries was described in our previous reports [7,9,19]. 1M LiClO<sub>4</sub> EC/DEC and 1M LiOH were used as an anodic and a cathodic electrolytes, respectively. Li<sub>(1+x+y)</sub>Al<sub>x</sub>(Ti, Ge)<sub>2-x</sub>SiyP<sub>(3-y)</sub>O<sub>12</sub> (LiSICON) plate was used as an organic / inorganic electrolyte membrane to prevent intermixing of both solutions. For the preparation of cathode, CNF-CB, acetylene black (AB) and 10 wt%

polytetrafluorethyrene (PTFE) binder in a weight ratio of 80 : 5 : 15 were mixed and then pressed onto the Ni mesh. The discharge-charge performance was measured in a voltage range of 2.5 - 4.2 V at the current density of 0.5 mA cm<sup>-2</sup> each 2 h. The ORR activity was examined using a rotating disk electrode (RDE) in the 1M LiOH at room temperature under N<sub>2</sub>/O<sub>2</sub> conditions. The catalysts were loaded on glassy carbon electrode (0.285 cm<sup>2</sup>) with diluted (1:50 in methanol) 5 wt% Nafion solution (Aldrich). The RDE used a 3-electrode system where platinum (Pt) and a silver/silver chloride electrode (Ag/AgCl) were used as a counter electrode and reference electrode, respectively.

### **3.2.3 Characterization of CNF-CB**

The specific surface area of all samples was measured by Brunauer-Emmett-Teller (BET). Raman spectroscopy (Raman) and Thermogravimetry-Differential Thermal Analysis (TG-DTA) were used to compare a graphitization of CNF-CB. The morphology of CNF-CB was examined by scanning electron microscope (SEM) and transmission electron microscope (TEM). A commercial CB was used as a reference at the same condition.

## **3.3 Result and discussion**

### **3.3.1 The characteristics for CNF-CB**

The results of XRD pattern was measured from 20-80 ° of 2 theta, which shown as Figure 3-2. CNF-CB 740 showed slightly higher graphitization than that of CNF-CB 640. On the other hands, the XRD pattern of CNF-CB 740 showed that some impurity was contained in CNF-CB, that pattern was corresponded to Ni<sub>3</sub>Fe. The CNF-CB 840 was obtained stronger XRD pattern peak for Ni<sub>3</sub>Fe composite than that of other materials especially. The Ni<sub>3</sub>Fe might be composed during CVD procedure each different temperature. Thus, the high temperature of 840 °C could be supplied better condition than other temperature to accomplished high crystallization of Ni<sub>3</sub>Fe

composite. Furthermore, this result indicated that metal ions, which was used to grow CNF, was not remove perfectly after acidic wash by HCl solution.

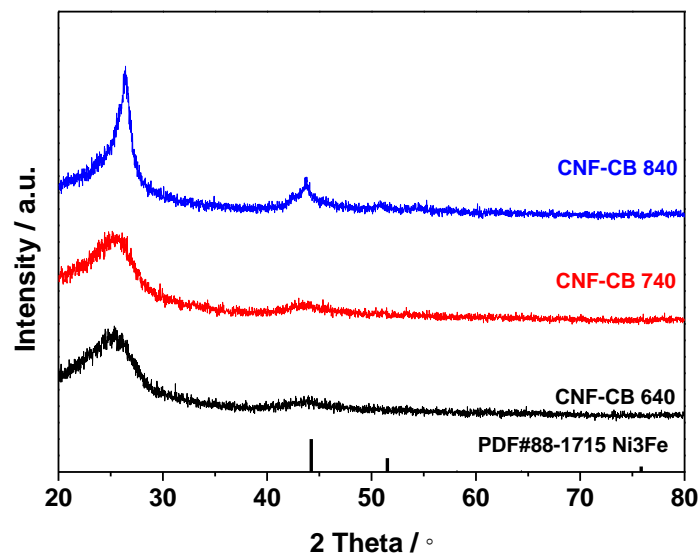


Figure 3-2. The XRD pattern of CNF-CB from 20° to 80° of 2 theta degrees. And the peak intensity, which corresponded with Ni<sub>3</sub>Fe of metallic composite.

Therefore, the TG-DTA analysis was accomplished to measure quantitative analysis of Ni<sub>3</sub>Fe composite. Furthermore, the graphitization also could be compared, which shown as Figure 3-3. The temperature area for TG-DTA measurement was from room temperature to 900 °C in air condition and 100 ml s<sup>-1</sup> of fellow speed. Moreover, the temperature raising rate was 10 °C min<sup>-1</sup>. From the TG curve, it showed nothing mass loss for initial area (~300 °C), which indicated that CNF-CB samples have not any functional group on the surface. Moreover, they showed different thermal decompose temperature for each samples as well as Ni<sub>3</sub>Fe was remained after carbon burned out. The quantity of remained Ni<sub>3</sub>Fe was very small (~ 3 wt%), however the amount of that was different each sample. The CNF-CB 640 contained most Ni<sub>3</sub>Fe, which was 2.82 wt%. On the other hands, CNF-CB 740 had least amount of Ni<sub>3</sub>Fe, which was 1.84 wt%. The CNF-CB 840 has 2.81 wt% of Ni<sub>3</sub>Fe. The content of Ni<sub>3</sub>Fe was shown in table 3-1.

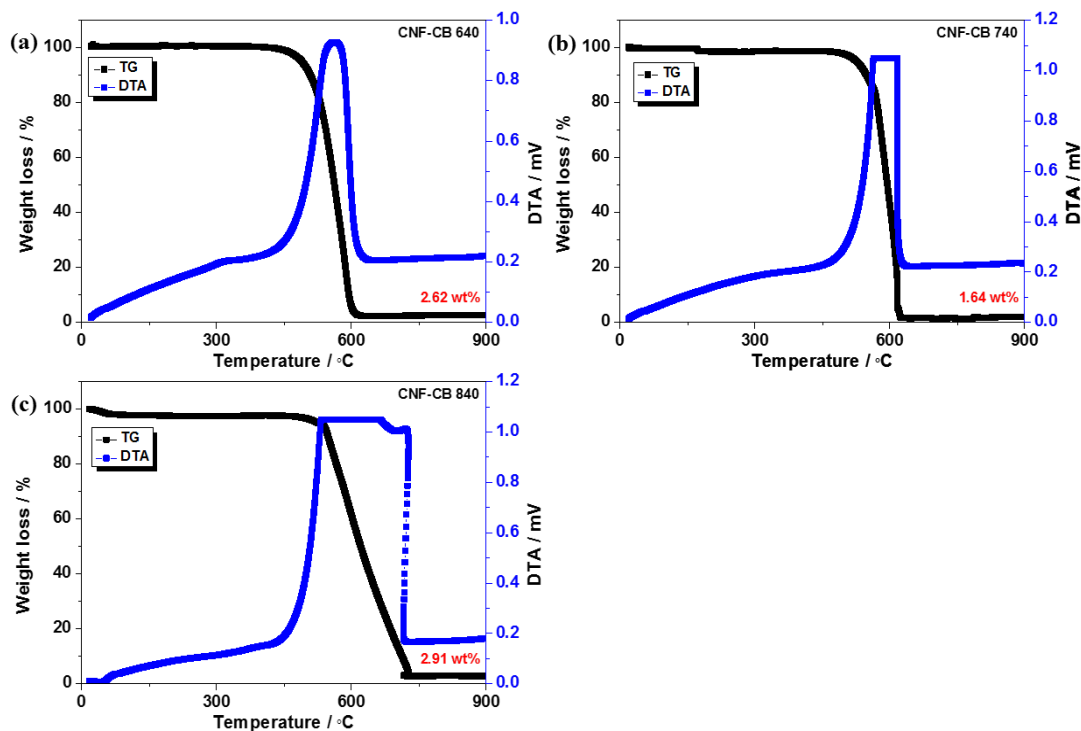


Figure 3-3. The thermo gravimetric (TG) and differential thermal analysis (DTA) curve from room temperature to 900 °C of temperature range under air condition (100 ml min<sup>-1</sup>) and the 10 °C min<sup>-1</sup> of temperature raising speed for CNF-CB 640 (a), CNF-CB 740 (b) and CNF-CB 840 (c), respectively.

Sample	Ratio of Contents for Ni <sub>3</sub> Fe (wt%)
CNF-CB 640	2.82
CNF-CB 740	1.84
CNF-CB 840	2.81

Table 3-1. The Ratio of remained amount for Ni<sub>3</sub>Fe in CNF-CB 640, CNF-CB 740 and CNF-CB 840 after acidic wash by HCl solution.

The combustion temperature of CNF-CB was confirmed by DTA curve. DTA curve showed strength of voltage. The voltage was occurred when material was bund out. Furthermore, the strength for rate of spread was able to be supposed through voltage values. Thus, the voltage value informed activation of combustion for materials. In addition, that supplied information for crystalline in carbon case. The highest voltage

values for DTA were 550, 565 and 533 °C for CNF-CB 640, CNF-CB 740 and CNF-CB 840, respectively. This result indicated that CNF-CB 740 had highest carbon crystalline than that of CNF-CB 640 and CNF-CB 840. On the other hands, the CNF-CB 840 showed burned out on lowest temperature, which indicated that the CNF-CB 840 had lowest graphitization.

The results of a specific surface area by nitrogen adsorption were given in Figure 3-4. The CNF-CB showed same N<sub>2</sub> adsorption-desorption hysteresis curve, which indicated that the all of CNF sample has same pore structure. According to IUPAC standard, the carbon porosity could separate for micro pore, meso pore and macro pore by hysteresis loop. The average pore diameter of micro pore was under 2 nm. The average diameter of macro pore was over the 50 nm. On the other hands, meso pore had from 2 nm to 50 nm for average diameter. Each porosity type had difference hysteresis loop for N<sub>2</sub> adsorption-desorption. The CNF-CB showed macro type hysteresis loop, which indicated that the CNF-CB two things. First, the CNF-CB have porous structure. Second, it was macro pore, thus its diameter was over 50 nm.

Nevertheless, the specific surface area of CNF-CB was different by CVD temperature. The BET surface area of CNF-CB were 254, 324 and 251 m<sup>2</sup> g<sup>-1</sup> for CNF-CB 640, CNF-CB 740 and CNF-CB 840, respectively. This result indicated that the CVD temperature had an effect for specific surface area of carbon materials, thus the grown of CNF had a role to increase surface area. The CNF-CB material commonly showed higher specific surface area than that of CB. The BET surface area of CB was 218 m<sup>2</sup> g<sup>-1</sup> as shown Table 3-2.

	BET surface area / m <sup>2</sup> g <sup>-1</sup>
CNF-CB 640	254
CNF-CB 740	324
CNF-CB 840	251
CB	218

Table 3-2. The BET surface area for CNF-CB 640, CNF-CB 740, CNF-CB 840 and CB respectively.

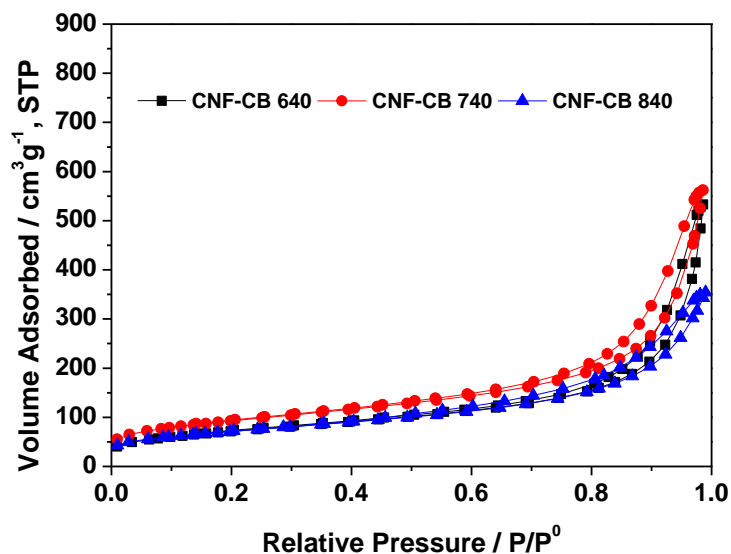


Figure 3-4. The hysteresis loop and BET specific surface area for CNF-CB 640, CNF-CB 740 and CNF-CB 840, respectively.

The graphite structure of all CNF-CB and CB was also evaluated by Raman spectroscopy measurements as shown in Figure 3-5 (a). All measured samples exhibited two distinct bands appearing at around  $1324\text{ cm}^{-1}$  (D-band) and  $1597\text{ cm}^{-1}$  (G-band). The D and G bands reflect the structure of  $\text{sp}^3$  and  $\text{sp}^2$  hybridized carbon atoms, indicating disordered graphite and the ordered state of carbon material, respectively [14-16]. The degree of the graphitization on CNF-CB can be quantified by the intensity ratio of the D to G bands, as shown Figure 3-5 (b). The peak intensity ratio ( $I_D/I_G$ ) was 1.68, 1.50, 2.14 and 1.86 for CNF-CB 640, CNF-CB 740, CNF-CB 840 and CB, respectively. The small  $I_D/I_G$  ratio of CNF-CB 740 suggests that CNF-CB 740 be a best graphitization.

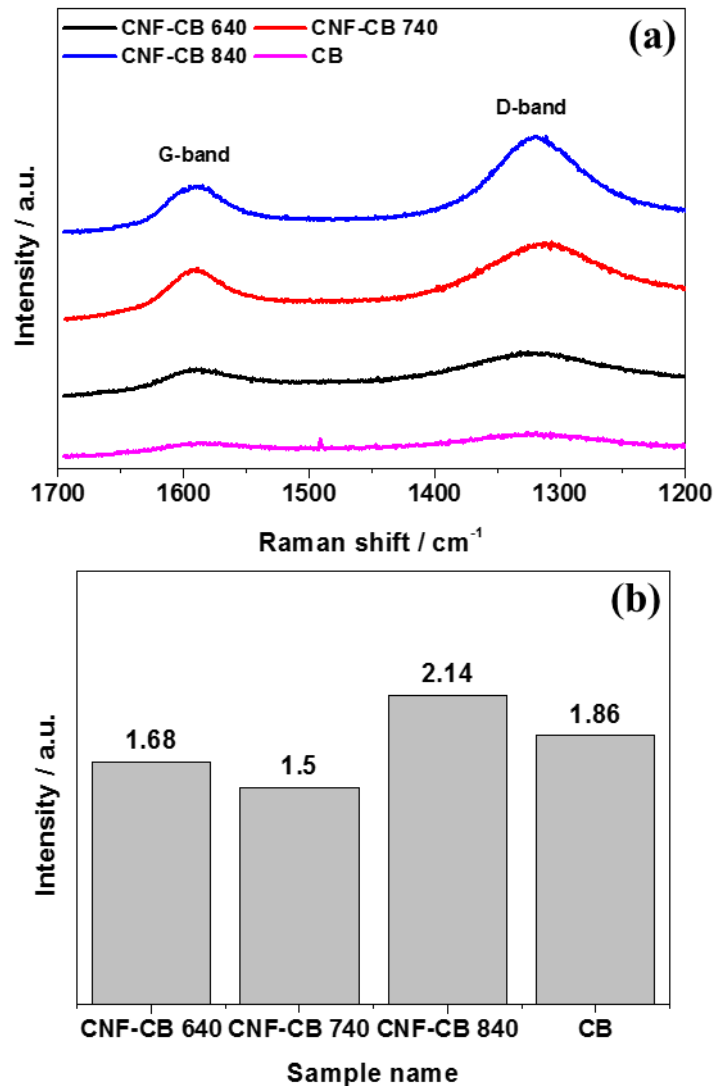


Figure 3-5. The Raman spectroscopy (a) and comparison of  $I_D/I_G$  ratio (b) from intensity value of D-band and G-band as Raman result for CNF-CB 640, CNF-CB 740, CNF-CB 840 and CB, respectively.

The structure and morphology of the CNF-CB were observed using SEM and TEM measurement. Figure 3-6 displayed the typical SEM images of CNF-CB 640, CNF-CB 740, CNF-CB 840 and CB, respectively. The CNF-CB 640 and CNF-CB 740 exhibited CNF grown on the CB surface with entangled and curl structure. However, the CNF as CNF-CB 740 was seen as thicker and longer than that of CNF-CB 640. Furthermore, the quantity also seem to more than that of CNF-CB 640. Moreover, only a few fibers were observed on the surface for the CNF-CB 840. On the other hands, pristine CB

showed that sphere of various diameter was aggregated, which had a very clean surface.

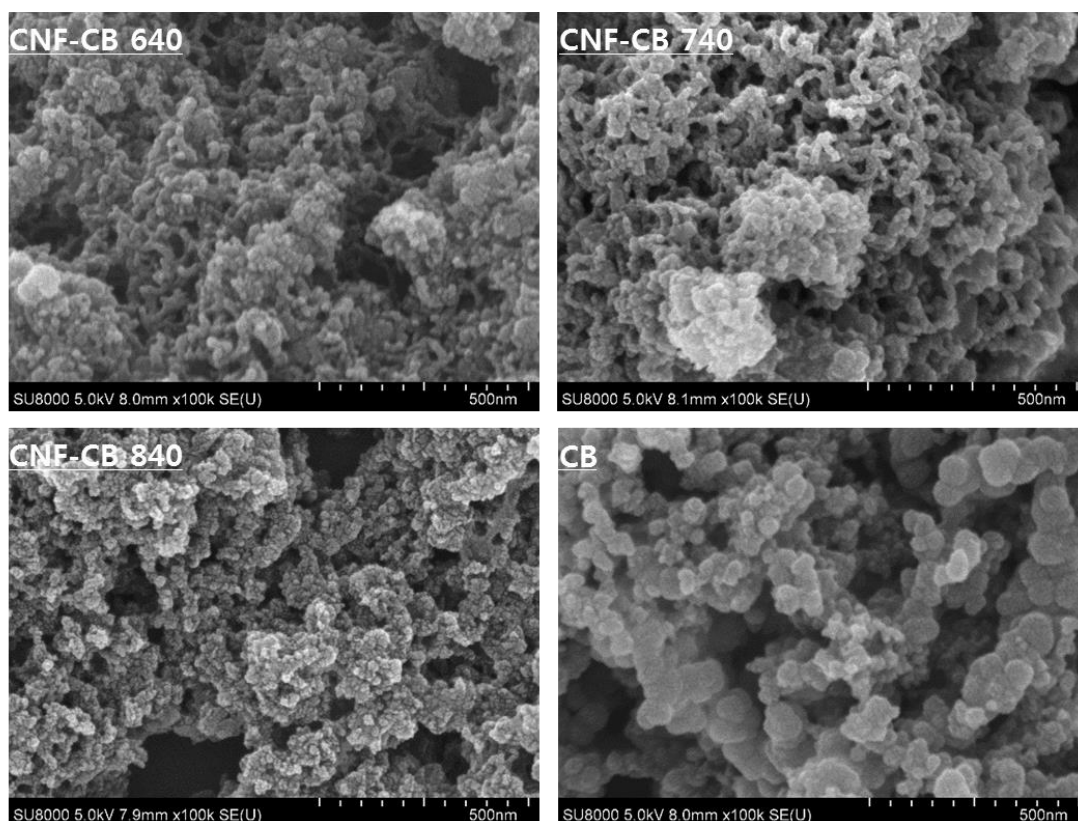


Figure 3-6. The SEM images for CNF-CB 640, CNF-CB 740, CNF-CB 840 and CB, respectively.

This result reflects importance of CNF grown up temperature. Such a correlation between heat treatment temperature and structure of CNF was examined under TEM. Figure 3-7 shows the TEM images of all CNF-CB samples. From the nanostructure, CNF-CB 640 and 740 samples provided selectively thin fibers of near 10 nm in a diameter. For the CNF-CB 640 and 740, a tubular structure though a CB particles was observed. On the other hands, the CNF of CNF-CB 840 showed no tubular structure and random directions in relation to the fiber axis. These results indicated that the formation of the CNF on the CB surface influenced the heat treatment temperature and the heat treatment temperature of 640 °C, 740 °C favor the formation of CNF.

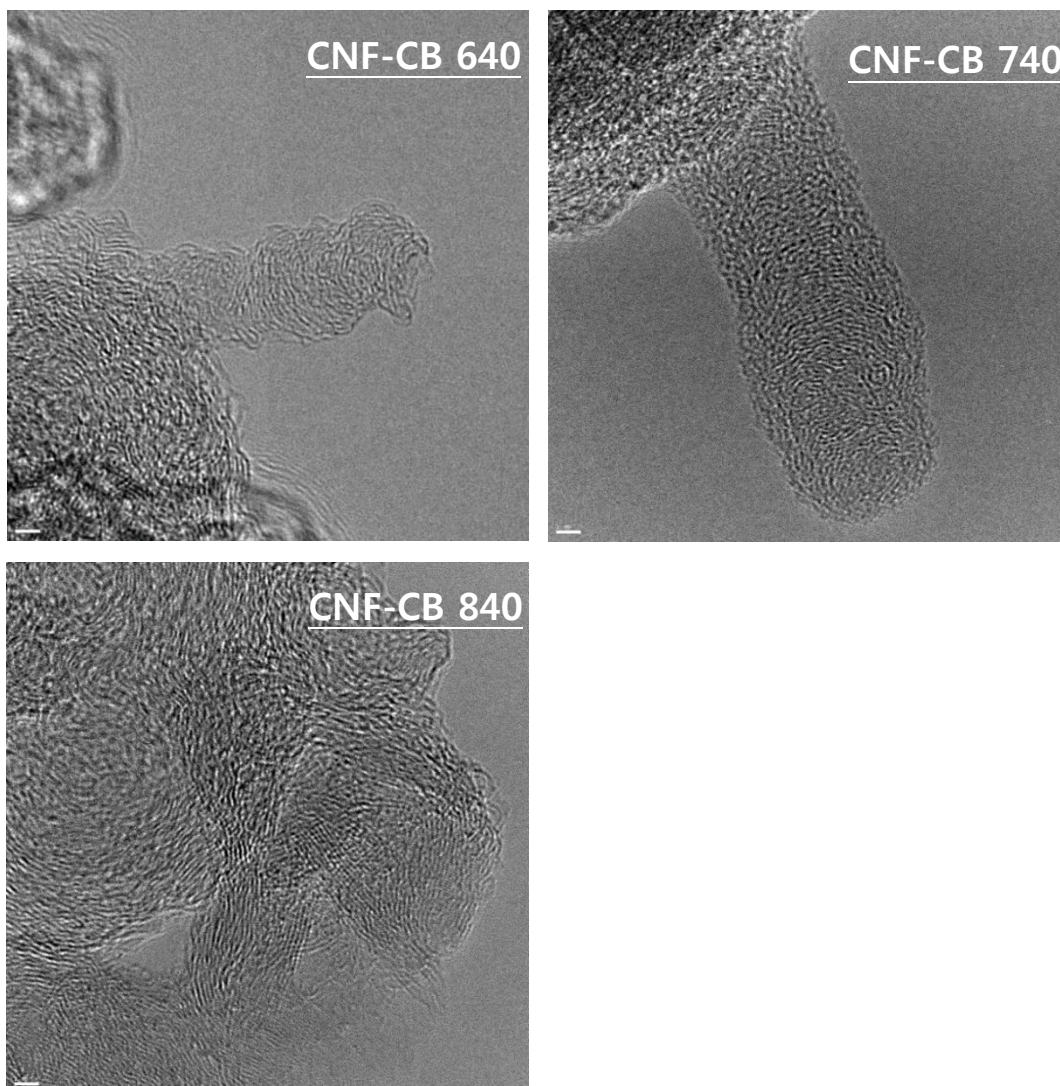


Figure 3-7. The TEM images for CNF-CB 640, CNF-CB 740, CNF-CB 840 and CB, respectively.

### 3.3.2 Analysis of electrochemical characterization for CNF-CB series

Figure 3-8 showed the cycle voltammetry of CNF-CB 640, 740, 840 and CB at a scan rate of  $20 \text{ mV s}^{-1}$  with a rotating rate of 500 rpm under 0.1M KOH in  $\text{N}_2$  and  $\text{O}_2$  condition. The onset potential of ORR as shown in table 3-3, which was about -0.18, -0.12, -0.17 and -0.14 V vs. Ag/AgCl for CNF-CB 640, 740, 840 and CB, respectively. At an overpotential of -0.3 V, the current density of CNF-CB 640, 740, 840 and CB was exhibited -0.85, -1.22, -0.92 and -0.9  $\text{mA cm}^{-2}$ , respectively. It indicated that CNF-CB

640 and CNF-CB 740 had higher catalytic activity for ORR than that of CNF-CB 840 and CB.

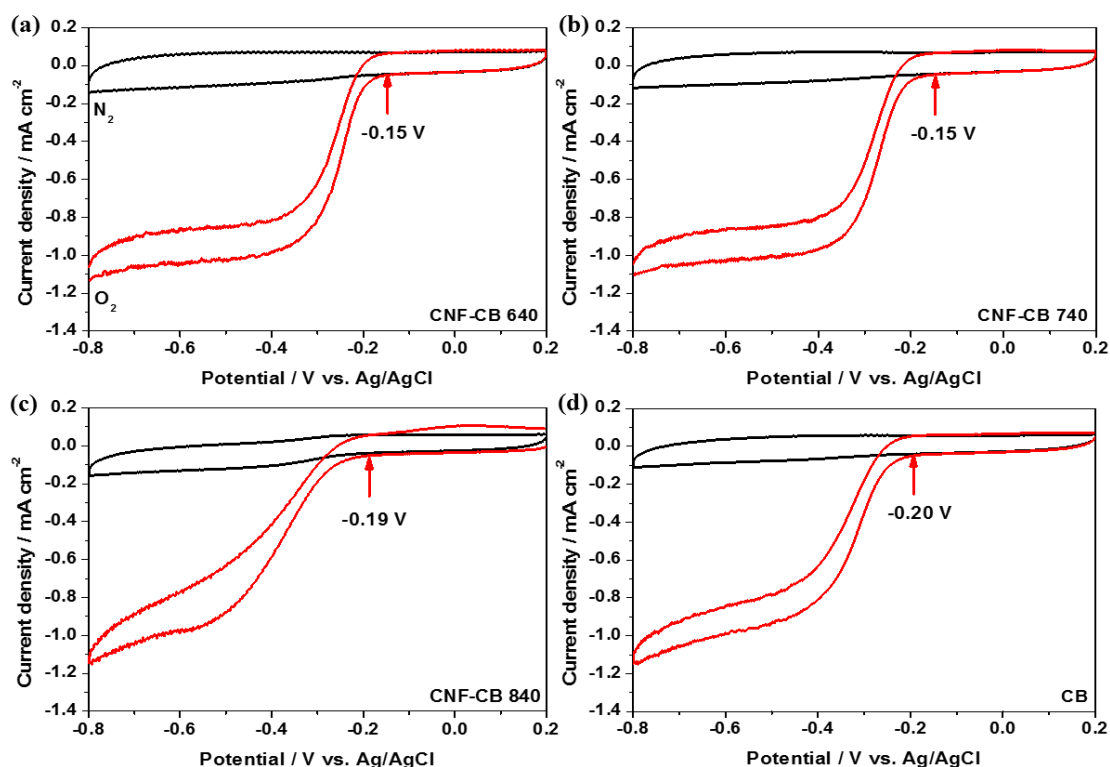


Figure 3-8. The cycle voltammetry (CV) analysis at a scan rate of  $20 \text{ mV s}^{-1}$  with a rotating rate of 500 rpm under 0.1M KOH in  $\text{N}_2$  and  $\text{O}_2$  condition for CNF-CB 640 (a), CNF-CB 740 (b), CNF-CB 840 (c) and CB (d), respectively.

Sample	The onset potential (V vs. Ag/AgCl)
CNF-CB 640	-0.15
CNF-CB 740	-0.15
CNF-CB 840	-0.19
CB	-0.20

Table 3-3. The onset potential of CNF-CB 640, CNF-CB 740, CNF-CB 840 and CB for oxygen reduction reaction (ORR).

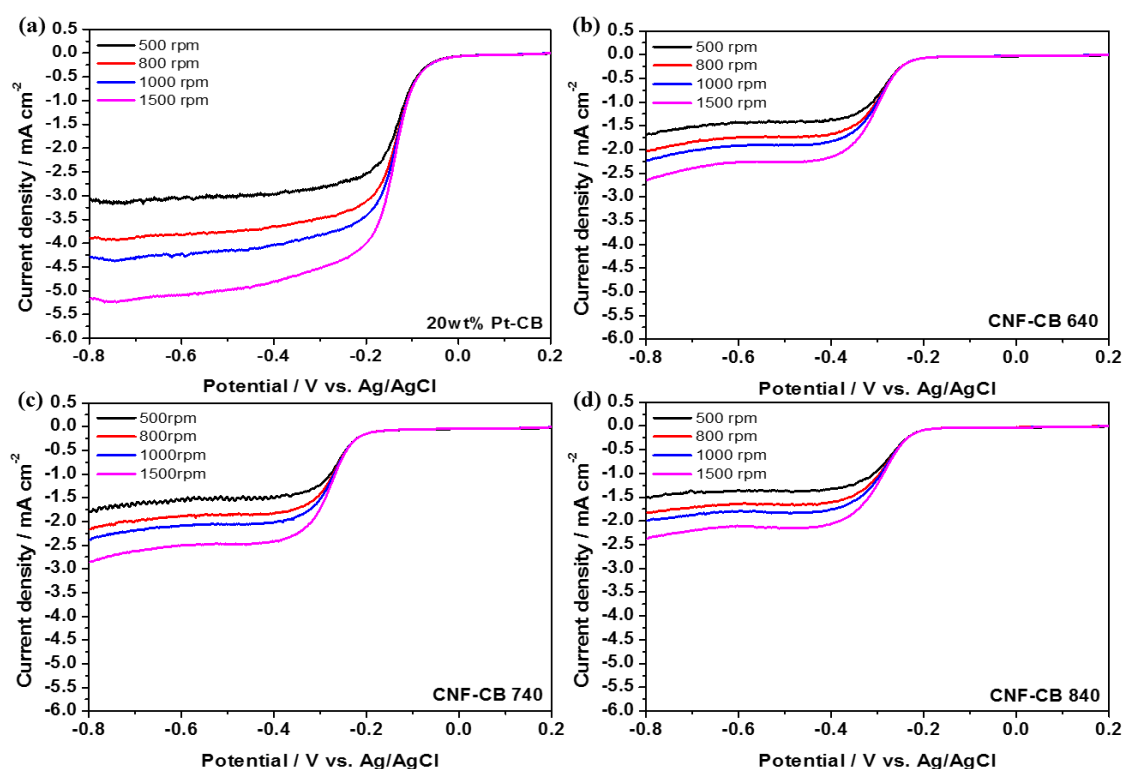


Figure 3-9. The linear sweep voltammetry (LSV) analysis at a scan rate of  $20 \text{ mV s}^{-1}$  with a rotating rate of 500 rpm to 1500 rpm under 0.1M KOH in  $\text{O}_2$  condition for 0wt% Pt-CB (a), CNF-CB 640 (b), CNF-CB 740 (c) and CNF-CB 840 (d), respectively.

The figure 3-9 showed linear sweep voltammetry (LSV) curves for 20 wt% Pt-CB, CNF-CB 640, CNF-CB 740 and CNF-CB 840 at a scan rate of  $20 \text{ mV s}^{-1}$  under 0.1M KOH. The ORR of 20 wt% Pt-CB was diffusion controlled when the potential was less than  $-0.25 \text{ V}$ . On the other hand, the CNF-CB 740 did not reach mass transport limiting voltage in the potential region from  $-0.2 \text{ V}$  to  $-0.4 \text{ V}$ .

The K-L equation was usually used to calculate the electrons transfer number during the ORR. The K-L equation was followed

$$\frac{1}{i} = \frac{1}{i_k} + \frac{1}{i_{l,c}}$$

$$i_{l,c} = 0.62nFAD_0^{2/3} w^{1/2} \nu^{-1/6} C_0^*$$

where,  $i_{l,c}$  was the limiting current,  $n$  the number of electrons transferred in the half

reaction,  $F$  the Faraday constant ( $96485 \text{ C mol}^{-1}$ ),  $A$  the electrode area ( $0.285 \text{ cm}^2$ ),  $D_0$  the diffusion coefficient ( $1.9 \times 10^{-5} \text{ cm}^2 \text{ s}^{-1}$ ),  $w$  the angular rotation rate of the electrode,  $\nu$  the kinematic viscosity ( $0.01 \text{ cm}^2 \text{ s}^{-1}$ ), and  $C_0^*$  analyze concentration ( $1.2 \times 10^{-6} \text{ mol cm}^3$ ). The corresponding K-L plots of 20 wt% Pt-CB, CNF-CB 640, CNF-CB 740 and CNF-CB 840 in Figure 3-10 displayed good linearity and parallelism, indicating the first-order reaction kinetics for ORR. The electron transfer number of 20 wt% Pt-CB was calculated to be 3.9 at -0.4 V, which near approaches the  $4e^-$  electron transfer number ( $n$ ) of the Pt-based catalyst in aqueous electrolyte for ORR [17]. The CNF-CB series were according to their corresponding RDE curves. The electron transfer number was calculated as shown table 3-4. The electron transferred number was to be 1.8, 1.8, 1.7 and 2.2 at -0.4 V for CNF-CB 640, CNF-CB 740, CNF-CB 840 and CB, respectively. All of the CNF-CB were suggesting a  $2e^-$  reduction process in aqueous electrolyte for ORR.

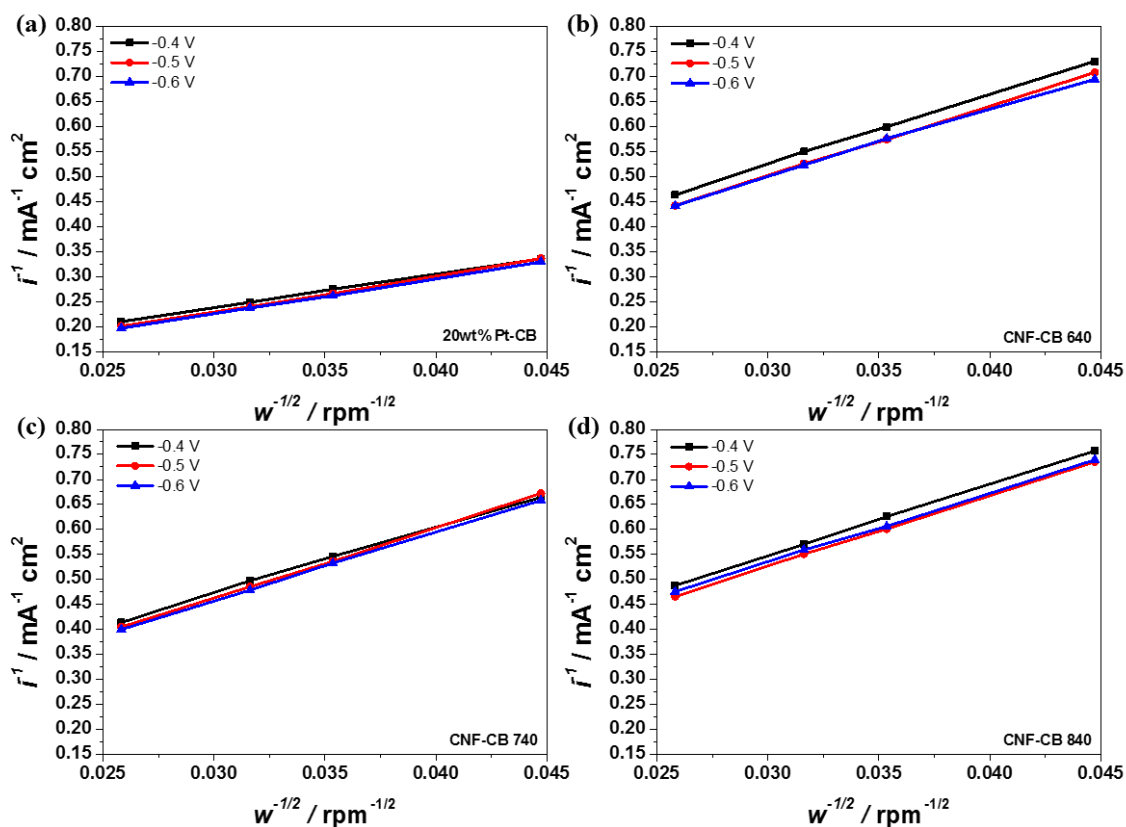


Figure 3-10. The Koutechky-Levich (K-L) plots corresponded LSV result of 20 wt% Pt-CB (a), CNF-CB 640 (b), CNF-CB 740 (c) and CNF-CB 840 (d), respectively.

Sample	The electron transferred number
20wt% Pt-CB	3.9
CNF-CB 640	1.8
CNF-CB 740	1.8
CNF-CB 840	1.7
CB	2.2

Table 3-4. The electron transferred number of 20wt% Pt-CB, CNF-CB 640, CNF-CB 740, CNF-CB 840 and CB for oxygen reduction reaction (ORR).

Nevertheless, the CNF-CB 740 showed better discharge performance than that of CNF-CB 640 and CNF-CB 840. Figure 3-11 showed the discharge performance of CNF-CB 640, CNF-CB 740 and CNF-CB 840 for 24h at current density of  $0.5 \text{ mA cm}^{-1}$  in Li-air battery under hybrid electrolyte condition. The CNF-CB had stable discharge performance without fading, which also showed discharge potential at 2.85, 2.80 and 2.80 V vs.  $\text{Li}^+/\text{Li}$  for CNF-CB 740, CNF-CB 640 and CNF-CB 840, respectively. This result indicated that CNF-CB 740 had higher electro catalytic activity for ORR than that of CNF-CB 640 and CNF-CB 840 under hybrid electrolyte.

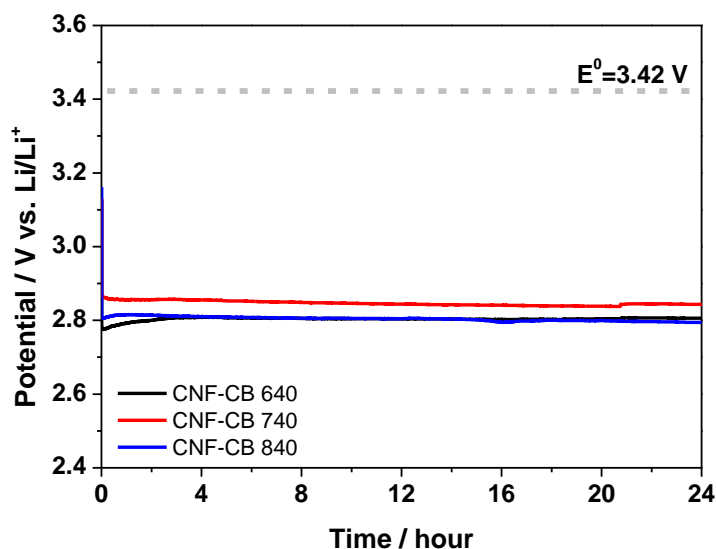


Figure 3-11. The discharge performance at a current density of  $0.5 \text{ mA cm}^{-1}$  for 24 h under hybrid electrolyte for CNF-CB 640, CNF-CB 740 and CNF-CB 840, respectively.

Moreover, the CNF-CB 740 was obtained best performance such as long cycle number and high stability than that of CNF-CB 640, CNF-CB 840 and CB for discharge-charge performance as shown in Figure 3-12. The discharge-charge performance was measured at  $0.5 \text{ mA cm}^{-2}$  with discharge and charge each 2h in cut off voltage from 2.5 V to 4.2 V. The discharge-charge performance were operated during 264, 280, 176 and 72 hours for CNF-CB 640, CNF-CB 740, CNF-CB 840 and CB, respectively. Thus, the hybrid Li-air battery were working for 66, 75, 44 and 18 cycle for CNF-CB 640, CNF-CB 740, CNF-CB 840 and CB, respectively. The discharge potential of hybrid Li-air battery cell was increased gradually during cell operating, which was over the cut off voltage after that time. In contrast, the charge potential showed smaller increase for overpotential than that of discharge overpotential. Thus, this result indicated that hybrid Li-air battery cell had more performance fading at discharge performance than charge performance. In addition, the discharge potential of hybrid Li-air battery cell based on CNF-CB showed higher durability for discharge-charge performance than that of CB. This result indicated that grown CNF on the carbon surface had something importance role to develop carbon durability.

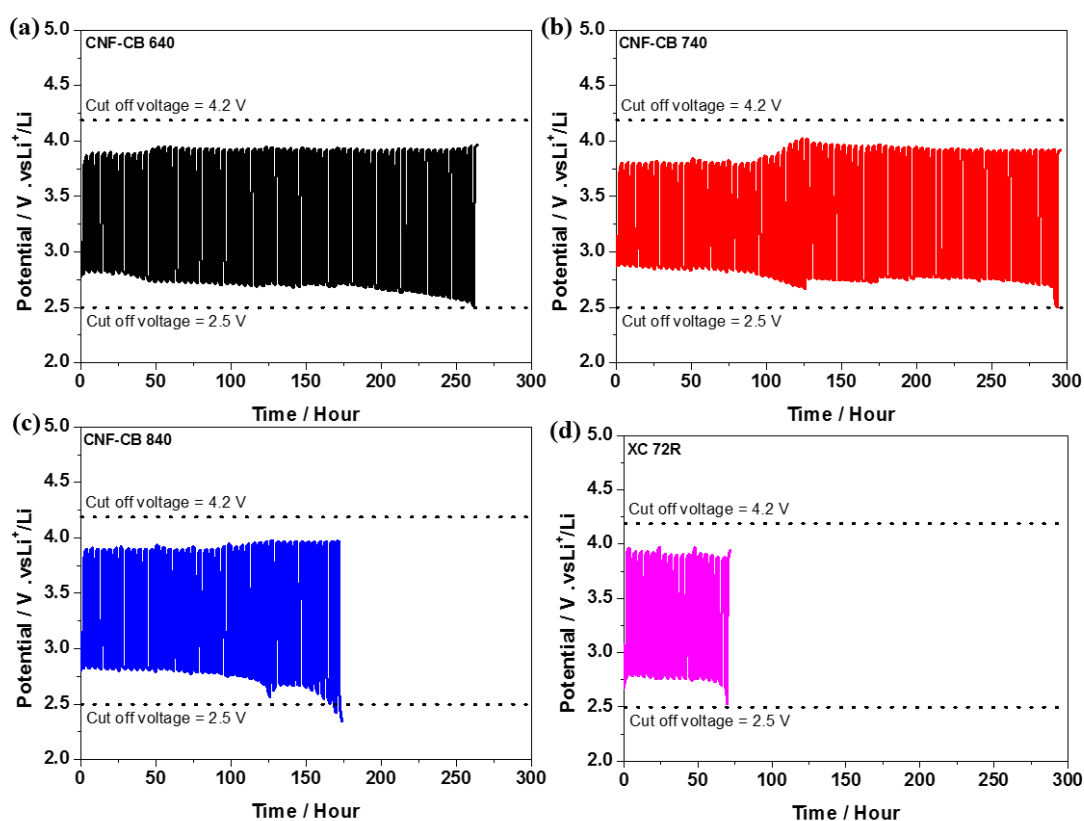


Figure 3-12. The discharge-charge performance at a current density of  $0.5 \text{ mA cm}^{-2}$  each 2 h under hybrid electrolyte for CNF-CB 640 (a), CNF-CB 740 (b), CNF-CB 840 (c) and CB (d), respectively.

Figure 3-13 showed the discharge and charge voltages obtained for all measured samples during cycling at a range of 2.5 to 4.2 V. The discharge voltage of CNF-CB 640, CNF-CB 740, CNF-CB 840 and CB at the 1<sup>st</sup> cycle was 2.80, 2.75 and 2.77 V vs.  $\text{Li}^+/\text{Li}$ , respectively. Comparing with the discharge voltage of CNF-CB 740 at the 1<sup>st</sup> cycle was 2.88 V vs.  $\text{Li}^+/\text{Li}$ , 1<sup>st</sup> discharge voltage of CNF-CB 640, CNF-CB 840 and CB was small as 0.013 V, indicating the best ORR performance of CNF-CB 740. With cycling, the discharge voltage of the CNF-CB 640, CNF-CB 740 and CNF-CB 840 decreased and the discharge voltage was reached at 2.5 V vs.  $\text{Li}/\text{Li}^+$  after 66, 70 and 44 cycles, respectively. While, the CB showed discharge voltage of 2.52 V vs.  $\text{Li}^+/\text{Li}$  after 18 cycles. It is thus considered that the CNF grown on CB led to improve the cycle stability in hybrid Li-air batteries. The CNF-CB 740 enabled long term cycling performance of hybrid Li-air batteries near 300 h, which was much longer times than

those of reported Li-air batteries with carbon cathode (120h, 200h ) [1,18].

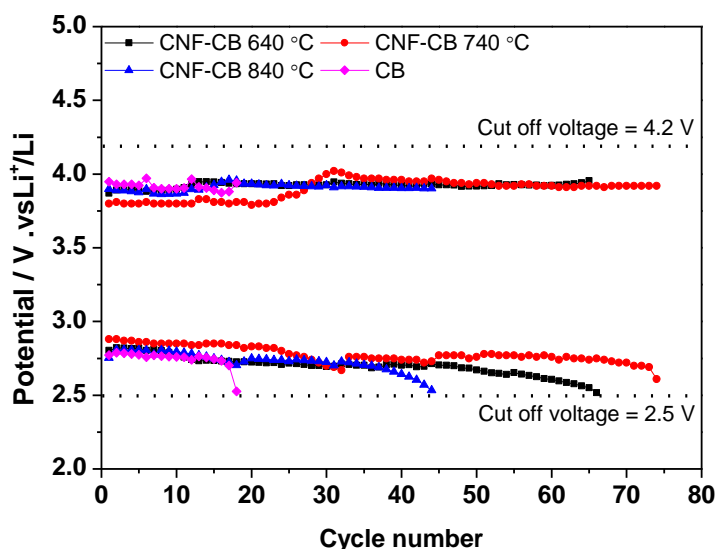


Figure 3-13. The discharge and charge voltages obtained for all measured samples during cycling at a range of 2.5 to 4.2 V for CNF-CB 640, CNF-CB 740, CNF-CB 840 and CB, respectively.

Figure 3-14 showed the discharge rate performance of hybrid Li-air batteries with CNF-CB 640, CNF-CB 740, CNF-CB 840 and CB electrodes at various current densities up to  $1.5 \text{ mA cm}^{-2}$ . The operating voltage was at 3.1, 3.12, 3.1 and 3.06 V vs.  $\text{Li/Li}^+$  at  $0.001 \text{ mA cm}^{-2}$  for CNF-CB 640, CNF-CB 740, CNF-CB 840 and CB, respectively. At  $1.5 \text{ mA cm}^{-2}$ , the cell potential of the CNF-CB 740 was as high as 2.44 V vs.  $\text{Li/Li}^+$  about 300 mV better than that of the CB. On the other hands, the CNF-CB 640 and 740 were obtained cell potential at 2.36 and 2.31 V vs.  $\text{Li/Li}^+$ , respectively. Thus, CNF-CB 640 and CNF-CB 840 had higher potential for about 220 and 250 mV than that of CB at  $1.5 \text{ mA cm}^{-2}$ .

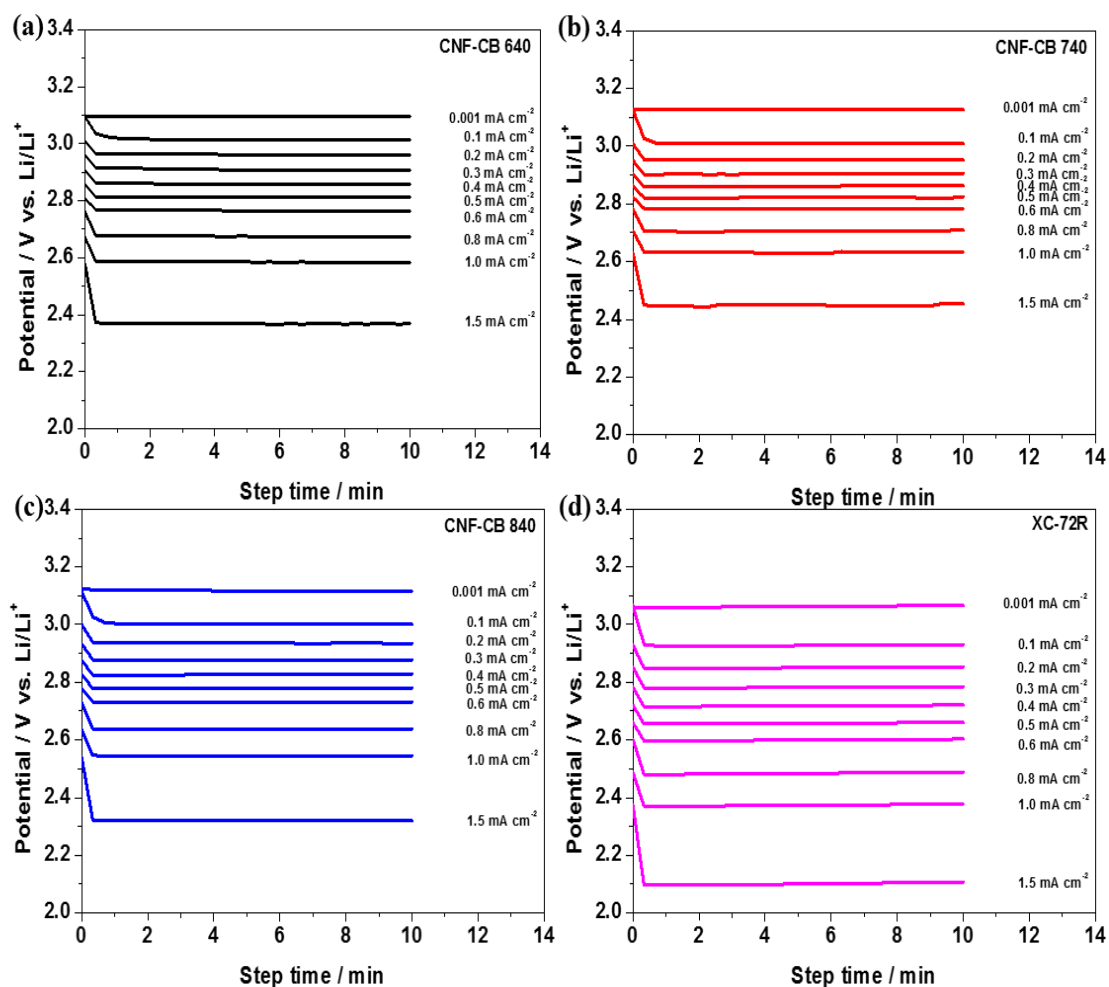


Figure 3-14. The discharge rate performance of hybrid Li-air batteries with CNF-CB 640 (a), CNF-CB 740 (b), CNF-CB 840 (c) and CB (d) electrodes at various current densities up to  $1.5 \text{ mA cm}^{-2}$

This result indicated that CNF-CB showed higher stability for discharge at high current density. However, each CNF-CB material was different for discharge performance depend on grown temperature of CNF. With increasing the current densities, linear decrease of the operating voltage of both samples is clearly observed in Figure 3-14.

We estimated the internal resistance of both samples by analyzing the I-V curve in the Figure 3-15. The internal resistance was calculated by Ohm's equation;

$$\Omega = \frac{\Delta V}{\Delta I}$$

Where,  $\Omega$  was internal resistance,  $\Delta V$  was increased potential and  $\Delta I$  was increased current, respectively.

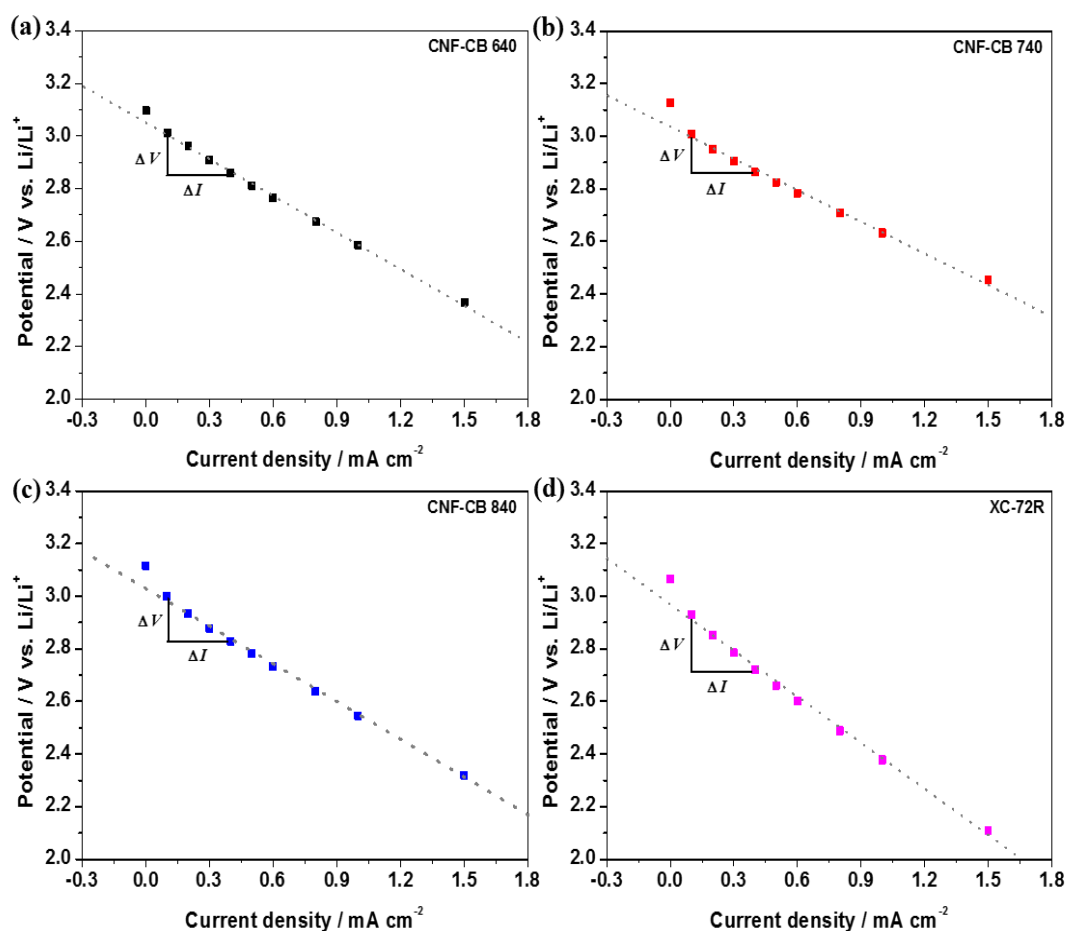


Figure 3-15. The internal resistance for CNF-CB 640 (a), CNF-CB 740 (b), CNF-CB 840 (c) and CB (d) electrodes by analysing the I-V curve at various current densities up to 1.5 mA cm<sup>-2</sup>.

The internal resistance for the CNF-CB 740 and CB was estimated to be about 446 and 666  $\Omega$  cm<sup>-2</sup>, respectively. It was also calculated that the internal resistance of CNF-CB 640 and CNF-CB 840 was about 514 and 600  $\Omega$  cm<sup>-2</sup>, respectively. This result means that the low interfacial resistance of CNF-CB 740 provided the improvement of the activity of ORR and cycle stability in hybrid Li-air batteries.

### 3.3.3 The effect of remained Ni<sub>3</sub>Fe metallic particles for characterization and electrochemical performance of CNF-CB series

The XRD diffraction and TG-DTA result showed that the Ni<sub>3</sub>Fe metallic particles were remained after acidic wash by HCl solution. Even though the quantity of Ni<sub>3</sub>Fe was very small (~ 3wt%), however we should determine electro catalytic activity of Ni<sub>3</sub>Fe particles to analysis role of CNF-CB in Li-air battery under hybrid electrolyte. Furthermore, some metallic catalyst such as precious metal or rare metal with their composite showed high electro catalytic activation to use only small amount, because it had excellent electro catalytic activity for ORR or OER. Therefore, the CNF-CB 740 after acidic wash with CNF-CB 740 before acidic wash were examined battery test to confirm electro catalytic activity of Ni<sub>3</sub>Fe composite for Li-air battery under hybrid electrolyte. The CNF-CB 740 before acidic wash was prepared by same fabrication procedure, however the acidic wash step was skipped after grown CNF.

Figure 3-16 showed XRD pattern for CNF-CB 740 before acidic wash with corresponded intensity of Ni<sub>3</sub>Fe at range 20 to 80 ° (2 theta). The X-ray diffraction intensities of Ni<sub>3</sub>Fe were obtained at 25, 35.7, 44.2, 51.5, 58.1, 64.3 and 75.8 ° (2 theta). The largest peak intensity was at 44.2 ° (2 theta) among those peaks. Furthermore, all diffraction peaks of Ni<sub>3</sub>Fe was corresponded with XRD pattern of CNF-CB 740 before acidic wash. This result indicated that the Ni<sub>3</sub>Fe metallic particles was located in CNF-CB 740. The particle diameter of Ni<sub>3</sub>Fe was calculated by Scherrer equation.

$$\tau = \frac{k\delta}{\beta \cos\theta}$$

where, k was the shape factor, which use 0.9 generally,  $\delta$  the constant (0.1542),  $\beta$  was the half of maximum XRD peak intensity, and  $\theta$  two theta angle for maximum intensity. The  $\beta$  value calculated by “(the peak intensity of maximum – intensity of back ground)/2”. Furthermore, the two theta angle used at 43.8 °. As a result, the calculated diameter value of Ni<sub>3</sub>Fe was near 4.1 nm.

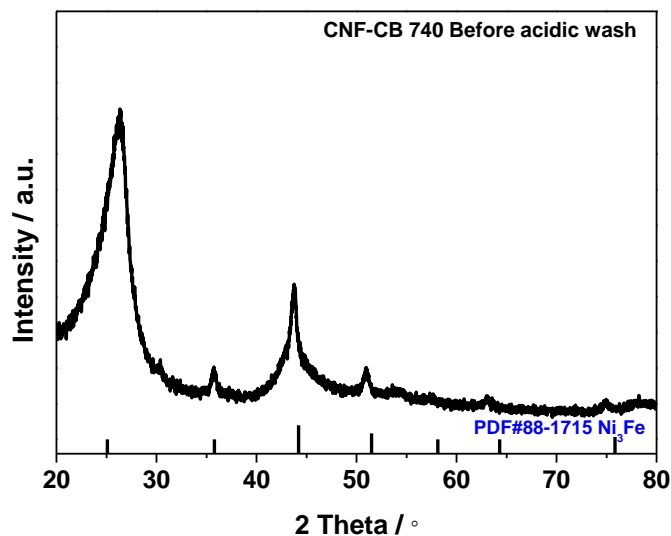


Figure 3-16. The XRD pattern for CNF-CB 740 before acidic wash with corresponded intensity of Ni<sub>3</sub>Fe at range 20 to 80 ° of 2 theta.

Figure 3-17 showed TG-DTA curve for CNF-CB 740 before acidic wash. The temperature area for TG-DTA measurement was from room temperature to 900 °C in air condition and 100 ml s<sup>-1</sup> of speed. Moreover, the temperature raising rate was 10 °C min<sup>-1</sup>. From the TG curve, the CNF-CB 740 before acidic wash sample also showed nothing mass loss for initial area (~300 °C), which indicated that CNF-CB samples have not any functional group on the surface too. In addition, the 8.8 wt% of Ni<sub>3</sub>Fe was remained after carbon combustion, which quantity was higher 5 time. Thus, 80% of Ni<sub>3</sub>Fe particles for CNF-CB 740 was removed during acidic wash by HCl solution. Furthermore, DTA curve showed the temperature for carbon decomposition for CNF-CB 740 before acidic wash sample. The top point of DTA curve was began at 533 ° to 629 °, which indicated that the CNF-CB 740 was started to decompose at 533 ° and finished at 629 °. That was lower temperature than that of acidic washed CNF-CB 740. It might be considered that the Ni<sub>3</sub>Fe metallic particle had an effect to decompose

carbon material easier.

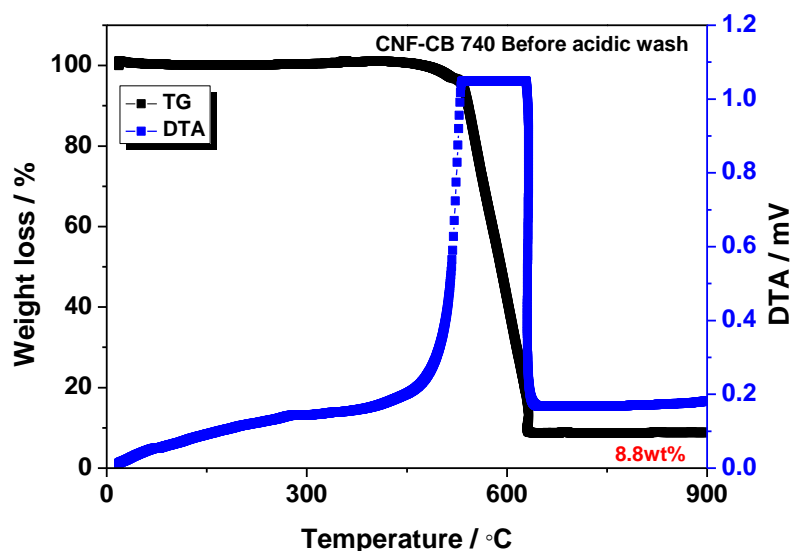


Figure 3-17. The thermo gravimetric (TG) and differential thermal analysis (DTA) curve from room temperature to 900 °C of temperature range under air condition (100 ml min<sup>-1</sup>) and the 10 °C min<sup>-1</sup> of temperature raising speed for CNF-CB 740 before acidic wash.

Figure 3-18 showed the 1<sup>st</sup> cycle discharge-charge performance for CNF-CB 740 before acidic wash by HCL solution (a) with CNF-CB 740 (b) after acidic wash samples to confirm electro catalytic effect of Ni<sub>3</sub>Fe metallic particle for Li-air battery under hybrid electrolyte. The comparison was occurred only at 1<sup>st</sup> cycle, because of the almost material showed most strong catalytic activation at 1<sup>st</sup> cycle. The battery performance measurement had same condition with previous analysis, but measuring time was only 2 h. Both material showed stable discharge-charge performance, however that showed difference performance. The CNF-CB 740 after acidic wash showed 2.88 V vs. Li<sup>+</sup>/Li for discharge potential. Furthermore, it also showed 3.78 V vs. Li<sup>+</sup>/Li for charge potential. The overpotential gap of CNF-CB 740 after acidic wash was 0.9 V at 1<sup>st</sup> cycle. In contrast, The CNF-CB 740 before acidic wash samples showed 2.82 and 3.83 V vs. Li<sup>+</sup>/Li for discharge potential and charge potential, respectively. Moreover its overpotential gap was little larger than that of washed sample, which was 1.01 V at 1<sup>st</sup> cycle. The 1<sup>st</sup> cycle performance result indicated that the Ni<sub>3</sub>Fe had not catalytic activity

to improve electrochemical performance in Li-air battery under hybrid electrolyte. Or, it interrupted electrochemical reaction for discharge-charge, because non-acidic washed sample showed potential fading and higher overpotential gap than that of washed sample.

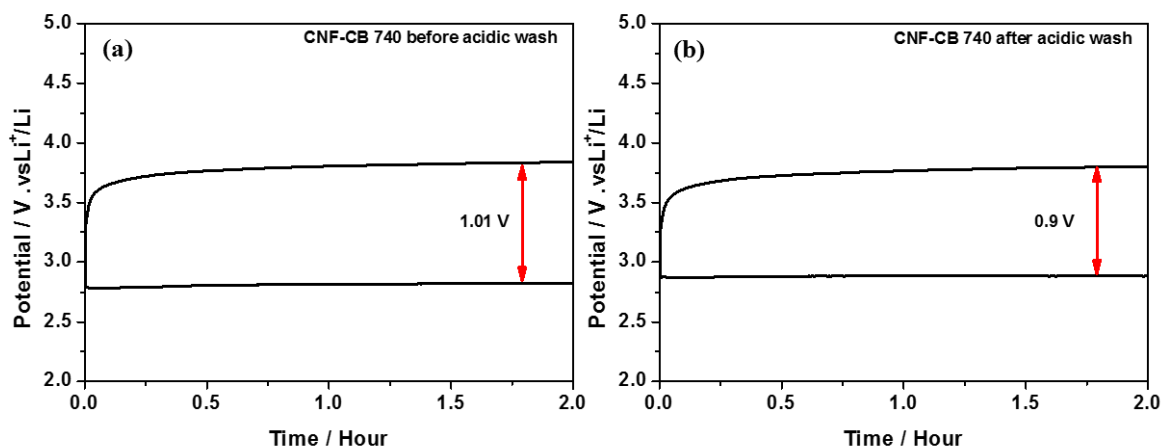
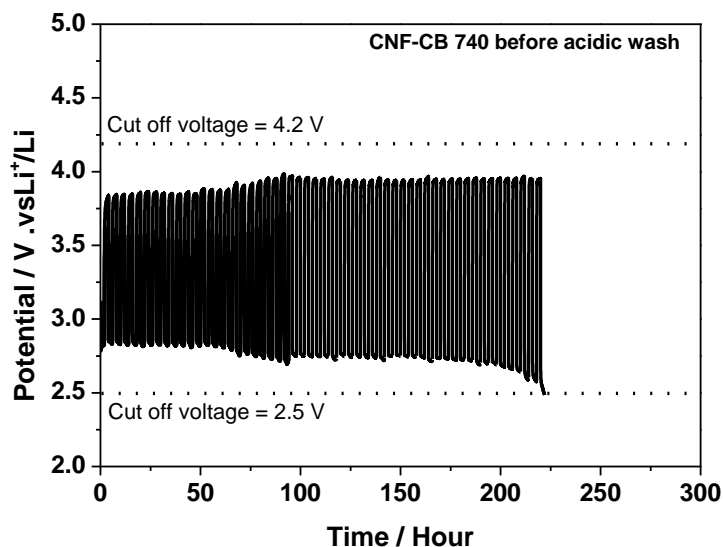


Figure 3-18. The discharge-charge performance for 1<sup>st</sup> cycle at a current density of 0.5 mA cm<sup>-2</sup> each 2 h under hybrid electrolyte for CNF-CB 740 before acidic wash (a) and after acidic wash (b), respectively.

Moreover, the non-acidic wash CNF-CB 740 was obtained worse performance than that of CNF-CB 740 for discharge-charge performance as shown in Figure 3-19. The discharge-charge performance was also measured at 0.5 mA cm<sup>-2</sup> with discharge and charge each 2h in cut off voltage from 2.5 V to 4.2 V. The discharge potential was reached cut-off voltage at 222 working hour, thus discharge-charge performance was operated during 220 hour. Thus, the hybrid electrolyte Li-air battery cell based on non-acidic wash CNF-CB 740 was obtained 55 cycle performance. Although the overpotential gap at 1<sup>st</sup> cycle for non-acidic wash CNF-CB 740 showed higher than that of acidic wash CNF-CB 740, the charge potential was obtained similar potential with acidic wash CNF-CB 740 during cycling performance. In contrast, the overpotential of discharging was kept higher than that of acidic wash CNF-CB 740. This result indicated that the performance fading might be occurred more during discharging than the

charging.

Figure 3-19. The discharge-charge performance at a current density of  $0.5 \text{ mA cm}^{-2}$  each 2 h under hybrid electrolyte for CNF-CB 740 before acidic wash.



Therefore, the non-acidic wash CNF-CB 740 was measured for BET analysis. As a result, the non-acidic wash CNF-CB 740 was obtained lower specific surface area than that of acidic was CNF-CB 740, as shown table 3-5. The specific surface area of non-acidic was  $194 \text{ m}^2 / \text{g}$ , which was smaller than  $324 \text{ m}^2 / \text{g}$  of acidic was CNF-CB 740. Thus, non-acidic was CNF-CB 740 had 40% reduced surface area of CNF-CB 740 after acidic wash.

	BET surface area ( $\text{m}^2 / \text{g}$ )
CNF-CB 740 before acidic wash	194
CNF-CB 740 after acidic wash	324

Table 3-5. The comparison of BET surface area for CNF-CB 740 before acidic wash with after acidic wash.

This result indicated that the non-activation  $\text{Ni}_3\text{Fe}$  metallic particles used many surface. Therefore, the smaller surface area of CNF-CB 740 before acidic wash could

accommodated tiny area for discharge product such as lithium hydroxide (LiOH). Therefore, the discharge performance fading was occurred more easily than that of acidic wash CNF-CB 740.

### 3.4 Conclusion

This research aimed to improve cycle performance without using metallic catalyst, because of metallic catalyst had a negative side effect for carbon corrosion. Therefore, the carbon composite of CNF-CB was prepared CVD method at difference temperature condition, which was tested for cathode as Li-air battery under hybrid electrolyte. CNF-CB materials shown that the difference electro catalytic activation, which might be attributed with grown temperature condition for CNF. Furthermore, Ni<sub>3</sub>Fe metallic composite was detected on XRD diffraction of CNF-CB after acidic wash by HCl solution. Therefore, the comparative experiment was examined to confirm electrochemical effect of remained Ni<sub>3</sub>Fe. As a result, remained Ni<sub>3</sub>Fe was not shown any electrochemical activation. Moreover, the non-acidic wash CNF-CB sample showed poor cycle performance than that of CNF-CB after acidic wash sample. Because of the Ni<sub>3</sub>Fe was decreased surface area. The detail of mechanism of ORR for the CNF-CB 740 was not clear yet. However, we have found that the CNF-CB 740 exhibited good high activity of ORR in alkaline media. This good performance of CNF-CB 740 as a catalyst to reduce oxygen may be attributed to the presence of active site as shown by specific surface area. Moreover, the CNF-CB 740 enabled long term cycling performance of hybrid Li-air batteries near 300 h. This enhanced cycle stability could be attributed to the good graphitization of CNF, which is suggested by Raman result. It was the first time using CNF-CB as a cathode of hybrid Li-air batteries, and these results will encourage further investigation using optimized CNF-CB as a promising candidate to replace conventional carbon materials in hybrid Li-air batteries.

### 3.5 Reference

[1] E. Yoo, H. Zhou, ACS Nano, 5 (2011) 3020-3026.

- [2] C H. Ahn, T. Okada, M. Ishida, E. Yoo, H. Zhou, *Journal of Power Sources*, 307 (2016) 474-480.
- [3] S. Wang, S. Dong, J. Wang, L. Zhang, P. Han, C. Zhang, X. Wang, K. Zhang, Z. Lan, G. Cui, *J. Mater. Chem.*, 22 (2012) 21051-21056.
- [4] L. Wang, X. Zhao, Y. Lu, M. Xu, D. Zhang, R S. Ruoff, K J. Stevenson, J B. Goodenough, *Journal of The Electrochemical Society*, 158 (2011) A1379-A1382.
- [5] C. Sun, F. Li, C. Ma, Y. Wang, Y. Ren, W. Yang, Z. Ma, J. Li, Y. Chen, Y. Kim, L. Chen, *J. Mater. Chem.*, A 2 (2014) 7188-7196.
- [6] L. Li, A. Manthiram, *Nano Energy*, 9 (2014) 94-100.
- [7] J S. Lee, G S. Park, H I. Lee, S T. Kim, R. Cao, M. Liu, J P. Cho, *Nano Lett.*, 11 (2011) 5362-5366.
- [8] J. Wu, H W. Park, A. Yu, D. Higgins, Z. Chen, *J. Phys. Chem.*, C 116 (2012) 9427-9432.
- [9] E. M. Benbow, S. P. Kelly, L. Zhao, J. W. Reutenauer, S. L. Suib, *J. Phys. Chem.*, C 115 (2011) 22009-22017.
- [10] L. Li, S. Liu, A. Manthiram, *Nano Energy*, 12 (2015) 852-860.
- [11] J. Huang, B. Zhang, Y. Y. Xie, W. W. K. Lye, Z.-L. Xu, S. Abouali, M. Akbari Garakani, J.-Q. Huang, T.-Y. Zhang, B. Huang and J.-K. Kim, *Carbon*, 100 (2016), 329-336.
- [12] M. S. Bhuvaneshwari, N. N. Bramnk, D. Ensling, H. Ehrenberg, W. Jaegermann, *Journal of Power Sources*, 180 (2008) 553-560.
- [13] S.M. Jang, J. Miyawaki, M. Tsuji, I. Mochida, S.H. Yoon, K. Fei-yu, *New carbon materials*, 25 (2010) 89-96.
- [14] M S. Dresselhaus, A. Jorio, M. Hofmann, G. Dresselhaus, R. Saito, *Nano Lett.*, 10 (2010) 751-758.
- [15] T. Jawhari, A. Roid, J. Casado, *Carbon*, 33 (1995) 1561-1565.
- [16] Y. Wang, S. Serrano, J J. Santiago-Aviles, *Synthetic Metals*, 138 (2003) 423-427.
- [17] L.Li, S. Liu and A. Manthiram, *Nano Energy*, 12 (2015), 852-860..
- [18] L. Li, A. Manthiram, *Adv. Energy Mater*, 4 (2014) 1301795.

## Chapter 4. Conclusion

The main goal of this research was to investigate the electrochemical performance improvement for Li-air battery under hybrid electrolyte by using two kind of cathode materials. Furthermore, we made an attempt to find unessayed material and applying as cathode for Li-air battery. Those material were based on nano structure carbon materials such as reduced graphene and carbon nanofiber. Furthermore, we also tried to analysis electro catalytic activity for these materials through various equipment.

Moreover, we endeavored to suggest guidance for investigation of new catalyst materials for hybrid Li-air battery to show advantage and challenges for both material. The electro catalytic activity and result of battery test for RGO-Co(mqph) and CNF-CB were to draw the conclusion as following.

In chapter 2, we studied Co(mqph) as cathode catalyst to improve electro catalytic activity for ORR in hybrid Li-air battery. The result of XRD, SEM, TEM, TG-DTA, XDX and XPS measurement showed that Co(mqph) was not decomposed during heat treatment, furthermore that was dispersed on the RGO surface very uniformly. The electrochemical performance for ORR of RGO-Co(mqph) was analyzed by CV and LSV measurement. From the CV and LSV result, RGO-Co(mqph) had on set potential at -0.06 V vs. Ag/AgCl for ORR. On the other hands, pristine RGO showed on set potential at -0.13 V vs. Ag/AgCl. This result indicated that Co(mqph) improve electro catalytic activity for ORR. Furthermore, the electron transferred number of RGO-Co(mqph) was to be 3.52, however RGO had electron transferred number of only 2.22. Thus, RGO-Co(mqph) had 4 electron path way for ORR in aqueous electrolyte. It indicated that Co(mqph) enhanced electro catalytic activity for ORR.

Nevertheless, the RGO-Co(mqph) showed larger overpotential gap than that of pristine RGO during cycle performance. It was considered that the carbon oxidation might occur by metallic catalyst during cycle performance.

Even though RGO-Co(mqph) showed improvement of catalytic activity for ORR in aqueous electrolyte, it also showed critical problem of carbon oxidation during cycle performance. The CNF-CB was used metal-free cathode catalyst to prevent carbon oxidation by metallic catalyst in chapter 3. The CNF-CB had different properties such

as graphitization, surface area and shape of grown CNF depend on grown temperature (640, 740 and 840 °C) during CVD method. It was obtained by TG-DTA, Raman and BET that CNF-CB 740 had not only highest graphitization but also largest surface area than that of CNF-CB 640 and CNF-CB 840. The pristine CB showed lowest graphitization and surface area than that of CNF-CB.

The CNF-CB 740 showed most long cycle performance (near 300 h) than that of CNF-CB 640, CNF-CB 840 and CB. In addition, the CNF-CB 740 had internal resistance about  $466\ 666\ \Omega\ \text{cm}^{-2}$ . It was also calculated that the internal resistance of CNF-CB 640, CNF-CB 840 and CB was about 514, 600 and  $666\ \Omega\ \text{cm}^{-2}$ , respectively. This result means that the low interfacial resistance of CNF-CB 740 provided the improvement of the activity of ORR and cycle stability in hybrid Li-air batteries.

We demonstrated the electrochemical performance hybrid electrolyte Li-air battery for based on RGO-Co(mqph) and CNF-CB as cathode. Both material showed good electro catalytic activity for ORR as well as moreover good cycle performance in hybrid electrolyte Li-air battery. At same time, both material also showed drawbacks. The data shown in this thesis can be help other future research to design catalyst material as cathode.

# List of Research Results

## **Published Paper list**

1. 『Electrochemical characteristic of based on carbon mixed with organic metal complex (Co(mqph)) in alkaline media Li-air battery.』  
Chang-ho Ahn, Tatsuhiro Okada, Masayoshi Ishida, Eunjoo Yoo, Haoshen Zhou Journal of Power Sources 307 (2016) 474-480.
2. 『Enhanced cycle stability of hybrid Li-air batteries with carbon nanofiber grown on carbon black.』  
Chang-ho Ahn, Je-Deok Kim, Masayoshi Ishida, Eunjoo Yoo, Haoshen Zhou RSC adv., 6 (2016) 74195-74200.

## **Presentation**

1. 『Research of electrochemical characteristic of carbon based organic metal complex (Co(mqph)) catalyst in alkaline media Li-air battery.』  
Chang-ho Ahn, Masayoshi Ishida, Eunjoo Yoo, Haoshen Zhou  
Kyoto, The 55<sup>th</sup> battery symposium in Japan 2014.11.19 (Oral)

# Acknowledgement

I don't know, "how can I say thank you" for everyone.

Until finish my works, I got a lot of help regardless of the place and the situation. I want to say "thank you for your great help." to those kindly people who give help me so much.

First of all, I would like to say Thank you to my esteemed Professor Masayoshi Ishida in University of Tsukuba and Professor Haoshen Zhou in University of Tsukuba and AIST. They gave greatful opportunity to study in Japan to achieve my dream. Although my first season of my Japan-life has some problems, I could overcome by Prof. Ishida's favor. I hope to send again my thankful. Prof. Zhou also guided me to right way for research as well as broken the frame of my wrong thinking though discussions. Furthermore, his kind and encourage words always help to be keeping my mind strongly. If I could not take sensitive care for both Professors, I could not finish my works. Thank you so much, sir.

I also would like to say Thank you to associated Professor Hanada in university of Tsukuba. I always finding her, when some problems about academic were occurred in my Japan-life. At that time, she advised many things by kind and smile every time. Thank you so much.

I hope to say thank you to Dr. Eunjoo Yoo of AIST too. She always coached many thing for experiment and reading research data. Her coaching became a foundation for development of my research ability. Thank you so much.

Thank you so much, Dr. Jedeok Kim of NIMS. He help to both side for my improvement. Therefore, I could finish my dissertation. I never forgot your regard, moreover I also pray for continue our good relationship in the future.

And my friends, Thank you.

Especially, Dr. Guo of AIST, my friend and father of cute boy. I could use almost analysis equipment for my experiment because of you. Furthermore, you always help

me in Lab and university, when I ask. I believe that you become a great father for your boy. I will also pray for him.

Mrs. Thu of university, Mr. Wu, Mr. Bai, Ms. Li, Ms, Liu and Mr. Zhou kai of AIST. Thank you so much to make beautiful memory. I remember you.

I also would like to say thank you to Dr. Kitaura and Mr. Okagaki. When I has some problems on AIST, they teach me very kindly. Without their regard, I have big problems anytime. Thank you so much.

The Korean oversea students, Mr. Youngjae Park, Mrs. Hyunjoo Joo and Seohyun Lee. Thank you very much. They always tried to solve my problems as well as they always stay near for me, when I alone. They always supported comfortable like real family, which help to concentrate my work by myself. Thank you.

My family,

Thank you very much, they are power, encourage, wisdom and love for me. I love you my family forever.

나의 엄마, 장인순 여사. 항상 믿어줘서 고마워. 나는 엄마의 자존심이니 항상 당당할 수 있도록 노력하며 살게. 항상 고맙고 사랑해. 나의 아빠, 안주영 거사님. 아빠의 기도 덕에 무사히 마치고 돌아갈 수 있게 되었습니다. 가끔은, 우리 사이에 오해가 생기기도 하지만 앞으로는 더 많은 대화를 통해 더 행복해졌으면 좋겠어요.

나의 또 하나의 아버지 천성욱 선생, 또 하나의 어머니 박정금 여사 감사합니다. 이 감사한 마음을 어떻게 말로 다 표현 할 수 있을까요?? 두 분께서 보내주신 응원과 격려로 항상 든든했고 힘을 낼 수 있었습니다. 항상 감사하고 건강하세요.

내 동생, 안미현. 고맙다. 건강해라.

나의 반쪽, 나의 부인 천경. 내가 학위를 마치는데 가장 큰 역할을 해줘서 고마워. 너의 믿음과 지지 그리고 사랑덕분에 난 항상 강해질 수 있었고 어려움들을 극복할 수 있었어. 행복하자. 사랑한다. 항상.